Rational Design, Synthesis and Optimization of Manganese-Based Cathode Materials for Lithium-ion Batteries

UNIVERSITY OF THE
WITWATERSRAND,
JOHANNESBURG

Aderemi Bashiru Haruna

A Thesis submitted for the faculty of Science at the University of Witwatersrand
Johannesburg, in the fulfilment for the degree of

Doctor of Philosophy in Chemistry

Supervisor: Prof. Kenneth I. Ozoemena

August, 2020

DECLARATION

I declare that this thesis is my own, unaided work. It is being submitted for the degree of Doctor of Philosophy in the University of the Witwatersrand, Johannesburg. It has not been submitted before for any degree or examination in any other university.

SIGNATURE: .... Date: ...21 October 2020..........

DEDICATION

This thesis research work is dedicated to my wife and children

ACKNOWLEDGEMENTS

I give thanks and glory to Almighty God who has always been my stronghold.

I am very grateful to my supervisors: Professor Kenneth Ozoemena and Dr. Dean Barrett for their super supports.

I thank the Materials for Energy Research group (MERG) and Faculty of Science for funding.

I acknowledge the supports of Dr. Barrister J. I. Oni and his family, Dr. Cristianae Rodella (LNLS, Brazil), Dr Andrew Venter and Ms. Zeldah Sentsho (NECSA), Dr Tumaini Mkwizu, Tshepo Mashoene, Dr. Shina Okueso, Engr. Mike Akande, Engr. Ganiyu Moody, Mr. Ayodele Durojaiye, Mr. Olawale Ikuseru, Mr. Bamidele Osinlu, Mr. Toba Durojaiye, Pastor Shola Akinpelu, Mr. Abubakar Abussalam (Chinese Academy of Sciences) and Ms. Babalwa Bali.

Thanks to my group members, the CATMAT group and all who in one way or the other made this program a success.

My profound gratitude to parents, family members and friends.

PUBLICATIONS

1. A. B. Haruna and K. Ozoemena. *Effects of microwave irradiation on the electrochemical performance of manganese-based cathode materials for lithium-ion batteries. Curr Opin Electrochem 2019, 18:16–23*
2. D. H. Barrett and A. Haruna. *Artificial intelligence and machine learning for targeted energy storage solutions. Curr Opin Electrochem 2020, 21:160–166*
3. A. B. Haruna and K. Ozoemena. *Manganese-based bifunctional electrocatalysts for zinc-air batteries. Curr Opin Electrochem 2020, 21:219–224*
4. A. B. Haruna and K. Ozoemena. *Effects of microwave irradiation on physical and electrochemical properties of Spinel* $LiMn_2O_4$ *Cathode Material* (to submit - 2020).
5. A. B. Haruna and K. Ozoemena. *Defect-engineering of* β-$MnO_{2-\delta}$ *precursor controls the structure-property relationships in high voltage spinel* $LiMn_{1.5}Ni_{0.5}O_{4-\delta}$ *cathode materials for lithium-ion battery* (to submit - 2020).

CONFERENCES

1. A. B. Haruna and K. Ozoemena. *Enhanced Performance of Spinel* $LiMn_{1.5}Ni_{0.5}O_4$ *Controlled by Oxygen Vacancy*. Belgrade Online Meeting of the International Society of Electrochemistry 2020. Submitted poster: s08-53
2. A. B. Haruna and K. Ozoemena. *Nanorod-like* $LiMn_{1.5}Ni_{0.5}O_4$ *for high-performance lithium-ion batteries*. 70th Annual meeting of the ISE 2019
3. A. B. Haruna and K. Ozoemena. *Spinel* $LiMn_{1.5}Ni_{0.5}O_4$ *Cathode Material for Lithium-ion Batteries: Effect of the degree of order of Mn/Ni and* Mn^{3+} *Content on the Electrochemical Performance*. Pre satellite ISE meeting - “Energy Storage and Industry 4.0: Challenges and Prospects”. South Africa, 2019
4. A. B. Haruna and K. Ozoemena. *Nanorod-like* $LiMn_{1.5}Ni_{0.5}O_4$ *for high-performance lithium-ion batteries*. University of Witswatersrand Cross faculty symposium 2018
5. A. B. Haruna and K. Ozoemena *Nanorod-like* $LiMn_{1.5}Ni_{0.5}O_4$ *for high-performance lithium-ion batteries.* 4th International Symposium on Electrochemistry 2018

PROFESSIONAL ORGANIZATIONS

1. International Society of Electrochemistry
2. South African Chemical Institute
3. Institute of Chartered Chemist of Nigeria
4. Institute of Public Analyst of Nigeria
5. Nigeria Institute of Food Science and Technology

AWARD/SCHOLARSHIP

1. **Postgraduate Merit Award** awarded by University of The Witwatersrand, 2020 & 2019
2. **Ph.D. Scholarship** awarded by Faculty of Science, 2019
3. **Ph.D. Scholarship** awarded by Materials for Energy Research Group, 2017 – 2018.
4. **Poster Presentation (**1st position**)**: 2018 4th International Symposium on Electrochemistry, University of Johannesburg, South Africa

ABSTRACT

This Ph.D. thesis strategically investigated some synthetic methods aimed at tuning the physico-chemistry and electrochemical properties of two manganese-based spinel cathode materials (i.e., $LiMn_2O_4$ (LMO) and $LiMn_{1.5}Ni_{0.5}O_4$ (LMNO)) for Li-ion batteries. For the LMO, pristine commercial LMO material (LMO-p) was subjected to microwave irradiation process to obtain a modified LMO material (LMO-m). The effects of microwave irradiation on these two materials were thoroughly studied using different advanced techniques, including synchrotron powder x-ray diffraction (SPXRD), x-ray photoelectron spectroscopy (SXPS), powder neutron diffraction (PND), Solid-State Magic-Angle-Spinning Lithium Nuclear Magnetic Resonance (MAS ^{7}Li NMR), Raman spectroscopy, thermogravimetric analysis (TGA) and Nitrogen Gas Adsorption analysis. TGA results reveal that the LMO-m sample is more thermally stable than the LMO-p sample. The Nitrogen Gas Adsorption analysis results show that the LMO-m has a larger surface-area, pore-volume and pore-size than LMO-p. Nitrogen Gas Adsorption analysis, SXRD, SXPS, ^{7}Li MAS NMR and PND consistently prove that microwave irradiation has increased the Mn^{4+} content in LMO-m more than in the LMO-p. Electrochemistry techniques (i.e., cyclic voltammetry (CV), electrochemical impedance spectroscopy (EIS) and galvanostatic charge-discharge (GC-D)) show that LMO-m possesses faster electron transfer kinetics, mass transport, better reversibility (Coulombic efficiency), higher specific capacity, and higher conductivity than the LMO-p. For the first time, this study has shown that microwave irradiation can suppress Jahn-Teller distortion and improve the physical and electrochemical properties of LMO without the conventional doping or surface-coating.

For the LMNO, for the first time, two simple strategic alternative synthetic routes were used to synthesize LMNO cathode materials from β-$MnO_{2-\delta}$ with different contents of oxygen vacancy. One was obtained in argon atmosphere (LMNO-Ar) and the other in high reducing hydrogen atmosphere (LMNO-H_2). The TGA, SPXRD, Raman spectroscopy and GC-D reveal that LMNO-Ar has better structural stability than LMNO-H_2, while SPXRD, FTIR, Raman, XANES, CV and GC-D show that the two samples have both disorder and order phases. The SPRXD, PND, SXPS, CV and GC-D revealed that LMNO-H_2 has greater Mn^{3+} content than the LMNO-Ar and thus directly reflects oxygen vacancy contents in the two cathode materials. The CV, GC-D and EIS show that the LMNO-H_2 is more conductive than LMNO-Ar. The GC-D reveals that LMNO-H_2 has a better specific capacity (113.6 $mAhg^{-1}$) than that of LMNO-Ar (90.1 $mAhg^{-1}$) but has worse capacity retention of (48.3%) than that LMNO-Ar (77.6%). The TEM images show that the two samples are nanorods. The results reveal that the oxygen vacancies change concurrently with the degree of disorder and amount of Mn^{3+}. The discharge capacity increases with oxygen vacancies, degree of disorder and amount of Mn^{3+}, while the retention capacity decreases with increasing with oxygen vacancies, disorder and amount of Mn^{3+}. These studies reveal strategic processes that can be adapted in the design, synthesis and optimization of the spinel Mn-based cathode materials for Li-ion batteries.

TABLE OF CONTENTS

LIST OF FIGURES

LIST OF TABLES

LIST OF SYMBOLS

A - Alpha

β - Beta

γ - Gamma

δ - Delta

λ - Lamda

° - Degree

‹ - Less than

≤ - Less than or equal to

› - Greater than

~ - Approximately

Θ - Theta

Al - Aluminum

Ar - Argon

Cr - Chromium

Cu - Copper

F - Fluorine

Mn - Manganese

Mg - Magnesium

Ni - Nickel

O - Oxygen

LIST OF ABBREVIATIONS

ACS:	American Chemical Society
ACE:	Associte Chemical Enterprises
AR:	Analytical reagent
BET:	Brunauer-Emmett-Teller
BNEF:	Bloomberg New Energy Finance
C V:	Cyclic voltammetry
3D:	Three dimension
DEC:	Diethyl carbonate
DMC:	Dimethyl carbonate
EC:	Ethylene carbonate
eV:	Electronvolt
EV:	Electric Vehicle
FCC:	Face Centered Cubic
FTIR:	Fourier-transform infrared spectroscopy
G C-D:	Galvanostatic charge-discharge
GHz:	Gigahertz.
HEVs:	Hybrid Electric Vehicles

IR:	In-frared
JCPDS:	Joint-Committee on Powder Diffraction Standards
J-T:	Jahn-Teller
Li:	Lithium
LCF:	Linear Combination Fitting
LIB	Lithium-ion battery
LMO:	$LiMn_2O_4$
LMNO:	$LiMn_{1.5}Ni_{0.5}O_4$
m:	Microwave
MAS:	Magic-angle spinning
Ni-Cd:	Nickel-Cadmium
Ni-MH:	Nickel-Metal Hydride
Ni-Cu:	Nickel-Copper
NMC:	Lithium nickel-manganese-cobalt oxides
NMP:	N-methyl-2-pyyolidone
NMR:	Nuclear magnetic resonance
UV:	Ultraviolet
US:	United States

p:	Pristine
ppm:	Part per million
PHEV:	Plug-in Hybrid Electric Vehicle
PND:	Powder neutron diffraction
PVDF:	Polyvinylidene fluoride
RS:	Raman-Spectroscopy
SPXRD	Synchrotron Powder *X ray* Diffraction
SXPS	Synchrotron X ray photoelectron spectroscopy
TEM:	Transmission-Electron Microscopy
V:	Volt
VIS:	Visible
Vs:	Versus
XANES:	X ray absorption near edge structure

CHAPTER 1

Introduction

1.1 Introduction

This section covers the motivation, rationale, aim and objectives of the research work. And finally, the thesis layout.

1.2 Motivation

There is currently an interesting developmental transition in the power and transportation systems. Bloomberg New Energy Finance (BNEF) predicted that solar and wind will constitute about 40% of the world electricity in 2040 from 7% (2019) [1] as shown in Figure 1.1.

Therefore, the need to store will be on the upsurge to balance the rise in the amount of intermittent sustainable power production. Thus, the applicable choice to modern power production is the electrical energy-storage-system and battery shall be the appropriate option to its successful application. The energy storage outlook emphasized the need for low-cost lithium-ion battery by 2030 to meet up the demand in the two key markets: (i) electric-vehicles and (ii) stationary storage [3].

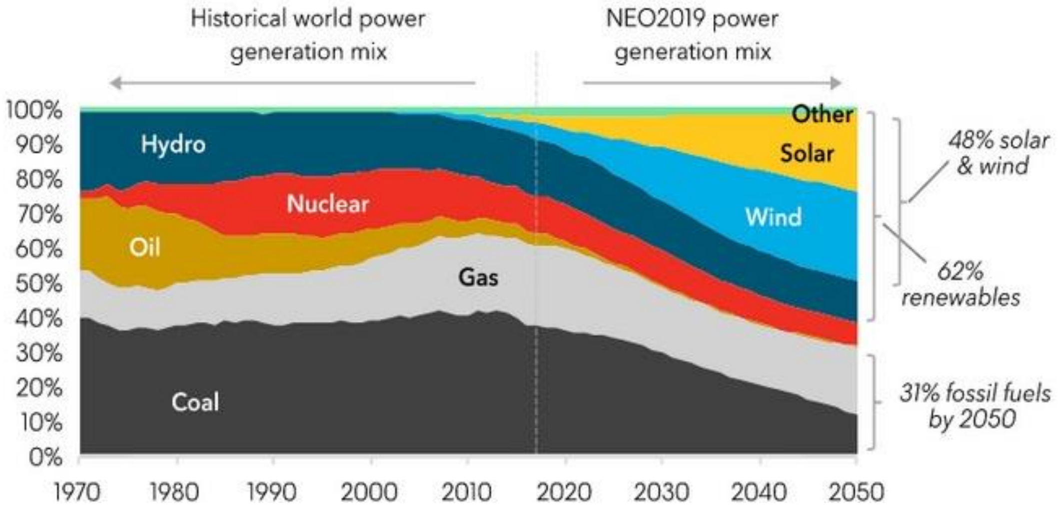

Figure 1.1: Global power generation mix [2]

The Li-ion battery's purchase price is of considerable importance for its practical application in electrical energy storage. Positive electrode materials constitute about one-fourth of the overall price of a Li-ion battery pack. Hence Mn-based materials have continued to be attractive and explored for Li-ion positive electrode materials because of their low costs, natural abundance, relatively less toxic and high operating voltages [4]

Figure 1.2 shows the US Geological Survey of global manganese reserves: South Africa has 80% of the global manganese reserves. Thus, this work on manganese-based cathode materials is to boost the value chain opportunity of the abundant manganese reserve in South Africa.

The manganese-based cathode materials comprise of the two spinels (LMO and LMNO); and the layered materials [Li-Ni-Mn-Co oxides (NMC)] [4]. However, this research work is limited to spinel materials only.

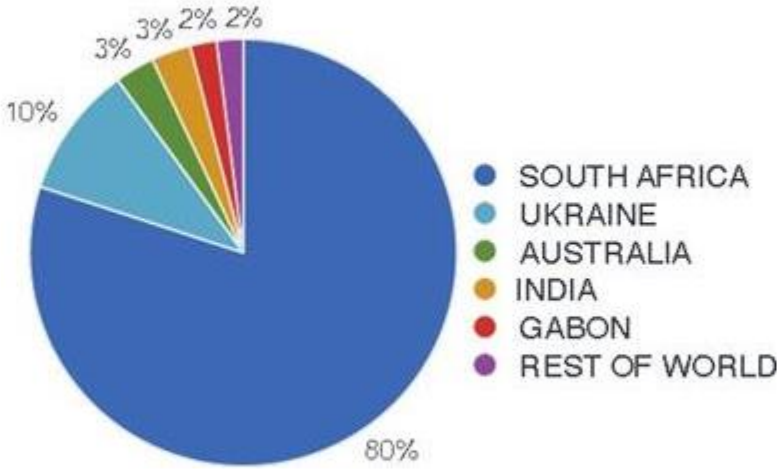

Figure 1.2: Global manganese reserves [5]

LMO has been of practical application, however it still has the challenge of low cycle performance particularly at high temperatures due to the Jahn-Teller distortion and degradation of Mn^{3+} (equation 1.1). LMNO is favored potential positive electrode next generation Li-ion battery for its increased 4.7 V, however its commercialization is still a challenge because of its low cyclic-stability and lower rate-capability [6].

$$2Mn^{3+}_{(solid)} \longrightarrow Mn^{4+}_{(solid)} + Mn^{2+}_{(solution)} \qquad (1.1)$$

Therefore, this thesis studied (LMO and LMNO) for lithium-ion batteries. This research work focused on the materials chemistry in terms of the fundamental properties (such as the Mn^{3+} contents, Mn oxidation-state, cation disordering/ordering) for the design, synthesis and optimization of spinel manganese-based cathode for Li-ion battery.

This study explored the usage of microwave irradiation as an alternative strategy to enhance the physico-chemical properties and electrochemical redox reactions in LMO cathode material without a decrease in the specific capacity. It is shown in this study how microwave irradiation has improved the fundamental properties of the LMO without doping or surface coat as in previous studies (7). This strategy is unique for the improvement of the physical and electrochemical properties of LMO because of its simplicity ("take complex and make it simple is genius" - Albert Einstein). It is proven by various analytical methods (Nitrogen Gas Adsorption analysis TGA, SXPS, 7Li MAS NMR, PND, CV, GC-D and EIS) that microwave irradiation can improve the physical and electrochemical properties of LMO for Li-ion battery.

Furthermore, the research work examined the use of different levels of atmospheres to synthesis the precursor: β-$MnO_{2-\delta}$ for the tuning of oxygen vacancy in LMNO for Li-ion battery. The fundamental properties (oxygen vacancies, degree of disorder, Mn^{3+} content and impurities) have significant effect on the performance of LNMO spinel for Li-ion battery [7,8]. This work showed that the structural parameters (oxygen vacancies, degree of disorder, Mn^{3+} content and impurities) can be tuned to enhance electrochemical performance of the LMNO for Li-ion battery.

1.3 Objectives

1. To synthesize LMO-microwave (LMO-m) from commercial LMO (LMO-p) using microwave irradiation
2. To investigate the effect of microwave irradiation in LMO-m relative to LMO-p by analytical techniques: SPXRD, PND, NMR, RAMAN, SXPS and XANES.
3. To investigate the electrochemical properties of the LMO-p and LMO-m in fabricated lithium-ion battery coin cells
4. To synthesize the precursors: β-$MnO_{2-\delta}$ under different levels of reducing atmospheres.
5. To synthesize of different polymorphs of spinel LMNO cathode materials having different oxygen vacancies, degree of disorder, Mn^{3+} contents and impurities.
6. To characterize the prepared spinel LMO (pristine and microwave) and LMNO polymorphs by analytical techniques: SPXRD, FTIR, Raman, PND, NMR, SXPS and XANES
7. To Investigate the electrochemical performance of prepared spinel LMO (pristine and microwave) and LMNO polymorphs using coin type Li-ion cells.

1.4 Outline

Chapter 1 (Introduction): This chapter presents the motivation, objective and outline of the thesis.

Chapter 2 (Literature-review): This section presents the review on works carried out on LMO and LMNO cathode materials for Li-ion battery

Chapter 3 (Experimental): This section narrates the synthesis procedures with the analytical techniques.

Chapter 4 (Results and discussions): This chapter presents and discusses the results obtained in the use of microwave irradiation to retard the Jahn-Teller distortion, improve the physical properties and enhance the specific capacity of spinel LMO for Li-ion battery.

.**Chapter 5 (Results and discussions):** This chapter reports the relationship among the oxygen vacancy, degree of disorder, Mn^{3+} content and impurity; and resultant effect on electrochemical performance of the spinel LMNO for Li-ion battery.

Chapter 6 (Conclusions): Results’ conclusions and recommendations are presented in this section.

1.5 References

(1) Bloomberg new energy out: 2019/07

(2) Bloomberg resources publication: 2019/07

(3) Bloomberg energy storage investment boom 2019/07

(4) A. B. Haruna and K. I. Ozoemena, Curr Opin Electrochem 2019, 18:16–23

(5) https://aheadoftheherd.com/Newsletter/2017/The-Missing-Link2.html (2017)

(6) J. Lu and K. S. Lee, Material Technology: Advance Performance Materials 2016, Vol. 31, No. 11, 628-641

(7) J. Lee, N. Dupre, M. Avdeev and B. Kang Scientific Reports volume 7, Article number: 6728 (2017)

(8) Yoon et al. Journal of Alloys and Compounds 686 (2016) 593-600

CHAPTER 2

Literature Review

2.1 Lithium-ion batteries

2.1.1 History

Benjamen Franklin was the first to coin the term “battery” when conducting experiment on electricity in 1749. The first dry cell battery: Zinc-carbon cell was produced by Carl Gassner in 1887. Waldmar Jungner produced the Ni-Cd battery and Ni-Fe battery in 1899. Thomos Edison patented a modified design of Jungner’s nickel-iron battery in 1903. Lewis Urry of the company now known as Energizer made a breakthrough when he came up with alkaline battery in 1955. The 1970s and 80s led to the discovery of nickel-hydrogen and nickel-metal hydride batteries (Ni-MH) respectively [1].

Though Li battery was created in 1912 [1]; Whittingham in 1970 created a pathway for using lithium in room temperature rechargeable batteries which Exxon commercialized in 1997. The dendrite growth during cycling led to its failure. In 1980 Goodenough reported a new class of cathode material: two-dimensional Layered Li_xCoO_2 and Sony commercialized it to be the first successful Li-ion battery in 1991. Thackeray and Goodenough discovered a three-dimensional compound: spinel $LiMn_2O_4$ in 1983 which unlike the layered $LiCoO_2$ is cheaper and less toxic. The spinel $LiMn_2O_4$ has intersecting three-dimensional intercalation pathways that facilitate high charge and discharge rate. The main challenge is the capacity fading due to J-T distortion and Mn^{2+} dissolution [2].

Zhou et al. [3] cited previous reports on the suppression of J-T distortion and Mn^{2+} dissolution in spinel $LiMn_2O_4$. Consequently, the nickel substituted spinel $LiMn_{1.5}Ni_{0.5}O_4$ was first proposed by Amine et al. and Dahn et al.

2.1.2 Background

The growth in the world's population coupled with the industrial and technological advancement of the society has led to an increase in the global energy demand [4]. For over two centuries the comforts of life have relied on reserves of natural fuels (oil, coal and natural gas) [5] which are limited and not sustainable [6] Furthermore, the resultant environmental issues of burning these carbonaceous fuels and the emission of CO_2 on our planet cannot be overemphasized. Consequently, it is evidence that technical solutions are now required to prevent colossal energy crisis [5].

Renewable and sustainable energy sources (solar and wind) have gained more attention to reduce greenhouse emissions. These sustainable sources are intermittent, thus required efficient electrical energy storage systems (EESS) for grid stability and widespread distribution in order to compete with the current most used fossil fuels [4,7]. The (EESS) such as batteries are key enabling technologies that will aid the realization of electro-mobility, smart-grids and realistic reduction of CO_2 emission [8].

Batteries are devices to store chemical energy and release the energy in an electrical form in the context of a specific application [9, 10]. The two main forms of batteries are rechargeable and non-rechargeable [11].

The policy support coupled with the research progress on electric vehicle (EV) will play a considerable role in the reduction of energy and environmental challenges. EESS has been identified as key player to the feasibility of EVs. The Li-ion battery (L-IB) have gained greater attention than convention EESS because of higher densities (energy and power) [4-8, 12].

Currently, L-IB is used in mobile applications. However, the current L-IB cannot compete with the performance of fossil fuel vehicles [7]. The need to increase the drive-distances and rate capability; lower cost and improve safety for L-IBs in the EVs are required. Therefore, it is crucial for further research works on the improvement of L-IBs that are safe and environmentally friendly at a reduced cost [13].

L-IB have lesser weight and produce higher voltage (about 4 V) as compared to conventional batteries (Ni-Cd and NiM-H) as shown in Table 2.1. Thus, L-IB have higher gravimetric and volumetric densities (Figure 2.1) which gave L-IB preference for use in lighter and compact equipment.

Table 2.1: Li-ion batteries vs convectional batteries [14].

Chemistry	**Volt**	**Wh/Kg**	**W/Kg**
Lead-acid	2	30	180
Nickel-Cadmium (Ni-Cd)	1.2	47	120
NiM-H	1.2	55	200
Li-ion	**3.6**	**90**	**430**

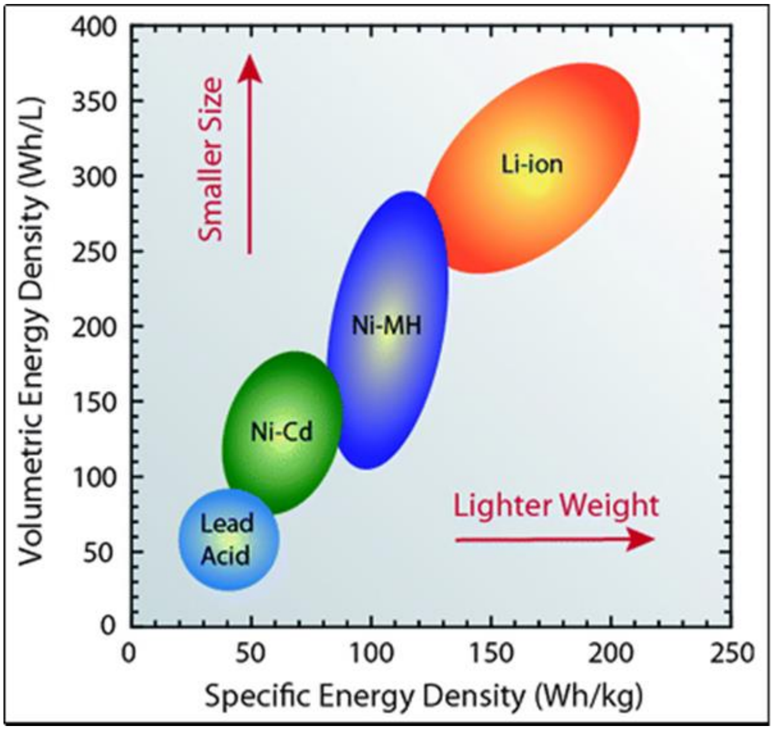

Figure 2.1: Volumetric energy density versus specific energy density plot for Li-ion and conventional batteries [16]

2.1.3 Lithium-ion battery: current chemistry

The L-IB works by the intercalation mechanism (insertion or extraction of Li^+ into the crystal lattice of host electrode without altering its crystal structure). These intercalation hosts have suitable lattice sites or open crystal structures that allow reversible oxidation and reduction reactions [15].

L-IB mainly comprises of Electrodes, Electrolyte, Separator (polymer membrane) and current collector [Copper (Cu) and Aluminum (Al)] [15] as shown in Figure 2.2. The batteries undergo oxidation and reduction reactions during the charging and discharging processes respectively. Li in the cathode ionized and moves through the electrolyte into the lattice structure of the anode, while the electron moves out of the cathode to anode through external load in the charge process. Consequently, electrical energy is stored in the form of chemical energy in the battery (equation 2.1 and 2.2) [17,18].

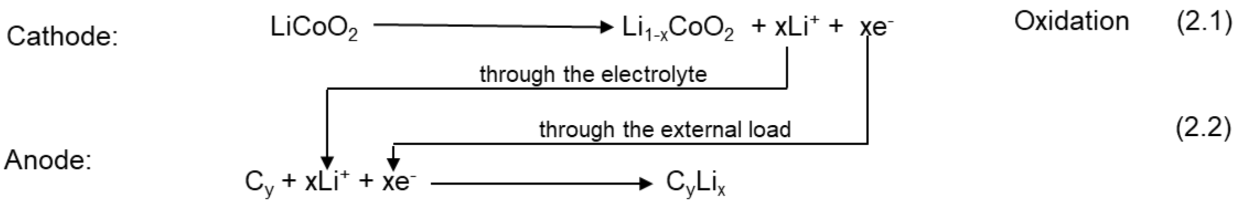

Cathode: $LiCoO_2 \longrightarrow Li_{1-x}CoO_2 + xLi^+ + xe^-$ Oxidation (2.1)

Anode: $C_y + xLi^+ + xe^- \longrightarrow C_yLi_x$ (2.2)

The discharging process is the reverse of the charge (equation 2.3 and 2.4) [17,18].

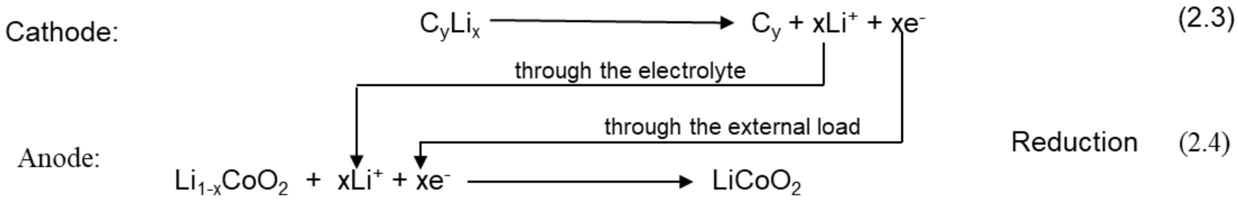

Cathode: $C_yLi_x \longrightarrow C_y + xLi^+ + xe^-$ (2.3)

Anode: $Li_{1-x}CoO_2 + xLi^+ + xe^- \longrightarrow LiCoO_2$ Reduction (2.4)

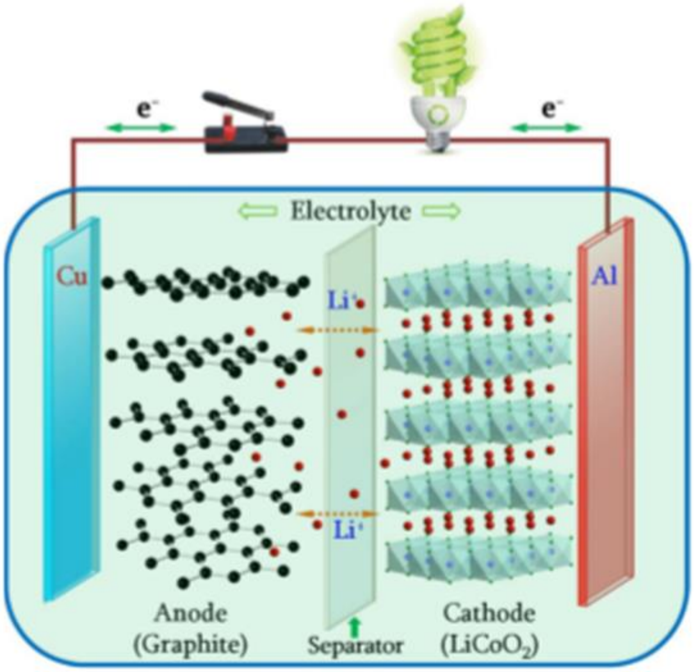

Figure 2.2: Schematic Configuration of rechargeable Li-ion batteries [72]

The overall process is a reversible reaction charging-discharging process (equation 2.5). This forth and back movement of the lithium ions during charge and discharge processes led to lithium-ion batteries being called the Rocking Chair (swing) cells.

$$\text{Overall Process} \quad LiCoO_2 + C_y \rightleftarrows Li_{1-x}CoO_2 + C_yLi_x \qquad (2.5)$$

2.1.4 Next-generation lithium-ion batteries

The commercialized cathode material: $LiCoO_2$ could not meet the goals of the next generation EVs, Hybrid Electric Vehicles (HEVs) and PHEVs in terms of safety, cost, performance and environmental issues. Therefore, there is need for safer, cheaper and less toxic cathode materials that have high densities (energy and power) for use in these next-generation vehicles [19, 20].

The manganese-based spinel cathode materials amongst all others are future choices for higher densities (energy and power) battery applications because of the higher voltages (Table 2.2) [9]. In 1983, Thackeray reported spinel lithium manganese oxide ($LiMn_2O_4$) and was commercialized by NEC in 1996. The spinels (LMO and LMNO) are of great interest due to the ease of preparation, abundance, low cost and environmental friendliness. Among the derivatives, LMNO is the most favored as a result of its approximately 4.7 V [19].

Table 2.2: LMO batteries Vs convectional LIBs [9]

Cathode	Structure	Potential Vs Li/Li$^+$ (V)	Specific capacity mAhg^{-1}	Specific energy (WhKg^{-1})
$LiCoO_2$	Layer	3.70	140	546
$LiFePO_4$	Olivine	3.45	150 - 170	518 - 587
$LiMn_2O_4$	**Spinel**	**4.10**	**100 - 120**	**410 - 492**

2.1.4.1 Spinel lithium manganese oxides: $LiMn_2O_4$ (LMO) cathode material

Spinel lithium manganese oxides ($Li_xMn_2O_4$) are of great interest as intercalation cathode materials that meet the cost, toxicity, and efficiency criteria for commercial lithium-ion batteries [21, 22]. The classical LMO has *Fd3m* symmetry, where the Li and Mn are found in the 8a and 16d Wyckoff positions in a cubic close-packed array of oxygen. The 16c octahedral sites are vacant [21]. The 8*a* and 16*c* Wyckoff positions form the 3D channel for Li diffusion (Figure 2.3) [23, 24]. The 8a site bonds each of their four faces with neighboring 16c vacant site (Figure 2.4) [27]. At around 4 V, the Li$^+$ moves (through 8a--16c-to another 8a) in 3-dimensions during de-lithiation process [23].

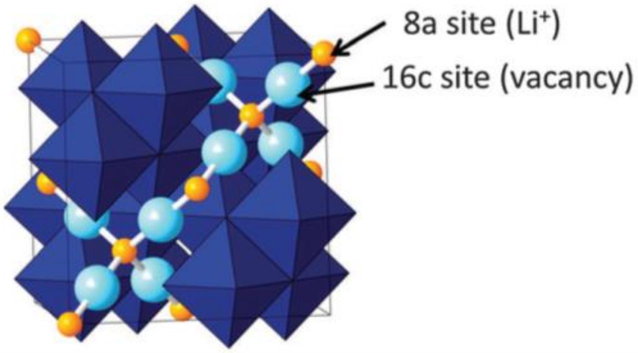

Figure 2.3: 3D Li$^+$ diffusional route [24].

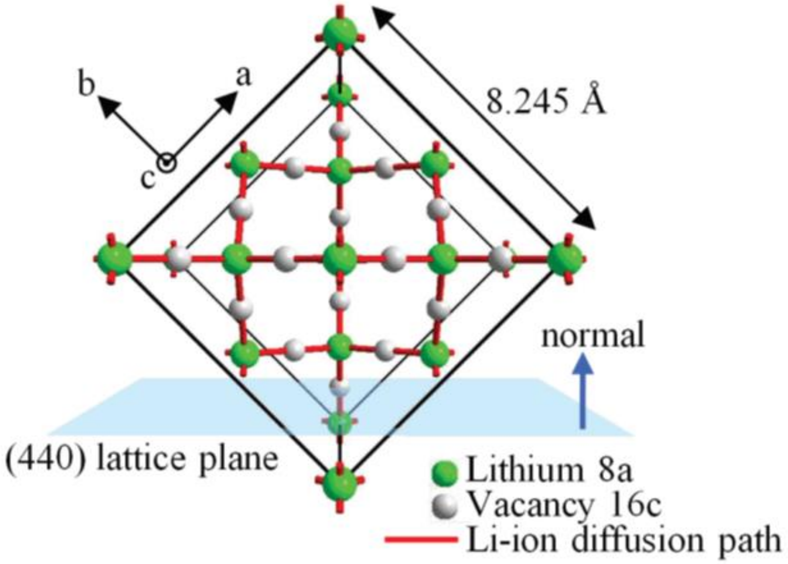

Figure 2.4: Cross section of LMO spinel phase: Li^+ sites (8a) with vacancies (16c) and Li^+ diffusion paths [25].

Figure 2.5 shows the spinel structure of cubic system *Fd3m* space group of the model LMO at room temperature.

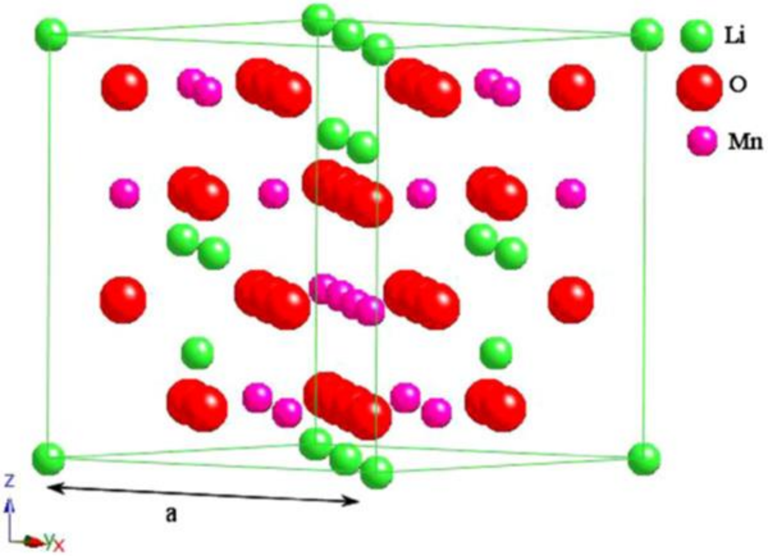

Figure 2.5: The spinel $LiMn_2O_4$ crystal structure [26]

The Mn in the octahedral sites exist as high spin Mn^{3+} (50%) and Mn^{4+} (50%) with $3d^4$ ($t_{2g}^3e_g^1$) and $3d^3$(t_{2g}^3) electronic configurations respectively. The structural formula of the cubic spinel $LiMn_2O_4$ can be expressed as $[Li]_{8a}[Mn^{3+},Mn^{4+}]_{16d}O_4$ [27].

2.1.4.1.1 Challenges

Several papers have reported that the setback of LMO for L-IBs is a decay capacity during charge-discharge process [22]. Researchers have attributed the source of the capacity fading to (i) the presence Jahn-Teller (J−T) active Mn^{3+} and (ii) the charge disproportionation of Mn^{3+} [27-30], explained below:

2.1.4.1.1.1 Jahn-Teller (J−T) active Mn^{3+}

The J-T effect, otherwise known as J-T distortion, is termed after Hermann Arthur Jahn and Edward Teller. Teller et al. [31] used group theory to prove that non-linear degenerate molecules are not stable. Therefore, elimination of degeneracy occurs by distortion to reduce the complex’s energy. The J-T effect mostly occur in transition metals octahedral complexes such as $Mn^{3+}O_6$ octahedral in the spinel LMO structure shown in Figure 2.6 [33].

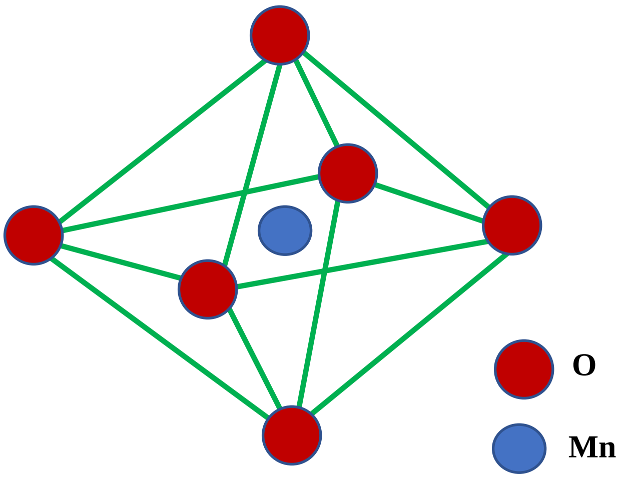

Figure 2.6: $Mn^{3+}O_6$ octahedron in the spinel LMO structure

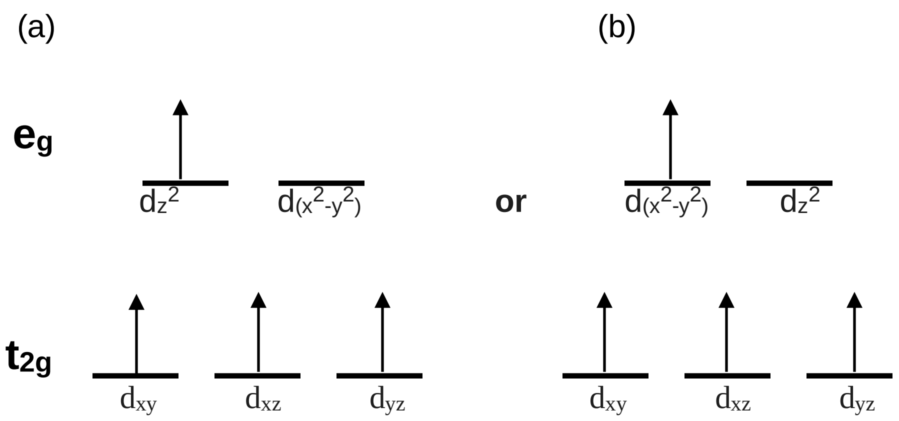

Figure 2.7: Schematic illustration of the electronic configuration of high spin Mn^{3+}

In LMO, the octahedral high spin Mn^{3+} has the electronic configuration t_{2g}^3 and e_g^1 while that of octahedral Mn^{4+} is t_{2g}^3. Therefore, one electron will occupy one e_g orbital while the other is vacant as shown in Figure 2.7 (a and b). In accordance with J-T theorem, the Mn^{3+} gets distorted to reduce energy and symmetry, thus the degeneracy is eliminated.

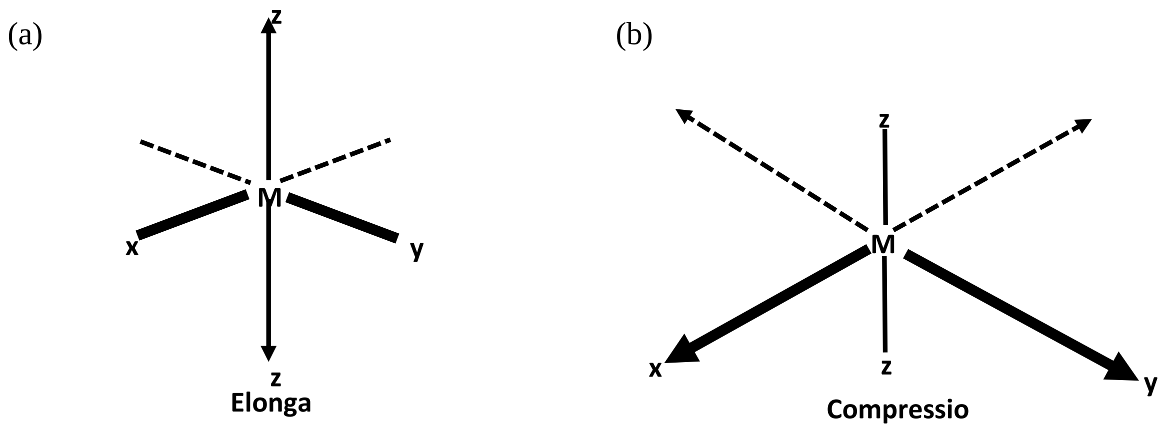

Figure 2.8: J-T distortion – (a) elongation, (b) compression

If the e_g electron position is in $d_z^{2.}$ orbital, then there will be a concentration of the electron density within the Mn and two O along the z-axis. Hence the electrostatic repulsion associated with these oxygens will be greater than the other 4 and the MnO_6 octahedral complex elongates along the z axis (as illustrated inFigure 2.8a).

The elongation stabilizes (i.e. lowers the energy) each of the d orbital along the z-axis, while those on the xy and x^2-y^2 axes are weakened (i.e rises in energy) [32]. Thus, the reduced energies of d_z^2, d_{xz} and d_{yz} orbitals breaks the degeneracy as shown in **Figure 2.9a**. This is known as tetragonal distortion (elongation). Similarly, if the e_g electron is in $d_{x^2\text{-}y^2}$ orbital, the MnO_6 octahedral complex elongates in the x and y axes. Consequently, this termed tetragonal distortion (compression). (Figure 2.8b, 2.9b).

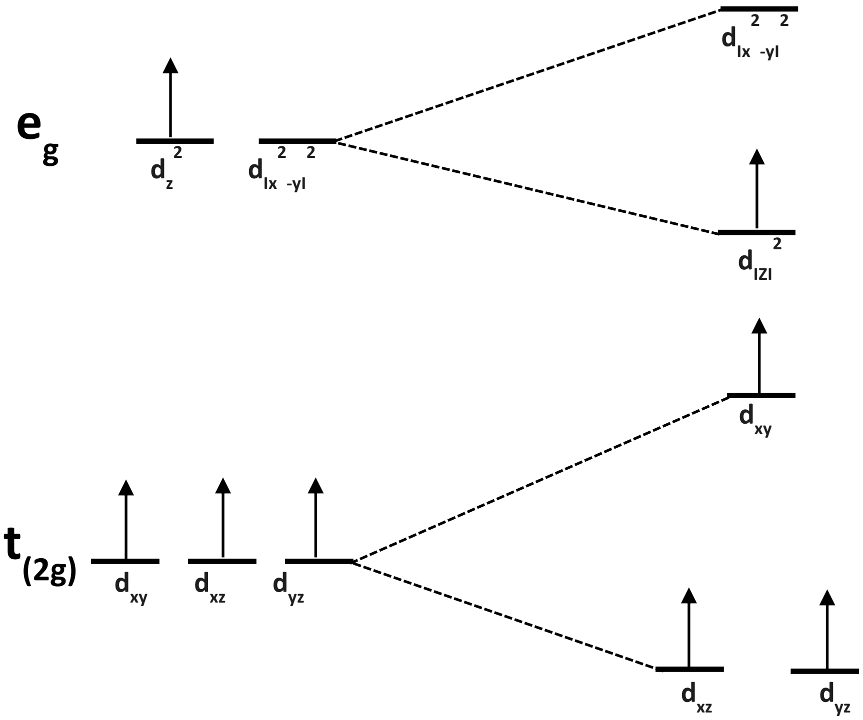

Figure 2.9a: Elongation distortion for an $Mn^{3+}O_6$ complex

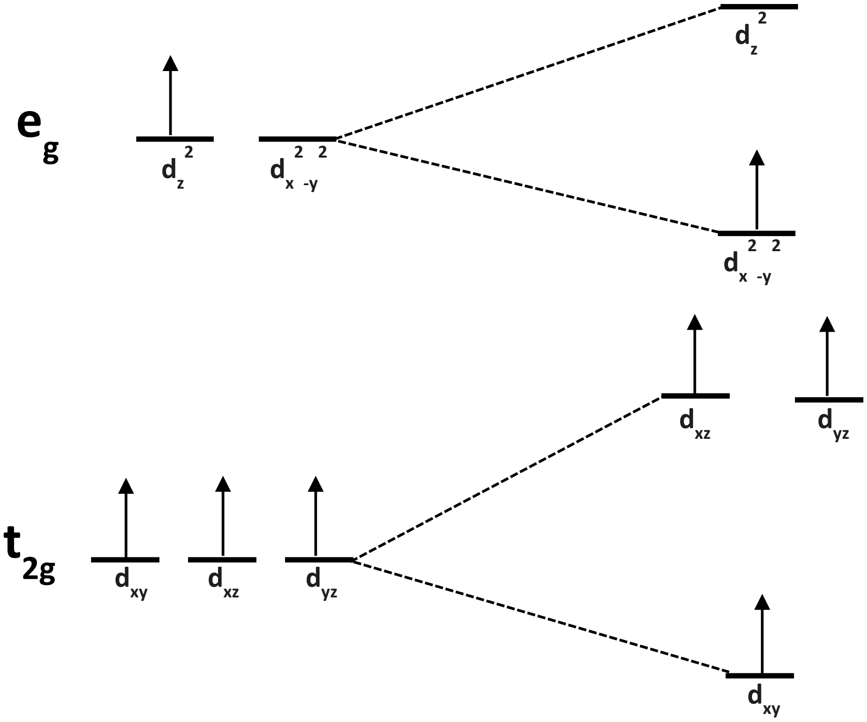

Figure 2.9b: Compression distortion for an $Mn^{3+}O_6$ complex

Researchers have shown that the capacity fading of 4 V LMO batteries can be attributed to the presence of the J−T active Mn^{3+} during charge-discharge processes [26, 34].

The J-T transition of the cubic crystal structure of spinel LMO to tetragonal structures can occur by (i) chemical or electrochemical redox reactions, (ii) heating $Li_{1.05}Mn_2O_4$ to high temperature and fast cool to room temperature and (iii) cooling stoichiometric $LiMn_2O_4$ sample cooled to 280 K [35]. This research work focused on only item (i).

2.1.4.1.1.1.1 Chemical or electrochemical redox reactions

Thackeray group [36] reported that spinel LMO cells were discharged at 3 V [$Li_xMn_2O_4$ (Li/Li^+)] when $1<x\leq2$ and 4 V when $O\leq x\leq1$. The insertion of Li into $Li_xMn_2O_4$ at 3 V (equation 2.8) caused the average Mn-ion valency to be below 3.5, which thus introduce a J-T distortion into the spinel structure. Consequently, the J-T distortion caused the transition from cubic to tetragonal with a 16%-unit cell increase (c/a ratio), which destabilized the $Li_xMn_2O_4$ structural integrity during cycling. Thus, led to significant decay in its capacity. The decay in capacity limits the application of LMO electrodes as a 3 V cell [37, 38]. The 4 V electrode has better cycling stability than that of 3 V, but it shows capacity fading [26].

It is common knowledge that Li^+ can be removed and injected into the spinel LMO. The removal of a Li^+ from the 8a of the cubic LMO ($Li_{(8a)}[Mn_2]_{(16d)}O_4$) takes place occurs in 2 steps at around 4 V vs (equation 2.6 and 2.7) [38]

$$LiMn_2O_4 \longrightarrow Li_2Mn_2O_4\ (LiMnO_2) \quad (2.6)$$

$$LiMn_2O_4 \longrightarrow Mn_2O_4\ (\lambda\text{-}MnO_2) \quad (2.7)$$

The insertion of Li^+ into the spinel $[Li^+]_{tet}[Mn^{3+}, Mn^{4+}]_{oct}O_4$ increases during the Li interaction process and led to the formation of $Li_{1+x}[Mn^{3+}]_{1+x}[Mn^{4+}]_{1-x}O_4$. Hence electron must be added to maintain charge balance (equation 2.10 [27].

$$Mn^{4+} + e^- \longrightarrow Mn^{3+} \quad (2.10)$$

Therefore, the ratio of $Mn^{3+} : Mn^{4+}$ is › 1 and the average Mn valency is ‹ 3.5. Consequently, the high spin Mn^{3+} leads to the J-T distortion and change in the volume of the spinel $[Li^+]_{tet}[Mn^{3+},Mn^{4+}]_{oct}O_4$. This is accompanied by capacity loss during charge-discharge processes.

2.1.4.1.1.2 The charge disproportionation of Mn^{3+}

It is also a general knowledge that during the charge-discharge processes of 4 V LMO batteries, the Mn^{3+} in spinel LMO caused Mn^{2+} dissolution. During the cycling process the dissolved Mn^{2+} gets deposited on the anode and restricts the diffusion of the Li^+. Thus, the dissolution process led to the capacity fading of the battery.

2.1.4.1.2 Solutions

The cycle performance of LMO the battery depends on the structural integrity of LMO cathode material during charge-discharge cycles. During the discharge process, the Mn^{3+} rich LMO spinel surface is generated which leads to J-T distortion [39] and a disproportionation reaction of the Mn^{3+} [40] that lowers the charge-discharge capacities and stability of the cathode. Therefore, it is of great value to carry out this research work to improve the properties of the spinel LMO for mobile and industrial applications.

Surface-coat and cation-dope processes have been reported to inhibit fading capacity of LMO, but these strategies are accompanied by a decrease in capacity [23, 26]. Some of these strategies are reviewed below:

2.1.4.1.2.1 Cation doping

Amine et al. [40] used a sol-gel method to synthesize a nanoscale homogeneous surface-doped spinel LMO ($LiMn_{2-x}Ti_xO_4$) by the incorporation of Ti^{4+} into its surface. The $LiMn_{2-x}Ti_xO_4$ cathode material has a stable crystal structure and the surface protected the bulk LMO from Mn dissolution. The $LiMn_{2-x}Ti_xO_4$ surface unlike the surface coated materials did not form a physical barrier to the ion and charge channels; thus, its surface is electrochemically active.

Fe - doped LMO reduced the J-T effect by suppressing the surface low valent Mn ions [30]. Consequently, this led to enhanced cycle performance with increased electronic and ionic conductivities.

Bi-metal (Ni-Cu) doped LMO studied by Gao et al. [28] discharged an initial capacity of 113 $mAhg^{-1}$ (0.3 C) and 88% retention capacity after 100 cycles.

Comin et al. [44] stated that highly doped samples have the de-lithiation process impaired. It is reported that doping of the LMO with Co^{3+}, Cr^{3+} and Ni^{2+} can inhibit the distortion. The group further proposed that the distortion could only be inhibited if the ratio $r = [Mn^{4+}]/[Mn^{3+}] \geq 1.18$ ($r = 1.106$ when $x = 0$) with the excess Li^+ and Mn^{3+} ions located in the 16d sites. The general formula $Li[Li_yMn_{2-y}]O_4$ can have:

(1) lithium-rich compounds $[Li]_{tetra}[Li_yMn_{1-3y}^{3+}\ Mn_{1+2y}^{4+}]_{octa}O_4$ when (y › 0) and

(2) lithium-poor compounds $[Li_{1-|y|}Mn_{|y|}^{2+}]_{tetra}[Mn_{1+|y|}^{3+}Mn_{1-|y|}^{4+}]_{octa}O_4$ when (y ‹ 0)

Yang et al [42] successfully doped Mg and F into the LMO lattice. The Rietveld refinement of the product ($LiMg_{0.1}M\text{-}n_{1.9}O_{3.8}F_{0.2}$) confirmed that the 8a sites contained Li^+, 16d sites contained the Li^+, Mg^{2+}, Mn ions and 32e sites contained O^{2-} and F^- ions relative to the pristine. The doped LMO showed improved electrochemical performance than the pristine.

2.1.4.1.2.2 Surface coating

Reduced graphene oxide was wrapped on LMO via the soft chemical method by Cao group [27]. The fishnet structured layer produced was able to absorb the volume strain due to J-T distortion and minimized the Mn dissolution and thus enhanced the cycling stability. Kang et al. [43] fabricated robust hybrid 1D LMO@C/CNF cathode material for flexible LMO cell. The LMO@C/CNF has a coated layer of amorphous carbon and exposed graphitic edge planes. The synergy of the coated amorphous layer and exposed graphitic edge planes enables the cathode material to have improved electronic conductivity, Li^+ transport and electrochemical stability. The LMO@C/CNF battery delivered a specific capacity of 126 $mAhg^{-1}$ (0.2 C) and improved cycling performance.

2.1.4.1.2.3 Morphology and Size

The synthesized nano-sized octahedral LMO structure with a strong MnO_6 framework, high Mn^{4+} content and exposed (111) crystal planes was synthesized by Tang group [44]. The octahedral LMO showed high electrochemical performance (capacity, stability and capacity retention). Cui group [45] investigated the relationship between the pore size and electrochemical performance of spinel LMO microspheres and found out that the sample with bigger pore sizes showed better electrochemical performance (capacity discharge: 124.3 $mAhg^{-1}$ and 96.9% retention capacity: 100 cycling (0.5 C)). The better electrochemistry resulted from the LMO cell with the bigger pore sizes has a lower surface area and is less affected by SEI deposited layer.

2.1.4.1.2.4 Synthesis methods

Santhanagopalan et al. [46] used sol-gel method to synthesis spinel LMO having a rich Mn^{4+} surface (Mn^{4+}/Mn^{3+} ratio = 2 approx.) to inhibit capacity fading. The fabricated LMO cells have improved electrochemical results.

2.1.4.1.2.5 Microwave irradiation

Green chemistry has called the attention of synthetic chemists to employ microwave irradiation. Green chemistry proposes reagents and methods that minimize the usage/production of harmful products. The approach advises to improve to the synthetic methods’ efficiency using fewer toxic solvents, reduce the synthesis processes and waste. Consequently, researchers have adopted the microwave irradiation method as a vital route to green chemistry [47, 48]. This study used a harmless microwave absorbent (water).

2.1.4.1.2.5.1 Microwave science

Microwave irradiation has brought a revolution to the synthesis in methods' chemistry (chemical synthesis paradigm shift). Microwave synthesis affords chemists better utilization of time unlike the inefficient and time-consuming conventional method of heating [47, 48].

Microwave irradiation offers a suitable option to the conventional heating methods. Figure 2.10 shows the spectrum of electromagnetic waves.

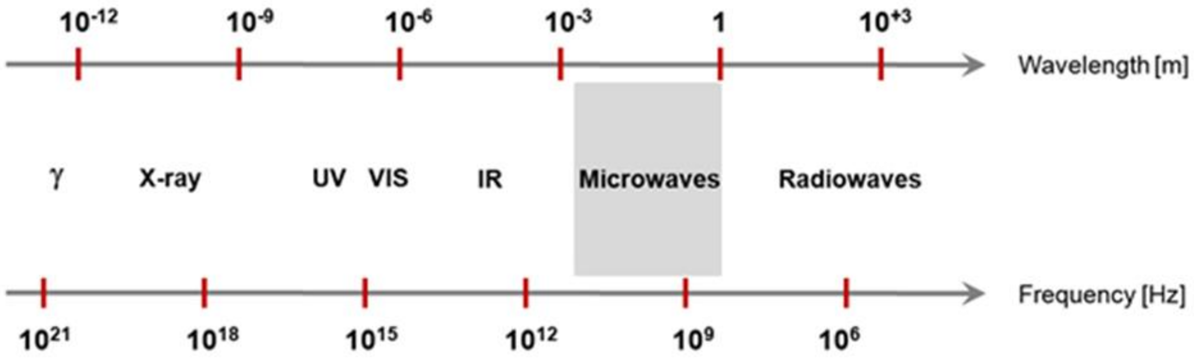

Figure 2.10: The spectrum of electromagnetic waves [49]

2.1.4.1.2.5.2 Mechanism of microwave irradiation

Generally, materials can be classified according to their response to microwave irradiation:

- Absorption materials (such as ethanol): high dielectric materials (polar organic solvents) can strongly absorb microwaves and thus fast heating of the medium.
- Transmission materials (such as sulphur): non-polar materials are microwave transparent – they allow microwave to pass through.
- Reflection materials (such as copper): they do not allow microwave to pass through, hence practically no electromagnetic wave or heat is absorbed into the system.

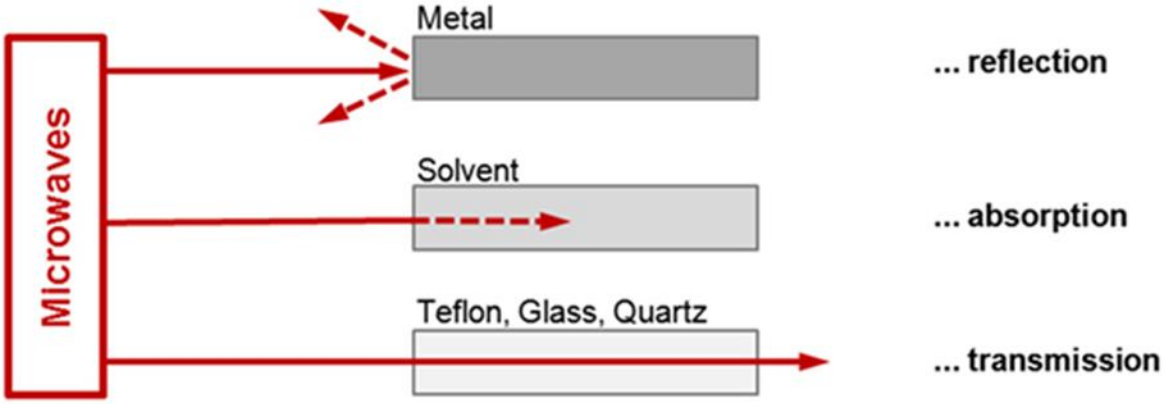

Figure 2.11: The interaction of microwave with materials [49]

There are three major techniques by which microwave absorbing materials are heated:

2.1.4.1.2.5.2.1 Dipolar polarization

A material must have a dipole-moment to generate heat by microwave irradiation [47]. Microwave irradiation usually heats materials by dipolar polarization [47, 48]. The irradiation causes the orientation of the ions along the electric field. Thus, during the ions' rotation and collision with each other, the friction that occurs produces heat. This is the mechanism by which dipolar polarization generates heat. The oscillating field's frequency range is a fundamental prerequisite for dipolar polarization (inter-particle interaction). When the range of the frequency is high, there will be inadequate dipolar polarization. This is because the polar molecule's motion will be stopped by the intermolecular forces before the molecules move with the field. Besides, when the range of the frequency is low, there will be adequate time for the polar molecule to be in phase with the field. 0.3 – 30 GHz is appropriate to oscillate the polar elements for adequate dipolar polarization [47].

2.1.4.1.2.5.2.2 Conduction

The conduction technique generates heat by the opposition to the current flow of the material. For conducting and semiconducting materials: microwave irradiation moves the charge carriers (such as electrons or ions) by an electric field which results in polarization. Heat is thus generated in the materials by the electrical resistance which resulted from the induced current [47, 48]. While for a solution, microwave irradiation moves the ions by the electric field which resulted in energy being used up. It is believed that the higher the polarity of the solvent, the higher the microwave irradiation absorbed and the higher the heat generated [47].

2.1.4.1.2.5.2.3 Interfacial polarization

In this technique the conduction and dipolar polarization techniques in play. For this technique, the conducting material (metal particles) be dispersed in a nonconducting material (sulphur). The metals will reflect most of the microwave irradiation while sulphur will transmit most of the irradiation. But when the two are combined, they form a good microwave-absorbing material provided the metal is in the powdered form. Metal powder (unlike the metal surface) is a good absorber of microwave irradiation and the heating mechanism is similar to dipolar polarization [47].

2.1.4.1.2.5.3 Microwave irradiation versus conventional synthesis

In conventional synthesis (Figure 2.12a), the heat energy is first transferred to the surface of the reaction vessels by convection or conduction and then to the sample. Thus, it takes some time to get the sample to the required temperature. Therefore, conventional synthesis is relatively energy inefficient and slow. But with the microwave irradiation, it penetrates through the reaction vessel to the sample and heat is produced via direct microwave-material interface ("in-core" heating, Figure 2.12b). The direct "in-core" microwave irradiation results in inverted temperature gradients relative to the conventional heating mechanism [47, 50]

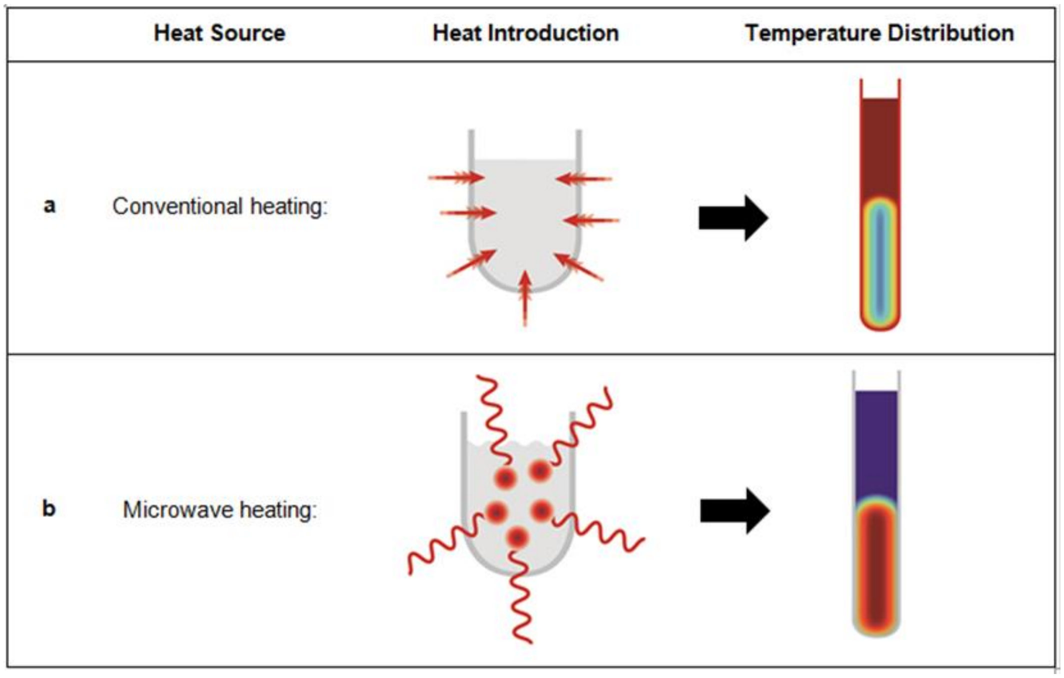

Figure 2.12: Comparison of microwave heating versus conventional heating [50]

2.1.4.1.2.5. Benefits of microwave irradiation

The advantages of microwave irradiation are outline below [47]:

(1) Faster reaction

(2) Better yield and higher purity

(3) Energy saving

(4) Uniform and selective heating:

(5) Green synthesis

(6) reproducibility

Xu et al. [51] used microwave irradiation to calcine the $LiMg_{0.05}Mn_{1.95}O_4$ produced. The synergy between Mg doping and microwave irradiation gave the product that has excellent structural stability which enhanced the discharge capacity and lowered the capacity fading.

Ozoemena group [52, 53] also reported the use of doping and microwave irradiation as a strategy to optimize the Mn valency for improved structural stability and capacity retention.

In this research work, microwave irradiation and water (as the absorbent) are used in compliance with the two key principles of green chemistry relevant to synthetic chemist. Thus, for the first time the use of microwave irradiation as a strategy to suppressed Jahn Teller distortion, increased the ratio r = $[Mn^{4+}]/[Mn^{3+}]$, average Mn oxidation state and specific capacity of the lithium-ion battery without doping and surface coating is reported..

2.1.4.2 Spinel lithium manganese nickel oxides: LMNO

Current consideration of L-IBs for large scale (EVs and stationary energy storage) applications has prompted research works for high energy and power densities materials [56, 57]. Consequently, the spinel LMNO emerged the outstanding positive electrode material, because of its higher operational 4.7 V, 3D Li-ion diffusion (high power) [58], low cost and toxicity [55]. The theoretical capacity of LMNO is 146.7 mAhg^{-1} and thus has increased energy-density (686 Whkg^{-1}) relative to $LiCoO_2$ (518 Whkg^{-1}), $LiFePO_4$ (495 Whkg^{-1}), Li_2FePO_4F (414 Whkg^{-1}), NMC 111 (576 Whkg^{-1}) [57, 58].

2.1.4.2.1 Crystal structure

LMNO ($LiMn_{1.5}Ni_{0.5}O_4$) is a spinel cubic structured crystal with the tetrahedral sites hosting the Li and the Mn and Ni are hexa-coordinated within distorted octahedra surrounded by O atoms [59]. The Mn and Ni arrangement in the LMNO depends on the synthetic temperature and atmospheric conditions among others. Therefore, the structure of spinel LMNO is in two crystal forms: Fd3m and $P4_332$ symmetries.

The Fd3m structure is non-stoichiometric ($LiMn_{1.5}Ni_{0.5}O_{4-\delta}$) with face centered cubic FCC spinel structure (Fd3m) [60]. The Mn-ions and Ni-ions are arbitrarily arranged in 16d Wyckoff position and thus, are termed as a disordered structure [61]. In the Fd3m structure, the Li^+ diffuses from the tetrahedral 8c sites through 16c sites to the next 8a tetrahedral sites as illustrated in Figure 2.13a. While the $P4_332$ symmetry exist as a stoichiometric ($LiMn_{1.5}Ni_{0.5}O_4$) having a primitive cubic structure ($P4_332$) [60]. The Mn and Ni are regularly arranged in the Wyckoff positions 4b and 12d respectively and thus are termed as an ordered structure [Figure 2.13b] [61]. In the $P4_332$ crystal structure, the Li^+ diffuses from the tetrahedral 8c sites through 16c sites to the next 8a tetrahedral sites as illustrated in Figure 2.13b.

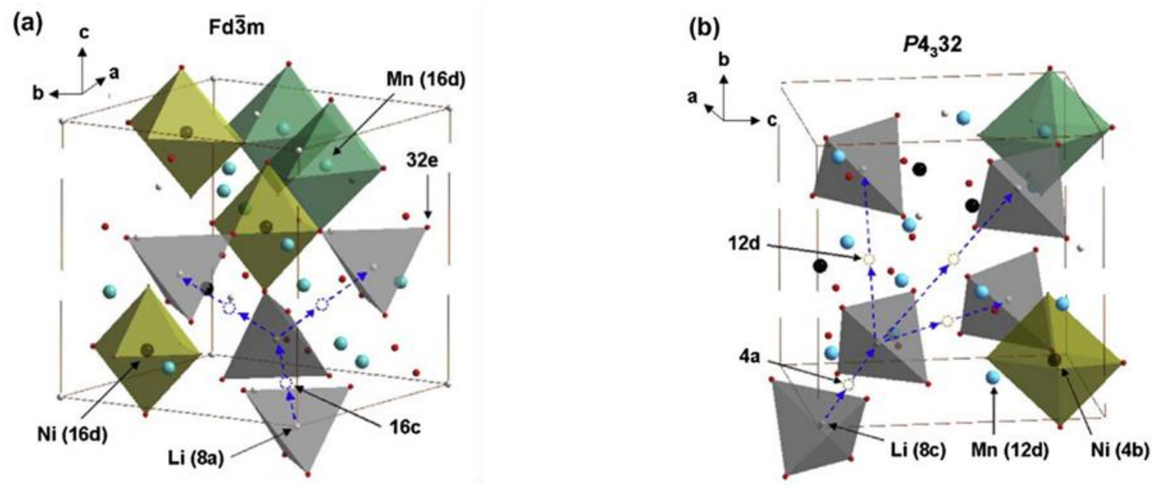

Figure 2.13: LMNO crystal structure and Li diffusion path [10]

2.1.4.2.2 Challenges

It is generally reported that the ordered symmetry is synthesized at ~ 700 °C, while the disordered symmetry is synthesized at higher temperatures, [62]. Researchers confirmed that the higher temperatures (800 to 1000 °C) employed for the preparation of the disordered phase led to oxygen loss and to maintain charge balance, some of the Mn^{4+} are reduced to Mn^{3+} [63]. In addition, there is a partial transformation of the spinel disordered LMNO to rock salt: impurities phase (NiO, Li_xNi_yO or LiNiMnO) during the higher temperature synthesis. These impurities hinder the Li^+ mobility and electron transport in the cathode material; thereby, lower its electrochemical capacity [56, 64, 65]. The ordered spinel LMNO has all the Mn ions as Mn^{4+} [56, 57] and the only redox reaction that occurs during the cycling process is between Ni^{2+} and Ni^{4+} (4.7 V versus Li^+/Li). Thus, the nonexistence of Mn^{3+} in the spinel prevents the J-T distortion and Mn dissolution during cycling which results in improved cycling performance [57]. However, the ordered spinel LMNO shows poor electronic conductivity because the active Ni^{2+} is surrounded by inactive Mn^{4+} which causes poor charge transfer between the Ni^{2+} and Mn^{4+} [56, 62].

It has been reported that the Fd3m LMNO show improved electrochemical performance relative to the ordered spinel because of the presence of Mn^{3+}. The Mn^{3+} is active electrochemically and presents a small plateau around 4 V [68, 69]. The Mn^{3+} has a larger ionic size than the Mn^{4+}. This offers improved Li^+ mobility path which promotes enhanced electronic and Li^+ conductivities. However, the Mn^{3+} is unstable and easily undergoes the disproportionation reaction to cause capacity-fade during electrochemical cycling as discussed earlier.

2.1.4.2.3 Solutions

The model disordered LMNO phase has Mn^{3+} which aids electronic and Li^+ conductivities, but high Mn^{3+} content and impurity can cause capacity fading. The ordered LMNO phase has only Mn^{4+} which provides better structural stability but deter fast transportation of Li^+. Consequently, the advantages of the two phases can be harnessed by the introduction of controlled Mn^{3+} content into the ordered phase. Thus, the co-existence of the two phases in a mix of seemingly ordered structure.

Researchers have reported that the occurrence and amount of Mn^{3+} in LMNO has an intricate effect on electrochemical performance [56, 68]. Thence, the need to control the degree of disorder, amount of Mn^{3+} and impurity cannot be overemphasized. Previous research papers' reports on the control of the amount of Mn^{3+} and impurity as highlighted below:

Ke et al. [56] were the first to report that the Mn^{3+} and impurity phase could be introduced into the spinel LMNO by inhomogeneous migration of atoms. They used the same synthesis conditions of calcining and annealing to produce three samples of spinel LMNO with different particle microstructures (hierarchical, hollow and solid) by the control of the precursors' microstructures. Their results showed that the synthesized samples have different amounts of Mn^{3+} and impurities.

Rao et al. [64] synthesized spinel LMNO that has the morphology of a caterpillar. The results of their electrochemical studies (C V and G C-D) showed that as prepared cathode material has the disordered and ordered phase with substantial Mn^{3+} content.

Magnesium was doped into spinel LMNO crystal by Wang et al. to reduce the Mn^{3+} content [69]. The doped LMNO material discharged 1209 $mAhg^{-1}$ (1 C) with capacity retention capacity: 92.2% (100 cycles).

Ozoemena's et al. [67] showed that microwave irradiation could be used to control the amount of Mn^{3+} in spinel LMNO for enhanced electrochemical performance.

LaF_3 was used to modify the surface of spinel LMNO. The nanolayer coated spinel LMNO cathode material has a reduced Mn^{3+} content relative to the pristine spinel LMNO [70].

Wang et al. [71] reported that the as prepared sample S750 has octahedron morphology with smallest particle size relative to samples S850 and S950 with the smallest Mn^{3+} content. The sample S750 delivered 110 $mAhg^{-1}$ (0.2 C) after 100 cycles

Researchers have published reports on the conventional processes to control the Mn^{3+} content in spinel LMNO, but the tuning of the Mn^{3+} content by controlling the atmosphere of the precursors' heat treatment has never been reported. Thus, this research work studied for the first time the control of Mn^{3+} and impurity in spinel LMNO by the preparation of the precursors in different levels of reduced environments. The detailed research work on the spinel LMNO is discussed in chapter 5 of this thesis. This study is proposed as an alternative strategy to design and synthesize of an improved LMNO cathode material for lithium-ion batteries.

2.1.5 Reference

1. Batteries: Electricity through chemical reactions, http://chem.libretext.org. (2020)
2. F. Ooms, E. Kelder, J. Schoonman, M. Wagemaker, F. Mulder Solid State Ionics 152–153 (2002) 143–153.
3. X. Fang, M. Ge, J. Rong and C. Zhou, J. Mater. Chem. A 2013, 1, 4083-4088.
4. D. D. Lecce, R. Verrelli and J. Hassoun, Green Chem, 2017, 19, 3442-3467.
5. M. M. Thackeray, C. Wolverton and E. D. Isaacs, Energy Environ. Sci., 2012, 5, 7854-7863.
6. C. Liu, Z. G. Neale and G. Cao, Material Today Volume 19, Number 2, March 2016.
7. X. Tang, S. S. Jan, Y. Qian, H. Xia, J. Ni, S. V. Savilon and S. M. Aldoshin, Nature 2015, Scientific Reports 5, Article Number 11958 pp 1-10.
8. D. Deng, Energy Sci. Eng. 2015; 3(5):385–418.
9. Batteries: Overview of Battery Cathodes. M. M. Doeff. Lawrence Berkerley National Laboratory, https://escholarship.org/uc/item/In55870s (02.01.2011)
10. https://documents.pub/download/safety-of-lithium-ion-batteries-recharge
11. A. Bard, G. Inzelt and F. Scholz (Eds.) Electrochemical Dictionary
12. Y. Zhu and T. Yi, Ionics (2016) 22: 1759-1774.
13. J. Ma, P. Hu, G. Cui, and L. Chen, Chem. Mater. 2016, 28, 3578−3606
14. Battery Introduction MVKF25
15. C. Liu, Z. G. Neale and G. Cao, Mater. Today, Volume 19, Number 2, March 2016.
16. https://sinovoltaics.com/wp-ontent/uploadfolders/sinovoltaics.com/2019/09/Picture1.png
17. N. Kiziltas-Yavuz, A. Bhaskar, D. Dixon, M. Yavuz, K. Nikolowski, Li Lu, R. Eichel and H. Ehrenberg, J. Power Sources 267 (2014) 533-541.

18. J. Lu and K. S. Lee, Material Technology: Advance Performance Materials 2016, Vol. 31, No. 11, 628-641
19. X. Zhang, F. Cheng, K. Zhang, Y. Liang, S.Yang, J. Liang and J Chen, RSC Advance, 2012, 2, 5669-5675 (4,6,7,8).
20. E. Zhao, L. Wei, Y. Gou, Y. Xu, W. Yan, D. Sun and Y. Jin, Journal of Alloys and Compounds 695 (2017) 3393-3401 (4,5,6-11).
21. J. Lee, F. Wang, C. P. Grey, *J. Am. Chem. Soc.* 1998, *120,* 12601-12613
22. B. Hwang, S. Kim, Y. Lee, H. Park, D. Kim, K. Park, Materials Chemistry and Physics 158 (2015) 138-143
23. K. Zhang, X. Han, Z. Hu, X. Zhang, Z. Tao, J. Chen, *Chem. Soc. Rev.,* 2015, 44, 699
24. M. Nakayama, M. Kaneko and M. Wakihara, Phys. Chem. Chem. Phys., 2012, 14, 13963–13970
25. Proell, R. Kohler, A Mangang, S. Ulrich, C. Ziebert, W. Pfleging, JLMN Vol. 7, No. 1, 2012
26. H. Xia, Z. Luo, J. Xie, Progress in Natural Science: Materials International 2012;22(6):572–584
27. Y. Chen, Y. Tian, Y. Qiu, Z. Liu, H. He, B. Li, H. Cao, Mater. Today Advances 1 (2019) 100001
28. A. Iqbal, A. Khan, T. Wang, D. Li, Y. Gao, Int. J. Electrochem. Sci., 14 (2019) 929 – 942
29. W. Wen, B. Ju, X. Wang, C. Wu, H. Shu, X. Yang, Electrochimica Acta 147 (2014) 271–278

30. H. Liu, R. Tian, Y. Jiang, X. Tan, J. Chen, L. Zhang, Y. Guo, H. Wang, L. Sun, W. Chu, Electrochimica Acta 180 (2015) 138–146
31. H. A. Jahn, E. Teller, Proc. R. Soc. Lond. A 1937 161, 220-235
32. C. Housecroft, A. G. Sharpe, Inorganic Chemistry. Prentice Hall, 3rd Ed., 2008, p. 644. ISBN: 978-0-13-175553-6
33. B. Zhang, C. Sun, P. Yang, W. Lu, B. L. Fisher, T. Venkatesan, S. M. Heald, J. Chen, G. Moog, Chow Physical Review B 89, 195140 (2014)
34. H. Hayakawa, T. Takada, H. Enoki, E. Akiba, P. Diffraction 15 (1), March 2000
35. X. Q. Yang, X. Sun, M. Balasubramanian, J. McBreen, Y. Xia, T. Sakai, M. Yoshio Electrochemical and Solid-State Letters, 4 (8) A117-A120 (2001)
36. R.J. Gummow, A. Kock, M.M. Thackeray, Solid State Ionics 69 (1994) 59-67.
37. M. M. Thackeray, A. Kock, Mat. Res. Bull. Vol 28 pp 1041-1049, 1993
38. C. Masquelier, M. Tabuchi, K. Ado, R. Kanno, Y. Kobayashi, Y. Maki, O. Nakamura, J. B. Goodenough, Journal of Solid State Chemistry 123, 255–266 (1996) Article No. 0176
39. G. Xu, Z. Liu, C. Zhang, G. Cui, L. Chen, J. Mater. Chem. A, 2015, 3, 4092
40. J. Lu, C. Zhan, T. Wu, J. Wen, Y. Lei, A. Kropf, H. Wu, D. J. Miller, J. W. Elam, Y. Sun, X. Qiu, K. Amine Nature Communications | 5:5693 | DOI: 10.1038
41. M. Bini, G. Chiodelli, V. Massarotti, C. B. Azzoni, M. C. Mozzati, A. Comin, Phys. Chem. Chem. Phys., 2001, 3, 2162-2166
42. W. Wen, B. Ju, X. Wang, C. Wu, H. Shu, X. Yang, Electrochimica Acta 147 (2014) 271–278

43. X. Yu, J. Deng, X. Yang, J. Li, Z. Huang, B. Li, F. Kang, Nano Energy 67 (2020) 104256
44. Y. Cai, Y. Huang, X. Wang, D. Jia, W Pang, Z. Guo, Y. Du, X. Tang, Journal of Power Sources 278 (2015) 574-581
45. S. Li, K. Zhu, J. Liu, D. Zhao, X. Cui, Journal of Electrochemical Energy Conversion and Storage February 2019, Vol. 16 / 011006-1
46. K. S. Reddy, B. Gangaja, S. V. Nair, D. Santhanagopalan, Electrochimica Acta 250 (2017) 359–367
47. A. S. Grewal, K. Kumar, S. Redhu, S. Bhardwaj, Int. Res J Pharm. App Sci., 2013; 3(5):278-285
48. Y. Zhu, F. Chen, Chem. Rev. 2014, 114, 6462−6555
49. K. Raju, F. P. Nkosi, E. Viswanathan, M. K. Mathe, K. Damodaran, K. I. Ozoemena Phys.Chem.Chem.Phys., 2016, 18, 13074
50. https://wiki.anton-paar.com/en/microwave-assisted-synthesis/
51. H. Zhang, D. Liu, X. Zhang, C. Zhao, Y. X,u Solid State Electrochem (2014) 18:569–575
52. K. Raju, F. P. Nkosi, E. Viswanathan, M. K. Mathe, K. Damodaran, K. I. Ozoemena Phys.Chem.Chem.Phys., 2016, 18, 13074
53. F. P. Nkosi, C. J. Jafta, M. Kebede, L. Roux, M. K. Mathe, K. I. Ozoemena, RSC Adv., 2015, 5, 32256
54. J. Lee, N. Dupre, M. Avdeev, B. Kang, Scientific Reports volume 7, Article number: 6728 (2017)

55. Y. Gu, Y. Li, Y. Chen, H. Liu, H. Zhou, H. Wang, Y. Han, J. Zhang Int. J. Electrochem. Sci., 12 (2017) 9523 – 9532, doi: 10.20964/2017.10.48
56. Y. Xue, Z. Wang, L. Zheng, F. Yu, B. Liu, Y. Zhang, K. Ke, *Scientific Reports* volume 5, Article number: 13299 (2015)
57. H. Shiiba, N. Zettsu, M. Nakayama, S. Oishi, K. Teshima, J. Phys. Chem. C 2015, 119, 9117−9124
58. S. Tao, F. Kong, C. Wu, X. Su, T. Xiang, S. Chen, H. Hou, L. Zhang, Y. Fang, Z. Wang, W. Chu, B. Qian, L. Song, Journal of Alloys and Compounds 705 (2017) 413-419
59. F. M. Vitucci, A. Paolone, O. Palumbo, G. Greco, L. Lombardo, M. Kontje, A. Latini, S. Panero, S. Brutti J. Am. Ceram. Soc., 99 [5] 1815–1822 (2016)
60. . Liang, M. Huang, Y. Zhao, H. Wu, Y. Wang, F. Tang Int. J. Electrochem. Sci., 11 (2016) 4611 – 4618, doi: 10.20964/2016.06.14
61. J. Lu, K. S. Lee, Materials Technology: Advanced Performance Materials 2016 Vol. 31 No. 114
62. K. Lee, G. J. Yang, Y. Kim Ceramics International 43 (2017) 15510–15518
63. J. Song, D. W. Shin, Y. Lu, C. D. Amos, A. Manthiram, J. B. Goodenough, Chem. Mater. 2012, 24, 3101−3109
64. A. K. Haridas, C. S. Sharma, T. N. Rao, Electrochimica Acta 212 (2016) 500–509
65. J. Li, D. Lu, Z. Chen, H. Zeng, A. Li, Y. Cai, Ionics (2017) 23:2275–2283
66. J. Xiao , X. Chen, P. V. Sushko , M. L. Sushko , L. Kovarik, J. Feng, Z. Deng, J. Zheng , G. L. Graff , Z. Nie , D. Choi, J. Liu , J. Zhang, M. S. Whittingham Adv. Mater. 2012, 24, 2109–2116

67. C. J. Jafta, M. K. Mathe, N. Manyala, W. D. Roos, K. I. Ozoemena, ACS Appl. Mater. Interfaces 2013, 5, 7592−7598
68. J. Yang, X. Han, X. Zhang, F. Cheng, J. Chen, Nano Research 2013, 6(9): 679–687
69. G. Liu, L. Zhang, L. Sun, L. Wang, Materials Research Bulletin 48 (2013) 4960–4962
70. Y. Li, Q. Zhang, T. Xu, D. Wang, D. Pan, H. Zhao, Y. Ba, Ceramics International 44 (2018) 4058–4066
71. N. D. Rosedhi, N. H. Idris, M. M. Rahman, M. F. Md Din, J. Wang, Electrochimica Acta 206 (2016) 374–380
72. C. Liu, Z. G. Neale and G. Cao, Materials today, Volume 19, Number 2, March 2016

CHAPTER 3

Experimental Method

3.1 Introduction

The materials used for the synthesis of the cathode materials, characterization techniques for analyzing the materials, electrode preparation, coin cell assembly and electrochemical measurement are outline below:

3.2 Chemicals and Materials

Outlined below are all the chemicals and materials used in this thesis work. All the chemicals are used as delivered:

- Commercial LMO (purchased from China)
- Manganese sulphate monohydrate ($MnSO_4.H_2O$), Sigma-Adrich, ACS reagent, ≥98%
- Lithium Nitrate ($LiNO_3$), Sigma Aldrich, ReagentPlus
- Sodium Nitrate ($NaNO_3$) Saarchem, AR
- Sulphuric acid (H_2SO_4), ace (associate chemical enterprises) 98%
- Lithium Hydroxide (LiOH) reagent ≥98%
- $[Ni(NO_3)_2{\cdot}6H_2O]$, 99.999 %
- Polyvinylidene fluoride (PVDF), MTI Corp
- Carbon black super C45: conductive additive, MTI

- N-methyl-2-pyyolidone (NMP), MTI
- Separator: Celgard H1612/16 μm
- Lithium hexafluorophosphate (LiPF6),
- Diethyl carbonate (DEC) $OC(OCH_2CH_3)_2$
- Dimethyl carbonate (DMC) $OC(OCH_3)_2$
- Ethylene carbonate (EC) $(CH_2O)_2CO$ Dongguan Shanshan Battery Materials Co. Ltd

3.3 Synthesis of the cathode materials

3.3.1 Synthesis of LMO-microwave (LMO-m) by microwave irradiation

Microwave irradiation was used to synthesis LMO-m by the addition of distilled water (50ml) to a weighed quantity of the commercial LMO-pristine (LMO-p). The mixture was stirred properly using a magnetic stirrer and then subjected to microwave (Anton Paar Multiwave 3000) irradiation at 600 W for 60 min. After which the mixture is dried in an oven to obtain the product: LMO-m as illustrated in Figure 3.1.

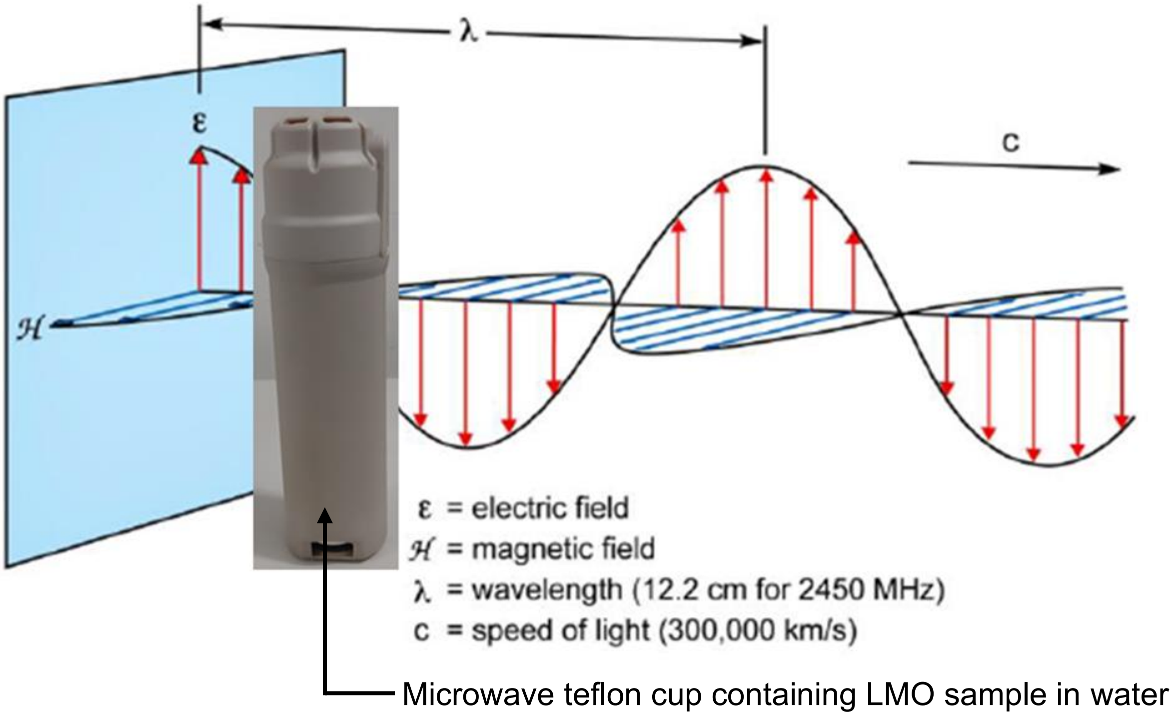

Microwave teflon cup containing LMO sample in water

Figure 3.1: Schematic diagram of microwave irradiation synthesis [1]

3.3.2 Synthesis of LMNO nanorods

3.3.2.1 Synthesis of the precursors: β-$MnO_{2-\delta}$ nanorods

Weight ratio 1:5:10 of the $MnSO_4$, $LiNO_3$ and $NaNO_3$ respectively were grounded using a mortar and pestle. The mix was heated in a tube furnace at 385 ^oC (2.0 hr) under

1. Argon (5%)/hydrogen (95) atmosphere to obtain the precursor: β-$MnO_{2-\delta}$ (Ar) nanorods
2. Hydrogen (100%) atmosphere to obtain the precursor: β-$MnO_{2-\delta}$ (H_2) nanorods

The two products were allowed to cool naturally under their respective prevailing atmospheres. Then the samples were washed severally with distilled water and dilute H_2SO_4 acid; and dried at 90^{o}C overnight [2, 3].

3.3.2.2 Synthesis of LMNO nanorods (LMNO-Ar and LMNO-H_2)

The LMNO nanorods were synthesized by the modified solid-state reaction [4]The molar ratio of 1.5:0.5:1.05 of β-$MnO_{2-δ}$ (H_2) nanorods, $Ni(NO_3)_2·6H_2O$ and LiOH were dispersed in ultra-pure. It was then stirred with a magnetic stirrer and dried in the oven at 80°C. The dried sample was heated to 700°C and maintained for 18 hr in air to obtain the product LMNO-H_2. The synthesis of the LMNO-Ar followed the same procedure as LMNO-H_2, except for the precursor: β-$MnO_{2-δ}$ (Ar) nanorods that were used (schematically illustrated in Figure 3.2).

.

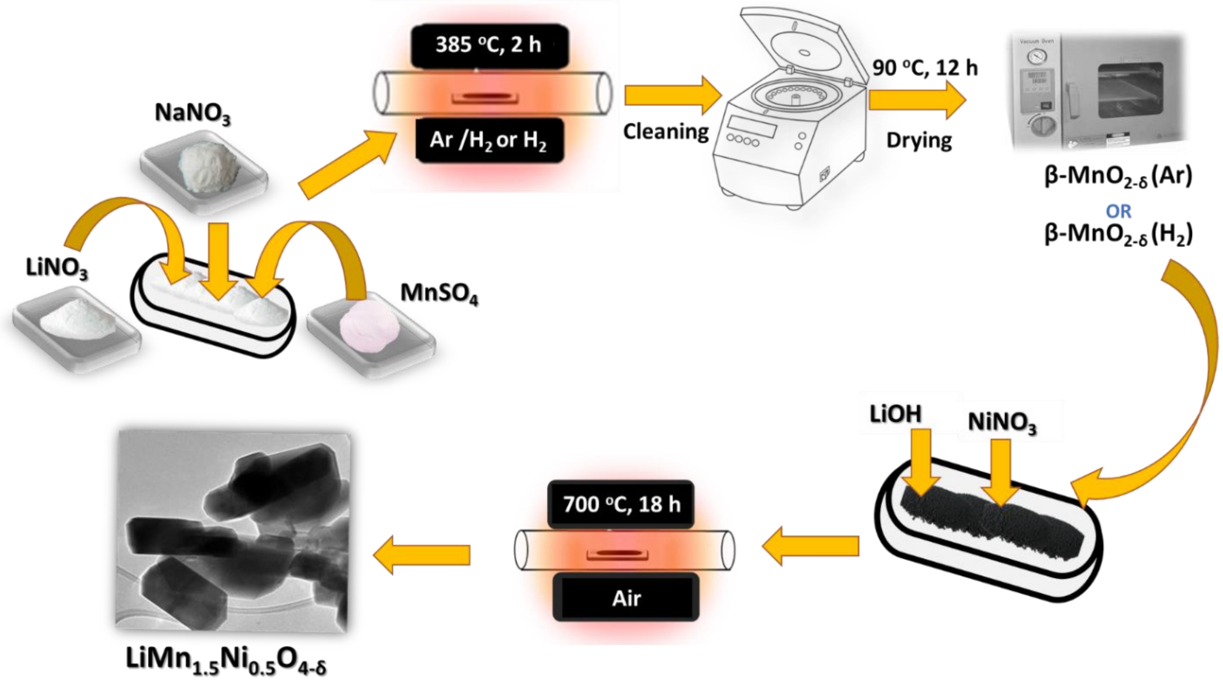

Figure 3.2: **S**chematic representation of the experimental design

The understated analytical techniques were used to characterize the prepared samples at room temperature:

- Powder X-ray Diffraction (SPXRD)

- Powder Neutron Diffraction (PND)
- Synchrotron X-ray Photoelectron Spectroscopy (SXPS)
- Nuclear Magnetic Resonance (NMR)
- X-ray Absorption Near Edge Structure (*XANES*)
- Raman Spectroscopy (RS)
- Transmission Electron Microscopy (TEM)
- Scanning Electron Microscopy (SEM) Characterization
- Nitrogen Gas Adsorption analysis
- Fourier-transform infrared spectroscopy (F-TIR)

3.4 Materials Analysis

3.4.1 Synchrotron Powder X-ray Diffraction (PXRD)

For this research work, the PXRD was carried using Bruker D2 diffractometer 580 equipped with Cu Kα radiation (λ = 1.54178 Å)

3.4.2 Powder Neutron Diffraction (PND)

The PND analysis was done at the NECSA SOC Limited, South Africa. The high-performance neutron diffraction instrument, PITSI was used to obtain the data at room temperature. The wavelength of 1.08 Å was used in Goniometer: 4 position-changer; sample rotated continuously with detector bank step size of 17^o (4-10 hr per step) and slit insert 5 x 35 mm on a 2θ range covering 10 to 115°.

3.4.3 Synchrotron X-ray Photoelectron Spectroscopy (SXPS)

Synchrotron XRD measurements were carried out at the XPD beamline of the LNLS synchrotron facility (Brazil). Measurements were conducted using a custom-built furnace operating in reflection mode geometry using a beam energy of 7.5 KeV and a Mythen strip detector. For all SXRD data presented here, the crystalline phase identification was done using DIFFRAC.EVA (Version 2. Release 2014) using the ICDD PDF2 database (Release 2016). Phase quantification was done using the Rietveld method as implemented in Bruker AXS TOPAS software (Version 5, 2014).

3.4.4 Nuclear magnetic resonance (NMR)

The ^{7}Li MAS (NMR) analysis of the LMO and LMNO samples was carried out using Bruker Avance-500 spectroscopy. The NMR spectra provided detailed information on the local structure of the two samples.

3.4.5 X-ray absorption near edge structure (XANES)

The XANES analysis at the Mn K-edge (8333 eV) and Ni K-edge (6539 eV) were performed at the D06A-DXAS beamline of the LNLS synchrotron facility (Brazil). DXAS is a dispersive beamline equipped with a focusing curved Si (111) monochromator, operating in Bragg mode, that selects the x-ray energy bandwidth (11 400–12 000 eV), with a 1152 × 1242 (500 × 900) pixel CCD solid-state detector that converts x-rays

into visible light for spectral analysis. The monochromator was calibrated with Ni and Mn foils prior to each measurement. Extraction of the XANES signal as well as the LCF`s from the measured absorption spectra was carried out using the Demeter software package

3.4.6 Raman Spectroscopy (RS)

Raman spectroscopy (RS) was used to study the vibrational information measurements of the LMO and LMNO samples. The 514.5 nm line of an argon-ion laser and a Horiba Jobin-Yvon LabRAM HR Raman spectrometer equipped with an Olympus BX41 microscope attachment was used to obtain the Raman spectra. The LabSpec v5 software was used to capture the data.

3.4.7 Fourier-transform infrared spectroscopy (F-TIR)

The F-TIR spectra were recorded using a Thermo Nicolet 6700 F-TIR spectrometer.

3.4.8 Transmission Electron Microscopy (TEM)

The images of the LMNO samples was captured using FEI Tecnai T12 Sprint TEM instrument

3.4.9 Nitrogen Gas Adsorption analysis

The surface area of the samples was determined by the Micrometric Tristar 3000 BET. The N_2 adsorption–desorption analysis was conducted at -195 °C. Preceding the analysis, the sample was outgassed at 150 ℃ for 4 h under nitrogen gas. The Nitrogen Gas Adsorption surface areas were obtained from the adsorption data in a relative pressure range from 0.05 to 0.30.The instrument provides data for the surface area and pore sizes of the LMO and LMNO samples.

3.4.10 Scanning Electron Microscopy (SEM)

The images of the LMOs was captured using the FEI Nova Nanolab 600 SEM Instrument.

3.5 Assembling and electrochemical characterization of coin cells

3.5.1 Fabrication of the LMO cathode materials coin cells

The LMO cathode laminate was fabricated by mixing a slurry containing 70% LMO, 20% conductive additive and 10% PVDF in NMP. The prepared mix was pasted on aluminum current collector and vacuum dried at 110ºC for 12 h. The dried laminate was then punched into 12 mm disc for coin cells assembly and transferred into the glovebox. The cells were assembled in the glovebox using Li foil as anode. $LiPF_6$ (1 M) in EC/DEC/DMC (volume ratio 1:1:1) electrolyte and a micro-porous polypropylene Celgard H1612/16 µm separator were used. The coin cells remained in the glovebox overnight before they were taken out for electrochemical measurements. BioLogic system (BCS-8xx series) was used to carry out the electrochemical measurements: CV, GC-D and EIS. BT-Lab program was used for data acquisition and analysis.

3.5.2 Fabrication of the LMNO cathode materials coin cells

The LMNO materials coin cells were fabricated the same way as the LMO, except the slurry that contained 80% LMNO, 10% conductive additive and 10% PVDF in NMP.

3.6 Reference

1. Microwave Chemistry in Organic Synthesis (By A. Bacher, UCLA, 4-30-2016)
2. N. Sui, Y. Duan, X. Jiao, D. Chen *J. Phys. Chem. C* 2009, *113,* 8560–8565
3. F. Cheng, T. Zhang, Y. Zhang, J. Du, X. Han and J. Chen, *Angew. Chem. Int.* Ed. 2013, 52, 2474 –2477
4. J. Yang, X. Zhang, Z. Zhu, F. Cheng, J. Chen, *Journal of Electroanalytical Chemistry* 688 (2013) 113–117

CHAPTER 4

Effects of microwave irradiation on physical and electrochemical properties of Spinel $LiMn_2O_4$ Cathode Material

4.1 Introduction

The cathode is described as the capacity-determining factor of the L-IBs [1]. Cathode materials are required to have high specific capacity and high working voltage, low cost, high safety and long cycle life for eVs [1]. Among the cathode materials for rechargeable L-IBs, the spinel $LiMn_2O_4$ (LMO) has emerged as one of its the most widely researched because of low cost, low toxicity and high safety [2, 3-6, 7].

The structure of model LMO is a cubic spinel and its crystallographic has been discussed in section 2

The Li^+ insertion during the discharge process lowers the average valency of Mn ions to less than +3.5, because of the presence of more than 50% Mn^{3+} [2, 5, 6]. The emergent of the high spin Mn^{3+}: d^4 results in a cubic to tetrahedral phase transition. This cubic-to-tetragonal transition (J-T distortion) leads to an increase of 6.5% in the unit cell volume and the Li insertion capacity is decreased. The J-T distortion caused reduction in the capacity of the cathode material during cycling [5, 6, 7, 10]. Consequently, improving the electrochemical performance of LMO it is imperative to suppress the J-T distortion.

Previous reports stated that the proportions of Mn^{3+} and Mn^{4+} have great consequences on the electrochemical properties of the LMO [4, 11]. Therefore, an appropriate increase in the ratio $r = [Mn^{4+}]/[Mn^{3+}]$ can suppress the J-T distortion [4]. It should be noted that r can be increased by the addition of excess Li (y) to the stoichiometry spinel $LiMn_2O_4$ which results in the formula: $Li[Li_yMn_{2-y}]O_4$ [4, 11],

(i) when $(y = 0)$, we have the stoichiometry: $[Li]_{tetra}[Mn^{3+}\ Mn^{4+}]_{octa}$ and $r = 1$

(ii) when $(y > 0)$, we have Li-excess: $[Li]_{tetra}[Li_yMn_{1-3y}{}^{3+}\ Mn_{1+2y}{}^{4+}]_{octa}O_4$ and $r > 1$

(iii) when $(y < 0)$, we have Li-poor: $[Li_{1-|y|}Mn_{|y|}{}^{2+}]_{tetra}[Mn_{1+|y|}{}^{3+}Mn_{1-|y|}{}^{4+}]_{octa}O_4$ and $r < 1$

Thackeray's group [12] stated that the reduction of Mn^{3+} content in the spinel LMO cathode materials can be used to suppress the J-T distortion. They proposed the understated three strategies to increase the value of r:

(i) Synthesis of stoichiometry spinel LMO: $Li_{1+y}Mn_{2-y}O_4$.

(ii) Dope a multivalent metal cation to replace a small amount of manganese ($LiM_yMn_{2-y}O_4$).

(iii) Synthesis of defect spinel (cation-deficient): $Li_{1-y}Mn_{2-2y}O_4$.

Several research works have been carried out to overcome the J-T distortion effect. One of the most reported strategies is the doping of the Mn sites ($LiM_yMn_{2-y}O_4$) to decrease the Mn^{3+} content (increased mean Mn valency). However, these strategies usually cause a decrease in capacity [5, 7, 9, 11, 13-16].

Sequel to the above challenge, this study explores an alternative to increasing the value of r ($[Mn^{4+}]/[Mn^{3+}]$) in LMO without a decrease in the specific capacity. The use of microwave irradiation is therefore proposed as a strategy to enhance the physico-chemical properties
(e.g. structural stability, $r = [Mn^{4+}]/[Mn^{3+}]$ and increase the average Mn oxidation state) and electrochemical redox reaction (e.g. the reversibility of anodic and cathodic current peaks Ipa/Ipc, ΔE_{pp} / V**)** of LMO without the need for doping with foreign ions or surface coating. This has been shown by XPS, NMR, CV, GCD, TGA, etc This is the first time that it will be reported that microwave irradiation is being used to increase $r = [Mn^{4+}]/[Mn^{3+}]$ in LMO without the doping of foreign ions and decrease in the initial specific capacity.

4.2 Results and discussions

4.2.1 Thermogravimetric Analysis (TGA)

The thermal stabilities of LMO-p and LMO-m were investigated by the TGA. The TGA profiles of LMO-p and LMO-m samples (Figure 4.1) shows three stages of weight loss. The LMO-p shows a sharp weight loss in stage 1 (~ 125 °C to ~ 300 °C), less weight loss in stage 2 (~ 300 °C to 700 °C) and a sharp loss in stage 3 (~ 700 °C to ~ 900 °C). Compare to LMO-p, the LMO-m shows a steady weight loss from stage 1 to 3. The overall weight loss in LMO-p (11.3 %) is greater than in LMO-m (10.2%), It can therefore be concluded that the microwave irradiation has improved the thermal stability of the LMO-p.

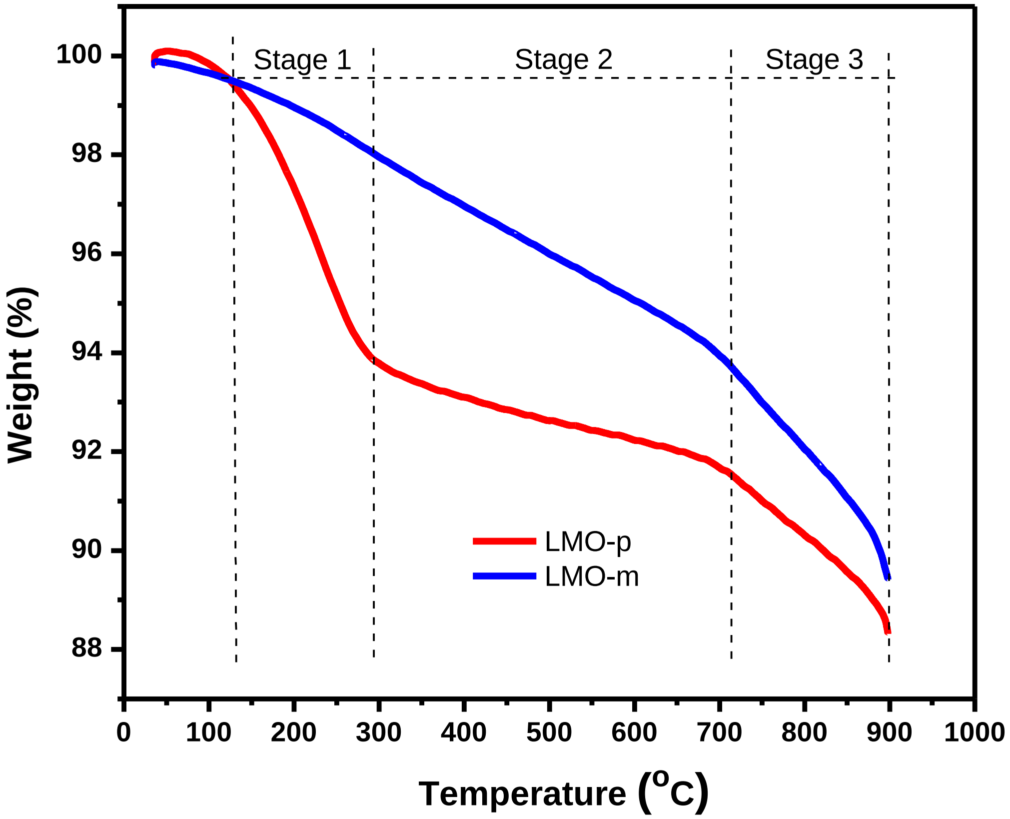

Figure 4.1: TGA curves of LMO-p and LMO-m

4.2.2 Synchrotron Powder X-ray Diffraction (SPXRD)

The SPXRD of LMO-p and LMO-m samples: Figure 4.2 (a and b). The diffraction peaks observed can be assigned to the Fd-3m symmetry (ICDD number. 00-035-0782). There was no secondary phase that was observed for both samples. Hence, pure and well-crystallized $LiMn_2O_4$ phase can be produced with microwave irradiation.

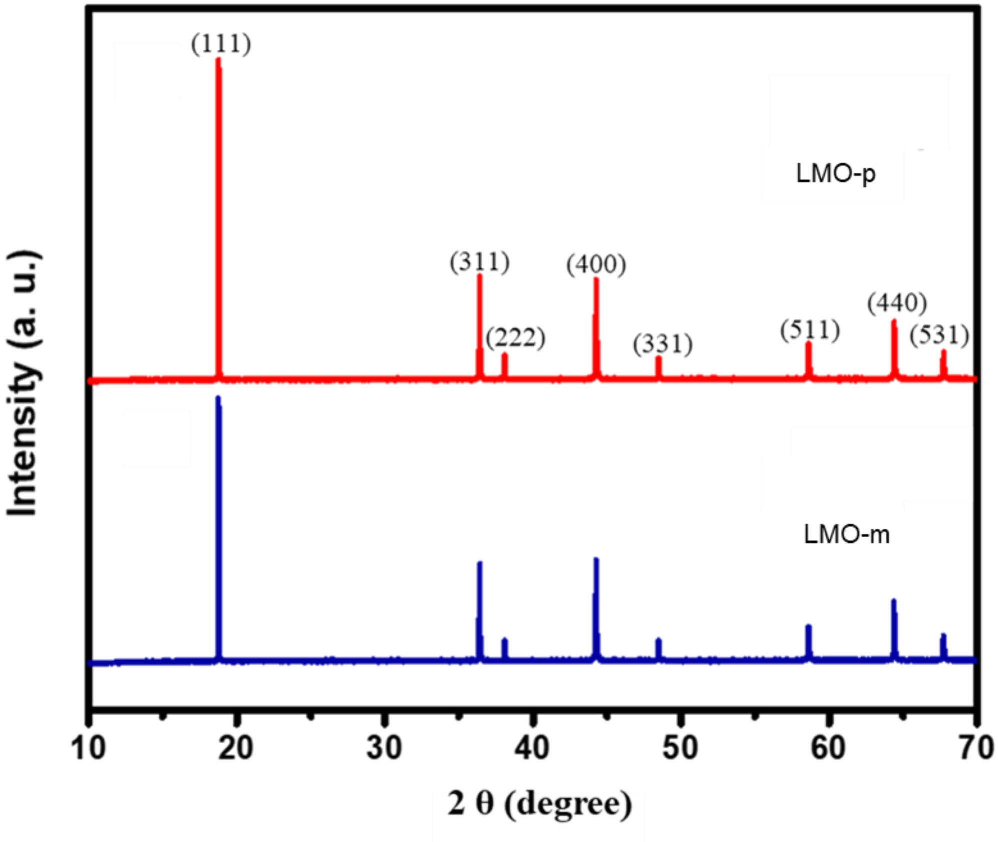

Figure 4.2: SPXRD patterns of (a) LMO-p and (b) LMO-m

Table 4.1: Crystal parameters of LMO-p and LMO-m

Sample	Space	Lattice constant (Aº)	Cell volume (Aº^3)
LMO-p	Fd3 m	8.1854	548.44
LMO-m	Fd3 m	8.1828	547.92

Table 4.1 displays the Rietveld refinement data for the two samples. The result shows that the lattice parameter of LMO-p (8.1854 Aº) is higher than that of LMO-m (8.1828 Aº). The increased lattice parameter is as a result of the higher Mn^{3+} content in LMO-p. This is because the Mn^{3+} (high spin: 0.645 Aº) is higher than that of Mn^{4+} (0.53 Aº) [18].

Therefore, it can be suggested that the microwave irradiation has reduced the Mn^{3+} content in LMO-m.

4.2.3 Nitrogen Gas Adsorption analysis

Table 4.2 shows that the LMO-m has a larger surface area, pores volume and size than the LMO-p. The LMO-m sample's larger surface area will provide it with a higher contact area with the electrolyte than LMO-p and thus there will be higher Li^+ flux across its interface which will boost its discharge capacity.

Table 4.2: Nitrogen Gas Adsorption analysis of LMO-p and LMO-m

	Surface-area (m^2g^{-1})	**Pore-volume (cm^3g^{-1})**	**Pore-size (nm)**
LMO-p	28.88	0.026	3.59
LMO-m	30.59	0.029	3.76

Also, the larger pore size of LMO-m will favored Li^+ transport more than that of the LMO-p because its structure would be maintained even when SEI film is formed during charge/discharge processes better the LMO-p sample's smaller pore size [19]. Hence LMO-m is expected to have better electrochemical properties than LMO-p.

4.2.4 Synchrotron X-ray photoelectron spectroscopy (SXPS)

The SXPS is a very useful method to examine surface elements of the two samples (LMO-p and LMO-m) by specifying the binding energies and oxidations states [20]. Figure 4.3 shows the splitting of the spin-orbit made of the Mn2p into two oxidation states of $Mn2p_{3/2}$

at 642.33 eV and Mn2p$_{1/2}$ at 653.89 eV. The difference in their binding energies is 11.6 eV. As similar value has been published by some authors [20].

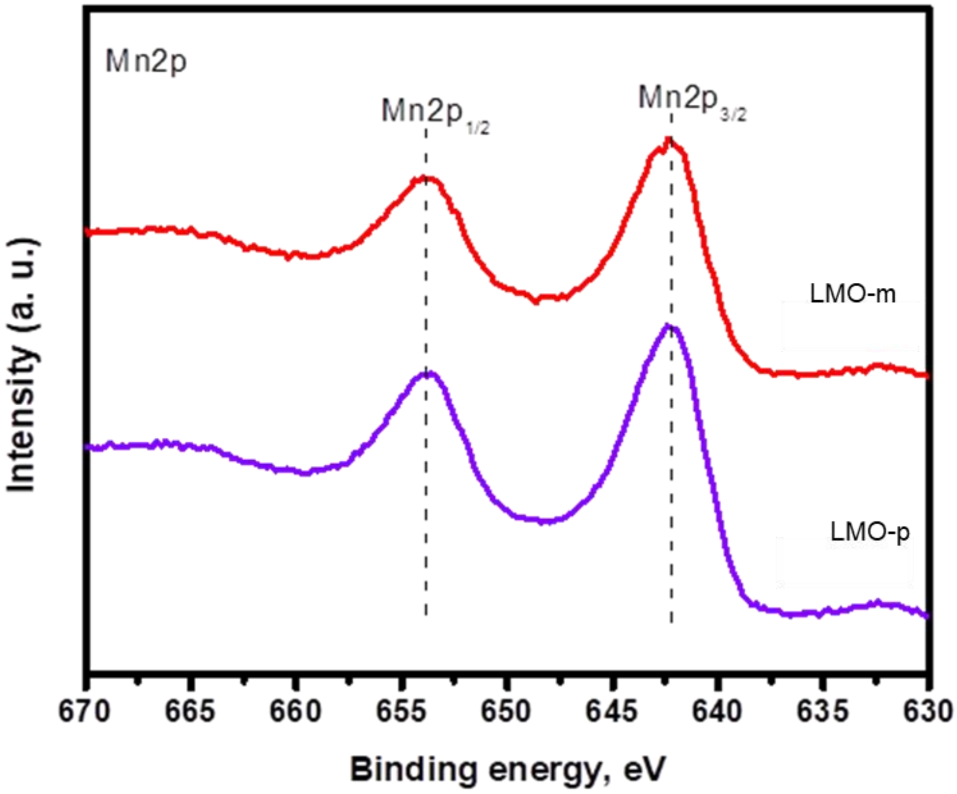

Figure 4.3: SXPS 2p Mn spectra of LMO-p and LMO-m

The average oxidation state of Mn in the two samples: LMO-p and LMO-m can be obtained from the XPS peaks. The 2p$_{3/2}$ Mn peak binding energy values for Mn^{3+} and Mn^{4+} in LMO-p are 641.7 and 643.4 eV respectively; and in LMO-m are 641.9 and 643.1 eV respectively. Figures 4.4 (a and b) show the amount of the Mn ions in the two samples' surface (LMO-p and LMO-m). From Table 4.3, the LMO-p has Mn^{3+} (58%) and Mn^{4+} (42%) while the LMO-m has Mn^{3+} (43%) and Mn^{4+} (57%). The values of r = [Mn^{4+}]/[Mn^{3+}] for LMO-p and LMO-m are 0.72 and 1.33 respectively. Hence the r value for the LMO-m is higher than that of LMO-p. The average Mn valences in LMO-p and LMO-m is 3.4 and

3.6 respectively. This result shows that Mn^{4+} content in LMO-m is higher than of LMO-p which is further corroborated with the NMR spectra in the next sub-section. The increased in the average Mn valency in LMO-m could be traced to the low valent Li^{+} substitution into the Mn-sites. Thackeray's group has reported the use of neutron diffraction studies to confirm that about 15% of Li^{+} can be substituted into the Mn sites in the nominal composition of the $LiMn_2O_4$ [21].

Table 4.3: SXPS Mn $2p_{3/2}$ fitted data

	Binding energy (eV)		**Atomic % of Mn spices**				
	Mn^{+3}	**Mn^{4+}**	**Mn^{+3}**	**Mn^{4+}**	**Mn^{3+}/Mn^{4+}**	**Mn^{4+}/Mn^{3+}**	**Mn valency**
LMO-p	643.4	641.7	58	42	1.38	0.72	3.4
LMO-m	643.1	641.9	43	57	0.75	1.33	3.6

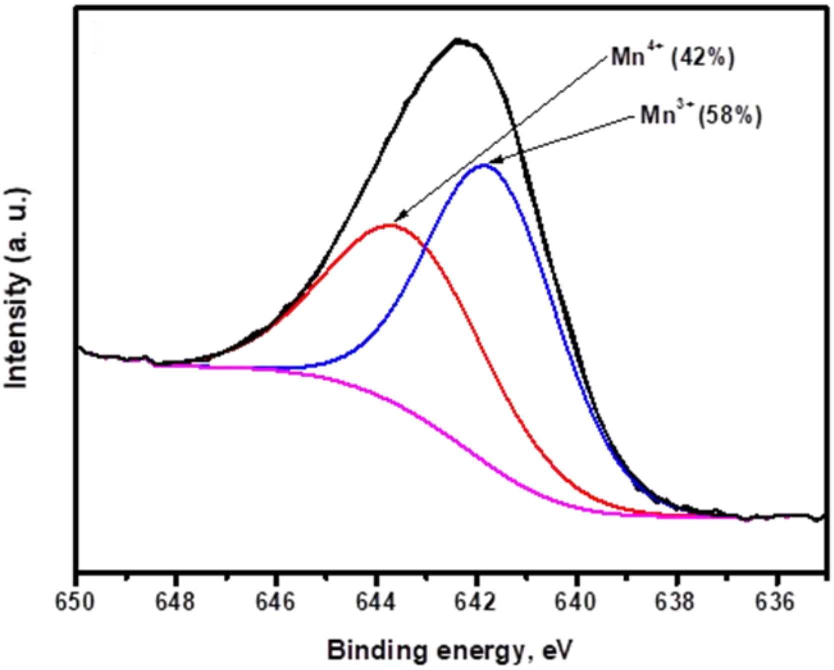

Figure 4.4a: SXPS 2p$_{3/2}$ Mn 2p$_{3/2}$ spectrum of the LMO-p

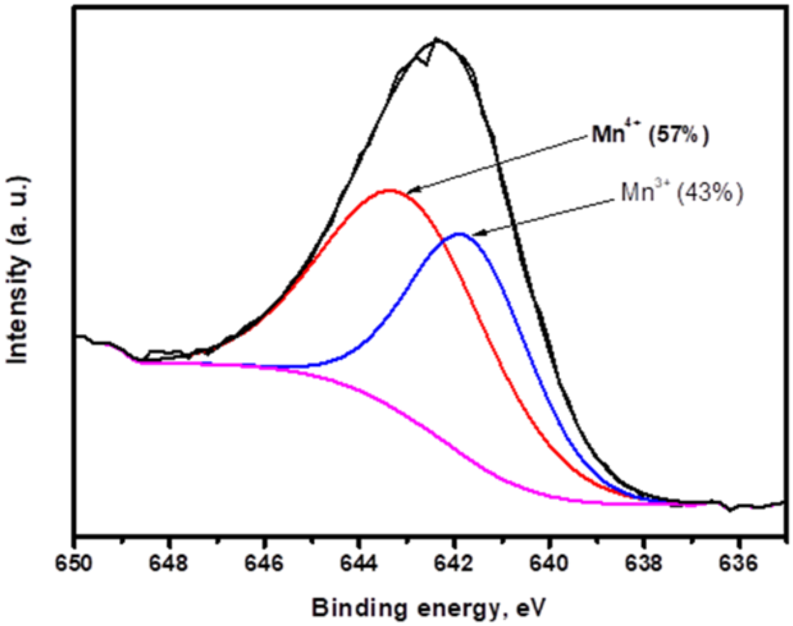

Figure 4.4b: 2p$_{3/2}$ SXPS Mn spectrum of the LMO-m

4.2.5 Nuclear magnetic resonance (NMR)

Li NMR is used to investigate the local environments of the Li-ions and cation involved in the redox processes. In this work ^{7}Li NMR analyses are used to examine the microwave irradiation effect on the local environments surrounding Li-ions in LMO-p and LMO-m. The ^{7}Li NMR spectra (Figure 4.5) of LMO-p and LMO-m show large shifts of the resonances typical of paramagnetic solids which are different compare to the shift position characteristically obtained for diamagnetic solids around 0 ppm and large spinning sideband manifolds [23].

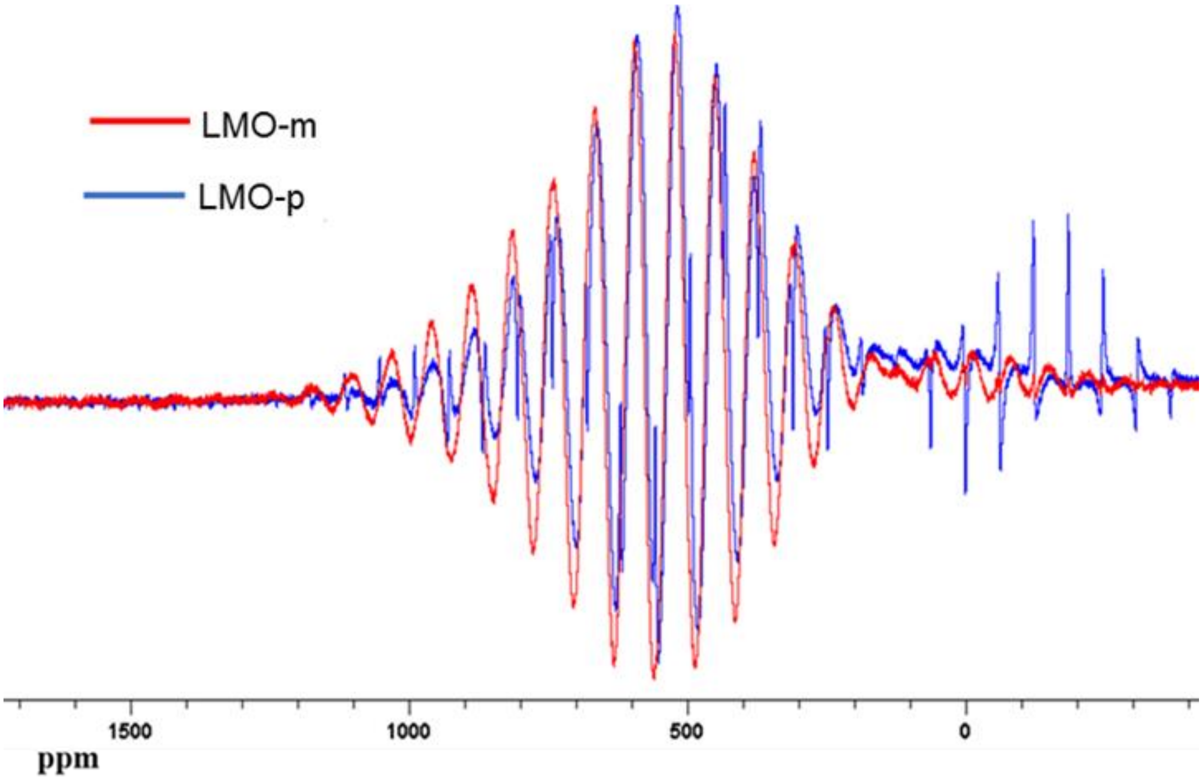

Figure 4.5: ^{7}Li MAS NMR spectra LMO-p and LMO-m

Figure 4.6 shows ^{7}Li MAS NMR spectrum of LMO-p. Peaks (590, 518.7 and 448.1 ppm) have smaller shoulders at the lower shift (558.1, 495.6 and 432.5 ppm respectively) and peaks (590, 662.5 and 735.0 ppm) have smaller shoulders at the higher shift (620.6, 683.1 and 746.9 ppm) respectively.

This occurrence is similar to the spectra published by Tucker in their study of metal-substituted lithium manganese oxide spinels [25] These shoulders are absent in the LMO-m, the collapse of these smaller shoulders in LMO-p into the main spinel resonance in LMO-m is because of the lithium-ion motion in the cathode material during the microwave irradiation [6]. Furthermore, the intensity of the LMO-m resonance grows

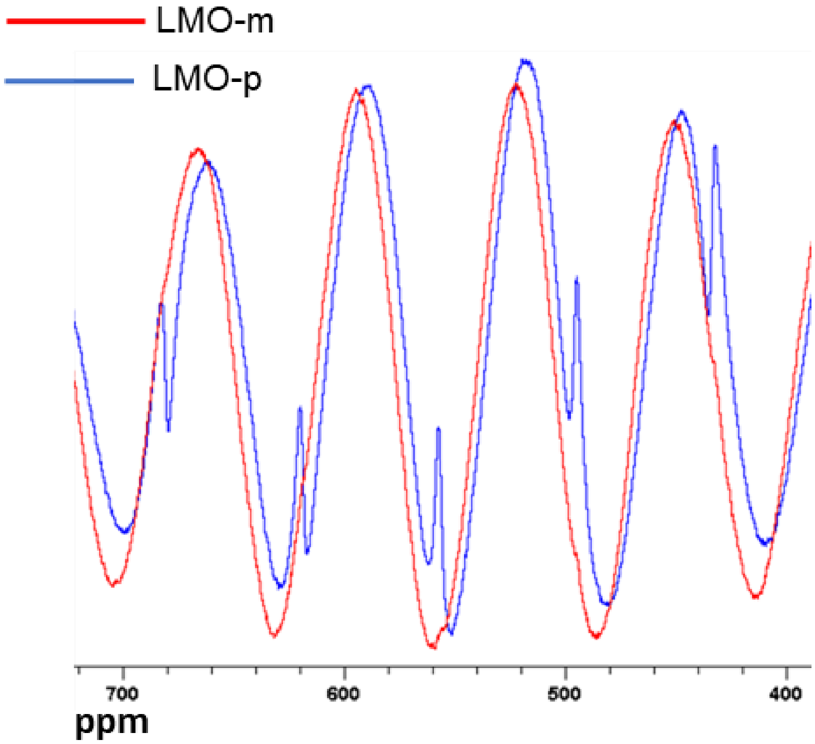

Figure 4.6: ^{7}Li MAS NMR spectra illustration of different local environment of Li$^+$ in LMO-p and LMO-m

as the resonances shift to a higher frequency. Previous researchers reported that resonances around 520 ppm can be assigned to Li in (8a) having the Mn oxidation state as 3.5 [24, 26]. Therefore, the LMO-p and LMO-m resonances at 518.7 and 522.5 ppm respectively (Figure 4.7) which can be assigned to the tetrahedral lithium in the normal cubic lattice site: 8a (herein called normal lithium peak) [24, 25]. Similar observations have been reported by Lee et al. [24] and Morgan et al [26]. Lee et al. [24] reported that Li in the tetrahedral sites of Mn^{3+}, $Mn^{3.5+}$, and Mn^{4+} resulted in shifts of 100-850 ppm and that the magnitude of the shift increase as a function of the manganese oxidation state [12, 24]. The shift to higher frequency is consistent with increasing Mn oxidation [27]. The LMO-p and LMO-m peaks at 590.0 and 595.0 ppm respectively, originate from lithium in the 8a site in close proximity to lattice defects (i.e.,, Li-for-Mn substitution or Mn vacancy) and herein refers to near-defect lithium peak [24, 25]. The slight shift of the peaks to lower frequencies is attributed to the increased Mn^{3+} content in the LMO [24, 28] . Therefore, the LMO-p has more Mn^{3+} content (448.7 ppm) than LMO-m (451.2 ppm). Also, the peaks of LMO-p and LMO-m at 590 ppm and 595.0 ppm respectively show that the microwave effect has caused more Mn^{4+} content in the LMO- m. This is in agreement with the SXPS and Mn edge: LCF fit.

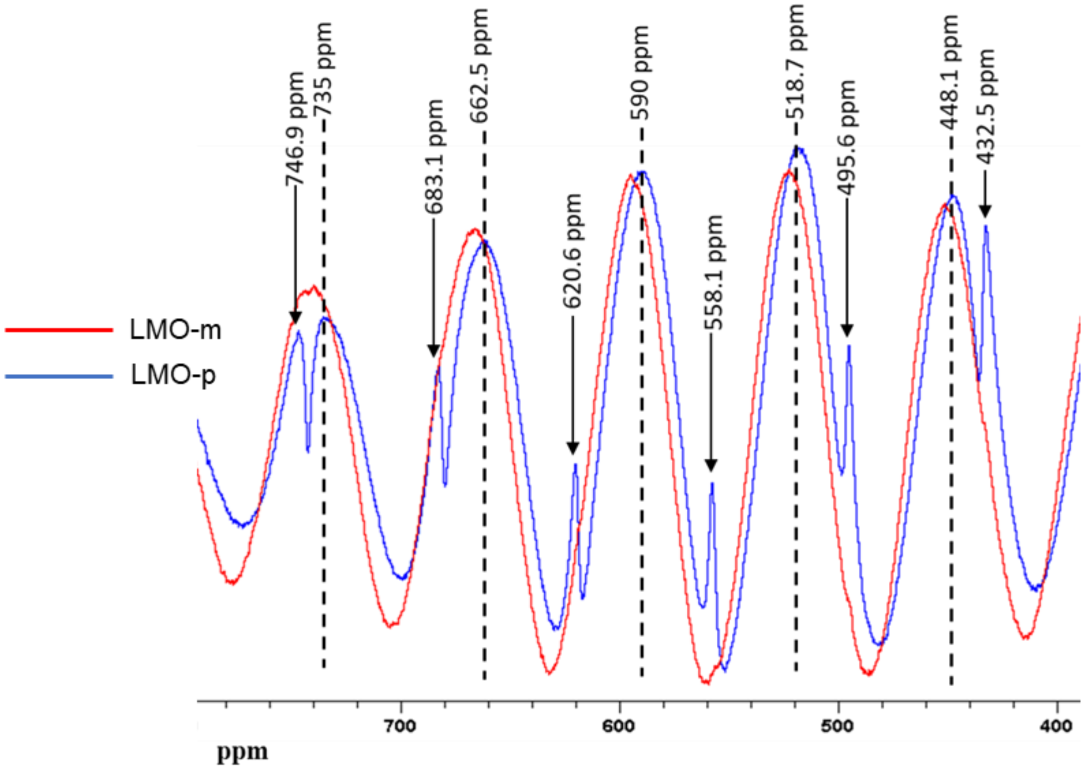

Figure 4.7: ^{7}Li MAS NMR spectra illustration (magnified) of the different local environment of Li^+ in LMO-p and LMO-m

Tucker [25, 29] and Gee [30] published that the key shift mechanism in LMO materials is the supertransferred hyperfine interaction between unpaired manganese d electrons and the lithium nucleus. Tucker [25] stated that transition metal t_{2g} unpaired electron density can move to the lithium orbitals in a bent Li-O-Mn bond, resulting in a shift of the lithium resonance to a higher frequency. But for a partially filled e_g orbital, unpaired spin density can only move to the lithium orbitals in a linear Li-O-Mn arrangement, because of geometric constraints of the oxygen p-metal d orbital overlap. This arrangement results in a shift of the lithium resonance to lower frequency. Going by Tucker et al. [25] conclusion from their findings on Cr-substituted lithium manganese oxide study, it can be inferred that microwave irradiation has increased the unpaired t_{2g} electron density in the LMO-m, thus an overall increase in the Mn^{4+} electron character, thereby increased the lithium chemical shift from 590 ppm (LMO-p) to 595 ppm (LMO-m). Therefore, we can conclude that microwave irradiation decreased local unpaired e_g electron density (Mn^{3+}) without decreasing local unpaired t_{2g} (Mn^{4+}) electron density.

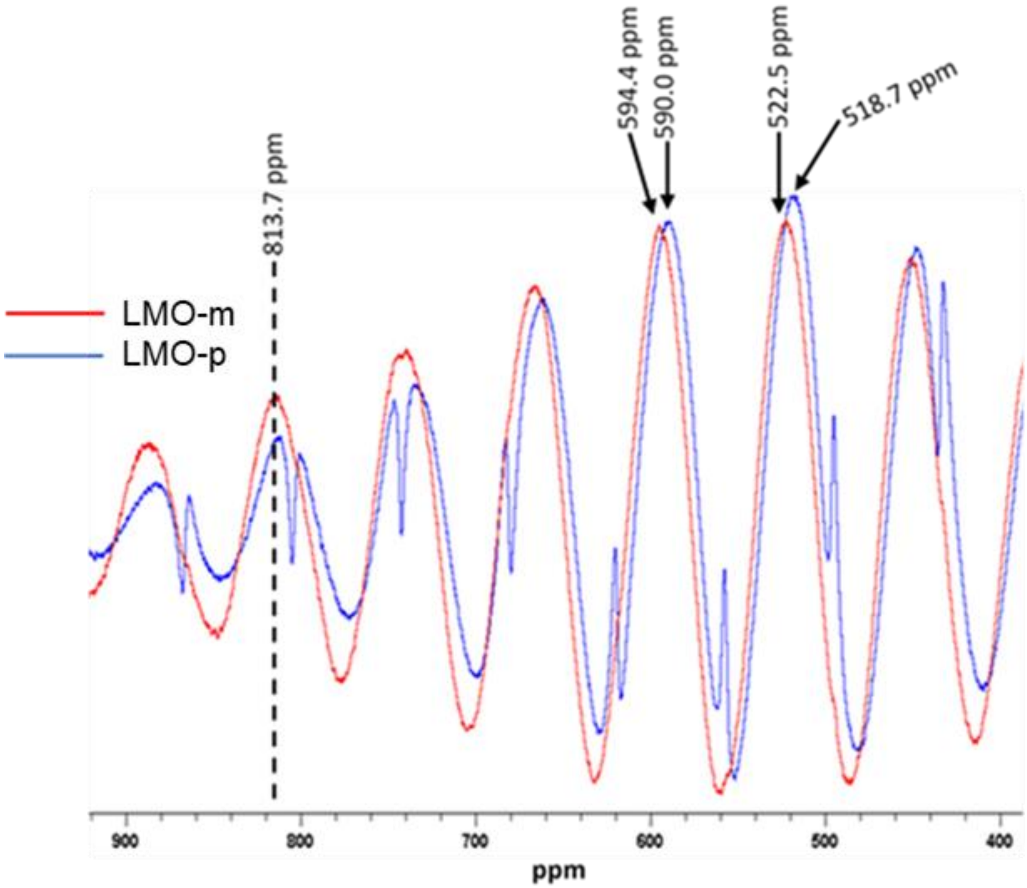

Figure 4.8: ^{7}Li MAS NMR spectra illustration of the different tetrahedral site of spinel Mn^{4+} in LMO-p and LMO-m.

Furthermore, the peaks in the high frequency region (around 800 ppm) are due to lithium spins in the tetrahedral site of spinel Mn^{4+} [24, 28], hence the broader high-frequency resonance observed at 813.7 ppm (Figure 4.8) for the LMO-m shows that the microwave irradiation causes a further increase in Mn^{4+} concentration around Li-ion [31].

4.2.6 Powder Neutron Diffraction (PND)

The changes in the structural spinel of LMO-p and LMO: m were analyzed by PND measurements. Figures 4.9 (a) and (b) show the Rietveld refinement patterns of the PND data of spinel- LMO-p and LMO: m respectively. The profiles of the Rietveld fits to the PND data for LMO-p and LMO: m samples are very similar, but the effects of microwave irradiation resulted in LMO: m sample having higher intensities for all the reflections as shown in Figure 4.10. The neutron Rietveld refinement shows that the microwave irradiation has reduced the lattice parameter from 8.2127 A^o in LMO-p to 8.2123 A^o in LMO-m. The decrease in lattice parameter with the microwave irradiation may be as a result of the LMO-m sample having more Mn^{4+} content than LMO-p sample because Mn^{4+} has an ionic radius (0.53 A°) which is lesser than the low spin Mn^{3+} (0.58 A°) and high spin Mn^{3+} (0.65 A°) , [2]. Hence the PND result has also shown that the microwave irradiation has reduce the Mn^{3+} content in spinel LMO-p as reveal by SPXRD, SXPS and NMR analytical results.

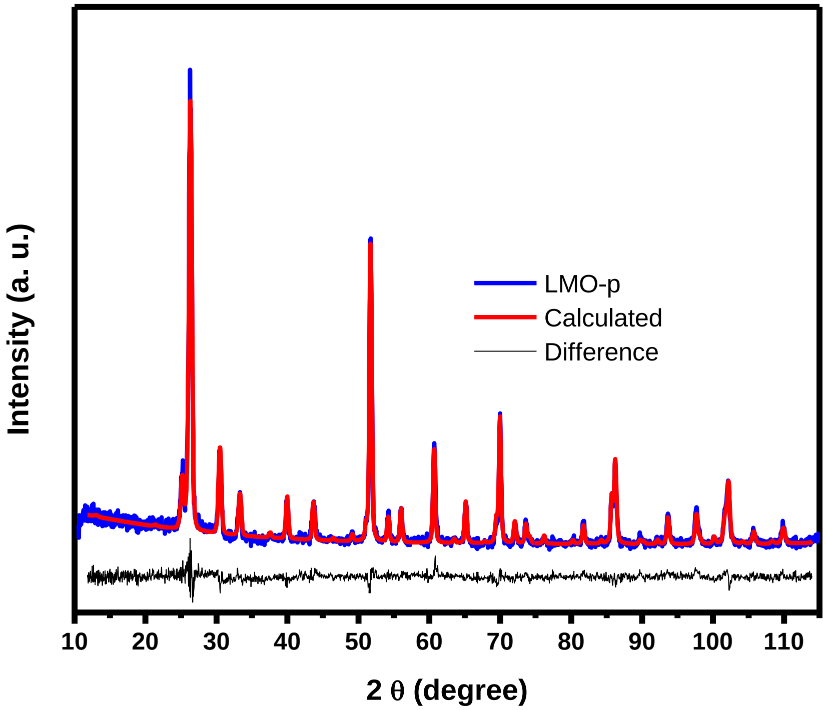

Figure 4.9a: Rietveld fit of PND data for: LMO-p

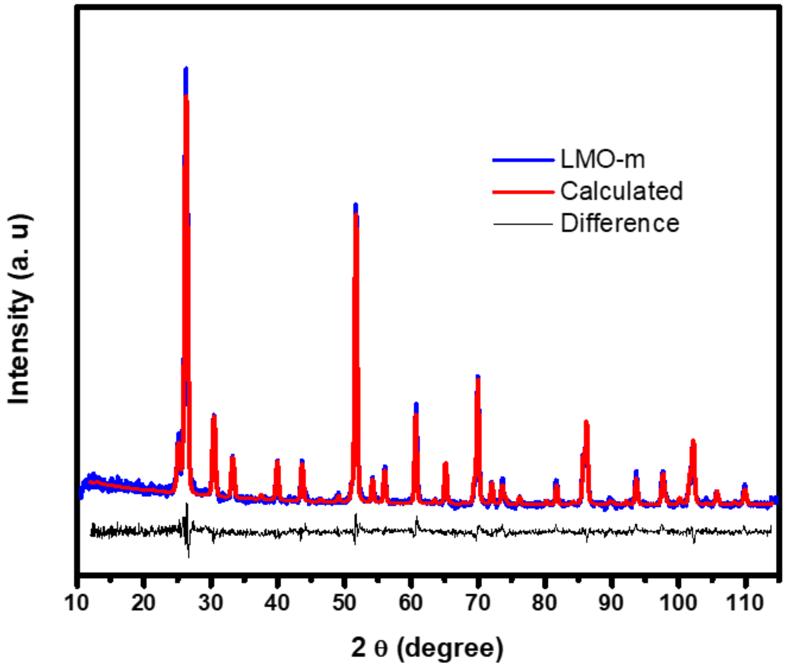

Figure 4.9b: Rietveld fit of PND data for: LMO-m

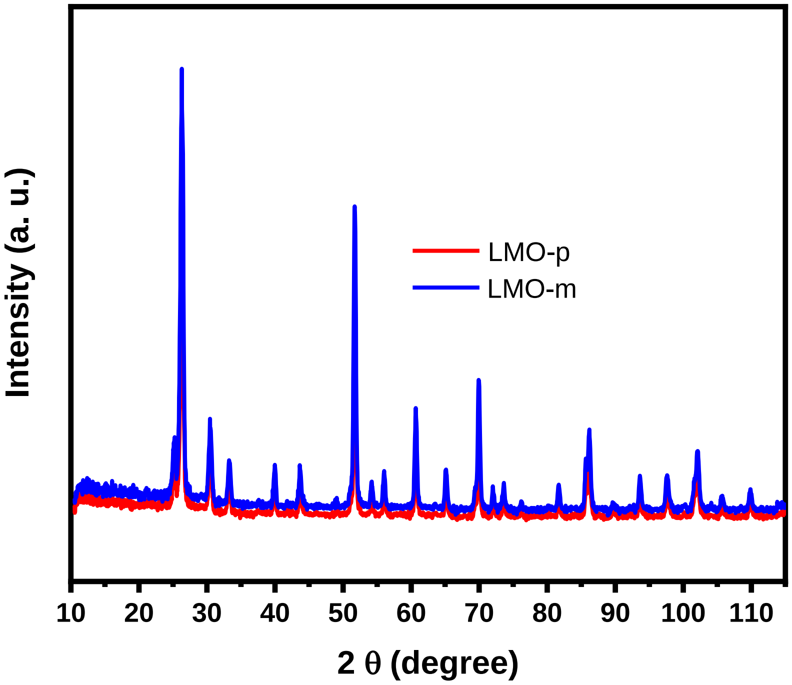

Figure 4.10: Rietveld fit of PND data for: LMO-p and LMO-m

4.2.7 X-ray Absorption Near Edge Structure (XANES)

Figure 4.11 shows the Mn K-edge XANES spectra of LMO-p and LMO-m. There is no significant edge shift in the two samples. The Mn edge: LCF (Table 4.4) fit shows LMO-p has Mn^{3+} (41.3%) and Mn^{4+} (58.6) while LMO-m has Mn^{3+} (41.1%) and Mn^{4+} (58.9%). Therefore, unlike the SXPS results which a shows significant increase in Mn^{4+} content in LMO-m than LMO: p, the XANES LCF fit shows that the LMO-m sample has a slight increase in the Mn^{4+} content than the LMO-p. It can be proposed that the effect of the microwave irradiation is more pronounced on the surfaces of the samples (as shown by SXPS) than in the bulk of the samples. This is because the SXPS is a surface analytical technique while XANES is of the bulk.

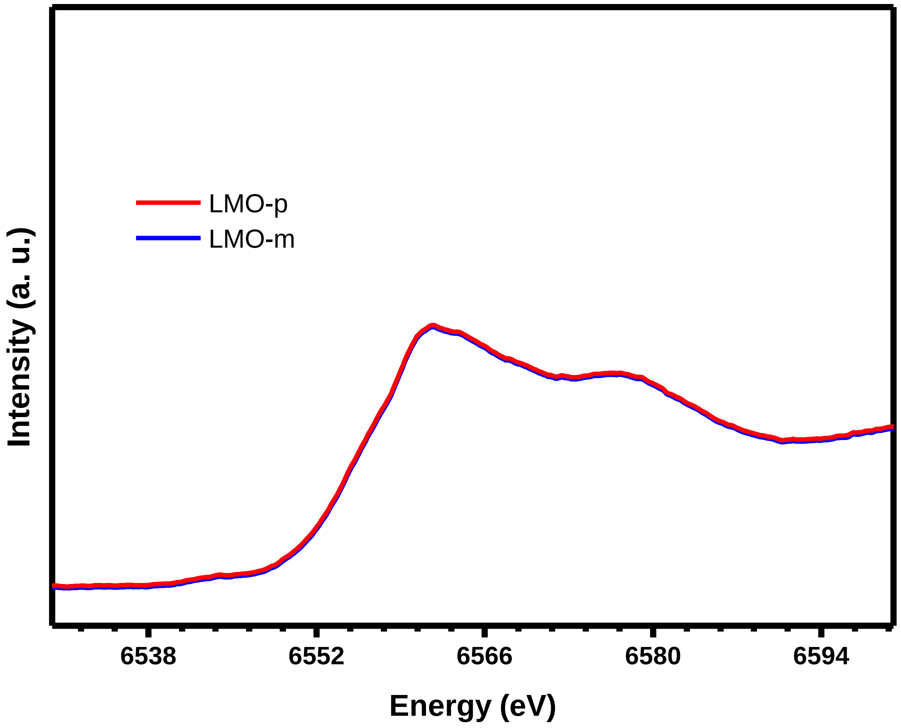

Figure 4.11: Mn K-edge XANES spectra of LMO-p and LMP: m

Table 4.4: XANES LCF fit

LMO	Pristine (%)	Microwave (%)
Mn^{3+}	41.4	41.1
Mn^{4+}	58.6	58.9

4.2.8 Raman Spectroscopy

Figure 4.12 shows the Raman spectra of LMO-p and LMO-m between 100 to 800 cm^{-1} stretch frequency. The LMO-p and LMO-m samples have strong bands at 627 and 626 cm^{-1} respectively. These peaks are the A_{1g} symmetry of stretching vibration of Mn and O compounds in the MnO_6 octahedra. The broad peaks relate to the bond lengths of the anions and cations in the LMO [32, 33]. The low-intensity shoulder peaks at 602 and 580 cm^{-1} (LMO-p and LMO-m respectively) are assigned to the F_{2g} mode and are linked to the average Mn valency (isotropic $[Mn^{4+}]O_6$ and J-T distorted $[Mn^{3+}]O_6$ octahedra) in spinel LMO structure. The medium intensity peaks at 483 (LMO-p) and 481 (LMO-m) are also assigned to the F_{2g} symmetry[32, 33]. The F_{2g} symmetry relates to the Li-O motion (movements of the tetrahedral cation) [32].

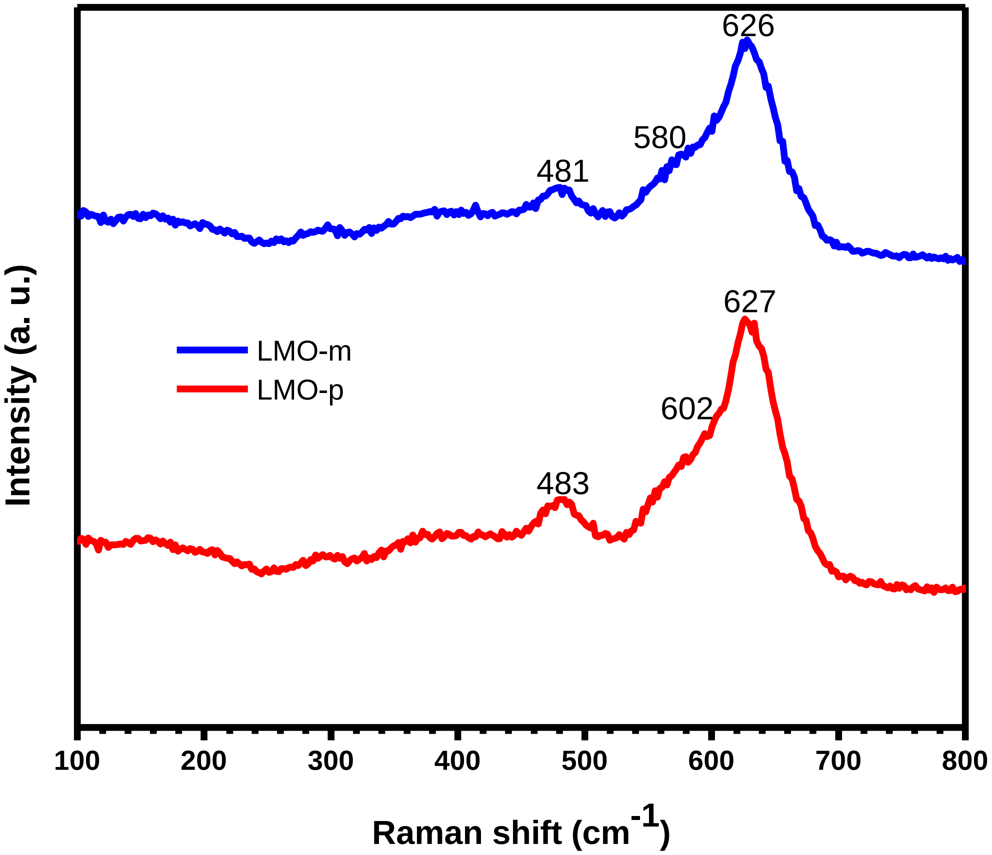

Figure 4.12: Raman analysis of LMO-p and LMO-m

4.2.9 Scanning Electron Microscopy (SEM) Characterization

The SEM was used to examine the images of the LMO-p and LMO-m. The morphology of the two samples looks alike. Figure 4.13 shows that the surfaces of the LMO-m sample are smoother than the LMO-p.

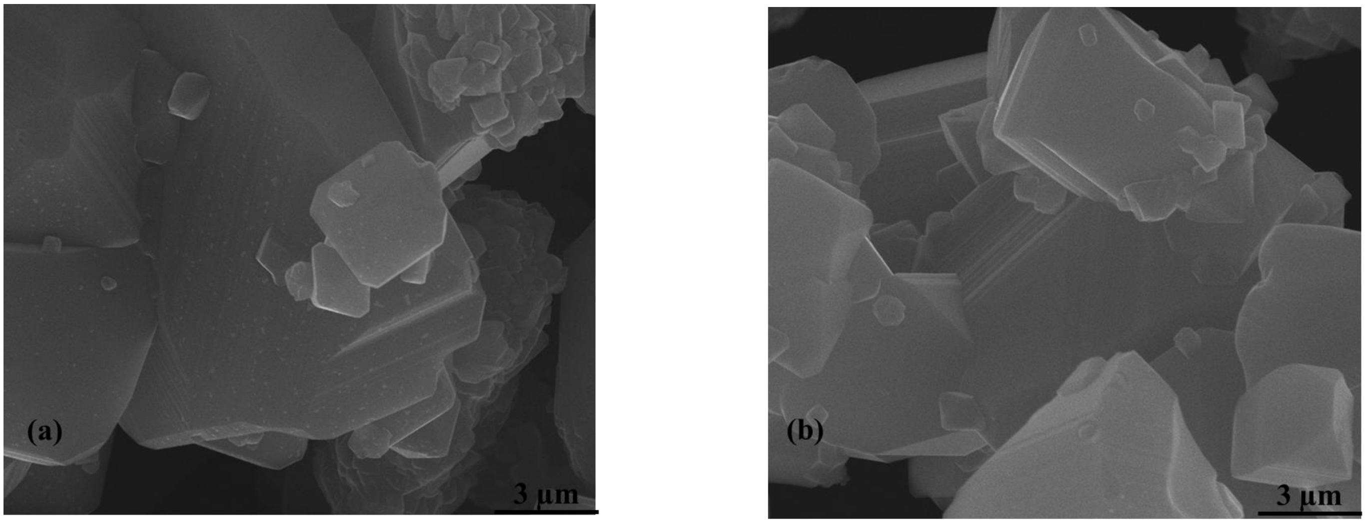

Figure 4.13: SEM images of (a) LMO-p and LMO-m

4.2.10 Electrochemical measurements

4.2.10.1 Cyclic voltammetry (CV)

Figure 4.14 to 4.17 compares the cyclic voltammograms (CV) of the LMO-p and LMO-m obtained at different cycles (1 – 10 cycles) in the voltage window (2 .0 and 4.4 V) versus Li/Li$^+$ (0.1mVs^{-1}, room temperature).

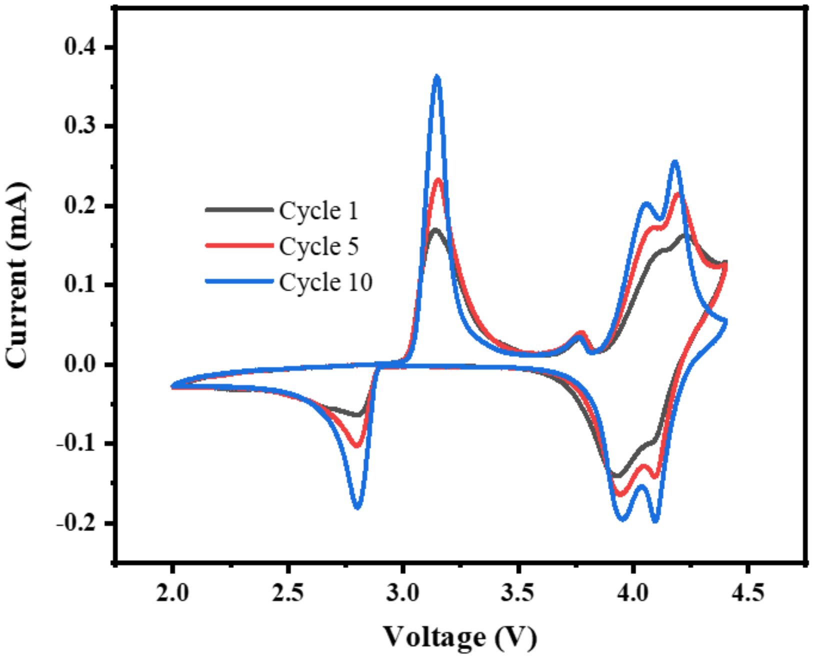

Figure 4.14: CV of LMO-p

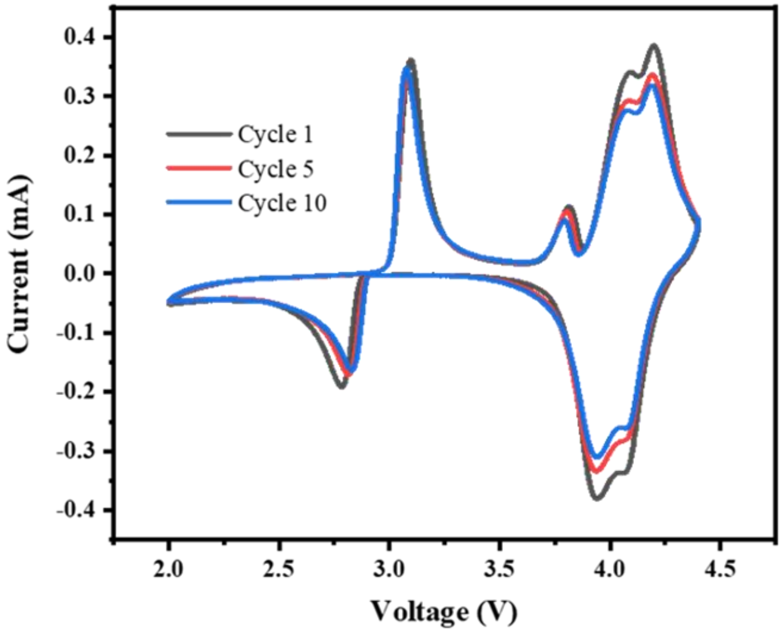

Figure 4.15: CV of LMO-m

The CV curves of the LMO-p and LMO-m (Figures 4.14 and 4.15) shows:

1. Redox peaks at around 2.8 and 3.1 V. It is believed that the redox process around 3.0 V relates to the phase-transition from cubic to tetragonal and thus reduce the average oxidation state of Mn to 3+ as shown in equation 4.1 [1]

   $$Li[Mn^{3+/4+}]_2O_4 + Li^+ + e^- \leftrightarrow Li_2[Mn^{3+}]_2O_4 \qquad (4.1)$$

   The phase transition (Jahn-Teller distortion) occurs when the Mn^{3+} content is > 50%. In other words, the cubic to tetragonal distortion is introduced into the LMO when the Mn oxidation state is below 3.5 as discussed in chapter 2. Figures 4.14 and 4.15 shows that the peak current around 2.8 V and 3.1 V of the LMO-p increases tremendously from 1 to 10, while those of the LMO-m did not increase (but reduced slight). Therefore, it can be suggested that the microwave irradiation has significantly reduced the Jahn-Teller distortion during cycling.
2. An irreversible anodic peak at around 3.8 V. Pfleging et al. [36] reported similar observation, but the cause of the peak has not been identified.

3. Oxidation-peaks around 4.1 /4.2 V and reduction-peaks around 4.0 and 4.1 V. These are characteristic peaks of redox processes of LMO cathode materials in the 4.0 V region.

To probe the redox properties of the two LMO electrode materials, the CV parameters obtained at the 1st and 10th cycles (Figure 4.16 and 4.17) are summarized in Table 4.5, focusing mostly on the following: (i) equilibrium voltage or open-circuit voltage (E^o / V), (ii) peak-to-peak separation voltage (ΔE_{pp} / V) representing the electron transfer kinetics of the cell; (iii) the heights of the anodic (I_{pa} / mA) and cathodic (I_{pc}/mA) peak current, which defines the mass transport and redox kinetics, and and (iv) the ratio of the the peak current (I_{pa}/I_{pc}), which gives insights into the reversibility of the redox chemistry or the Coulombic efficiency. The CV parameters provide four interesting insights into the redox properties of the two LMO materials. First, microwave treatment did not alter the equilibrium voltage (since both LMO materials give similar value of E^o at 4.1 V), thus the same Gibbs free energy is required. As will be shown in the galvanostatic charge-discharge (GC-D) section, both electrodes gave similar OCV of 4.1 V.

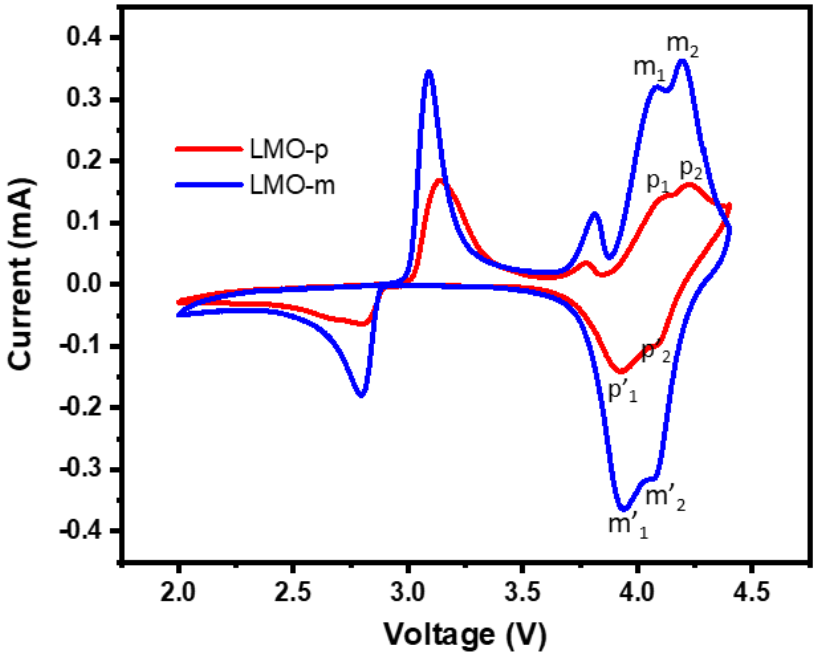

Figure 4.16: CV Cycle 1

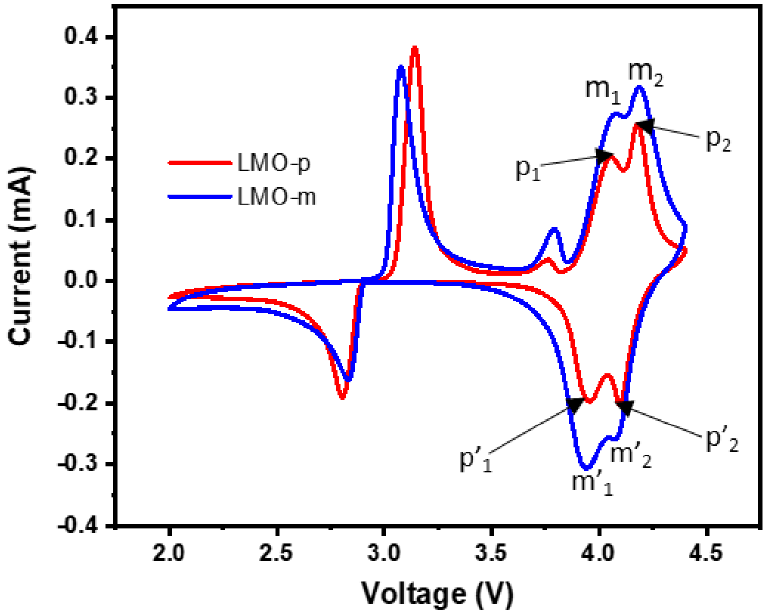

Figure 4.17: CV Cycle 10

Table 4.5: CV redox reaction parameters for LMO-p and LMO-m

LMO	**Cyclic voltammetric parameter**					
	Cycle #	E^o **/ V**	ΔE_{pp} **/ V**	I_{pa} **/mA**	I_{pc} **/mA**	I_{pa}/I_{pc}
LMO: p	*1st Cycle*	4.1	0.32	0.309	0.237	1.3
LMO: m		4.1	0.27	0.681	0.678	1.0
LMO: p	*10th Cycle*	4.1	0.18	0.462	0.402	1.2
LMO: m		4.1	0.23	0.589	0.562	1.0

Second, the first cycle shows that the LMO-m exhibits faster electron transfer properties (i.e., smaller value of ΔE_{pp} = 0.27 V) than the LMO-p counterpart (ΔE_{pp} = 0.32). Unlike the LMO-m that maintained its redox activities from the 1st to the 10th cycle, the LMO-p only became activated from the 2nd and subsequent cycles, essentially attaining the same level of electron transport (approx. ΔE_{pp} ~ 0.2).

Third, the LMO-m gave higher peak current from the 1st to the 10th cycle (both I_{pa} and I_{pc}) than the LMO-p counterpart. It is common knowledge that the current generated by an electrode is a function of two phenomena: (i) ***mass transport*** (which decribes the rate of which the electrolyte ions move across or within the electrode material), and (ii) ***charge-transfer kinetics*** (which defines ionic and/or electronic transfer at the electrode-electrolyte interface). Considering that both LMO-m and LMO-p show essentially similar ΔE_{pp} value, especially from the 2nd to the 10th cycle, it can be concluded that the high values of the peak currents recorded at the LMO-m is due to the dominance of its voltammetry by mass transport. The result clearly shows that microwave treatment confers on the LMO-m particles high surface area, pore volumes and pore size that allow for easy saturation of electrolyte and Li-ion transport (i.e., Li-ion de-intercalation / intercalation process). As would be seen from the (GC-D), the LMO-m gave higher specific capacity than the LMO-p counterpart. In addition, from the EIS, the resistance to charge transfer (Rct) is observed to be higher in LMO-p than in the LMO-m.

Fourth, the LMO-m maintained exceptional reversibility or Faradaic or Coulombic efficiency (i.e., attaining the theoretical value of $I_{pa}/I_{pc} = 1.0$) at all the cycles compared to the LMO-p cathode material that showed higher charging than discharging current (i.e., $I_{pa}/I_{pc} > 1.0$). The loss in Faradaic at the LMO-p may be associated with the electrons or ions involved in the electrochemical process involved in undesirable side reactions that may lead to the generation of heat or unwanted byproducts. As would be seen in the GCD plots (e.g., 50th cycle), the LMO-m shows better Coulombic efficiency than the LMO-p.

4.2.10.2 Electrochemical Impedance Spectroscopy (EIS)

The EIS was used to study the electrochemical performances of LMO-p and LMO-m cathode materials. Figure 4.18 and Figure 4.19 show the Nyquist plots of the two electrodes (LMO-p and LMO-m) at room temperature and the equivalent circuit used for the EIS fit respectively. R_s is the ohmic resistance of the electrode system, R_{CEI} is the high-frequency resistance at the cathode electrolyte interface which restrict the movement of Li^+. R_{ct} is the middle-frequency charge transfer resistance while the C_1 and C_2 are the interfacial capacitance of the electrode surface films and middle-frequency respectively. The M is low-frequency resistance which is ascribed to Li^+ diffusion in the electrode material. Table 4.6 shows that the Rs value for LMO-pristine (35.19 Ω) is close to that of LMO-m (38.35 Ω). The cause of the slight difference might have resulted from the fit error as the same concentration of electrolyte was used for the two cells. The R_{CEI} for the LMO-p (1077.0 Ω) is lesser than the LMO-m (1356.0 Ω). However, the R_{ct} for LMO-m electrode (177.6 Ω) is lesser than the LMO-p (352.4 Ω). Also, the low-frequency resistance (R_{d1}) associated with the restricted linear diffusion of Li^+ for LMO-m electrode (500.0 Ω) is lower than that of LMO-p (616.0 Ω) . The diffusion time constant t_{d1} for the LMO-p electrode (1.025 s) is lower than that LMO-m (1.507 s).

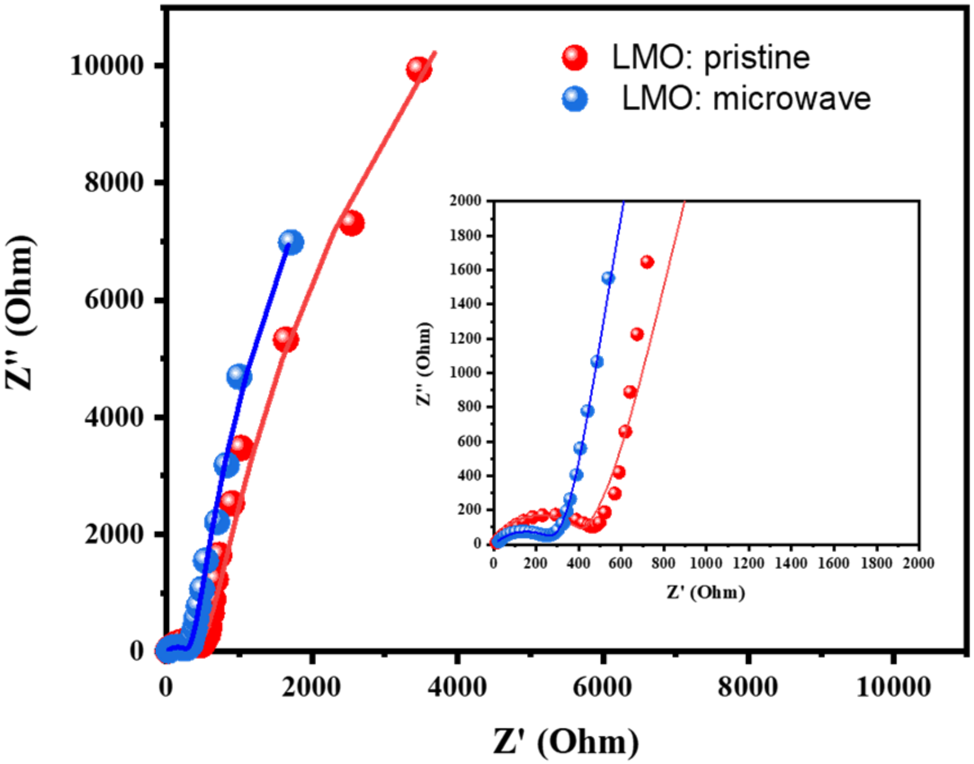

Figure 4.18: Nyquist plots at OCV Vs Li/Li$^+$ and room temperature (a) LMO-P and (b) LMO-m. Insert is the magnification of the Z" and Z' from 0 to 2000 Ω

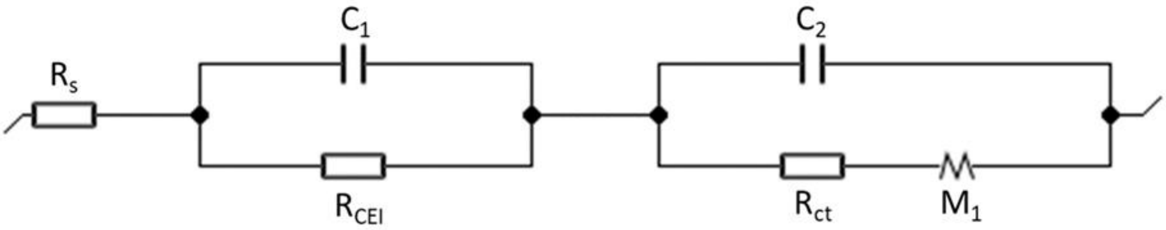

Figure 4.19: The equivalent circuit

Table 4. 6: EIS fitted parameters.

Electrode	R_s (Ω)	C (μF)	R_{CEI} (Ω)	C (μF))	R_{ct} (Ω)	R_{d1}	t_{d1} (s)
LMO-pristine	35.19	5.376	1077.0	5.747e^{-3}	352.4	616.0	1.025
	+/- 0.3511	+/- 0.1895	+/- 62.16	+/- 40.97e^{-6}	+/- 1.037	+/- 5.116	+/- 8.32e^{-3}
LMO-microwave	38.35	6.607	1356.0	3.098e^{-3}	177.6	500.0	1.507
	+/- 0.3915	+/- 0.1841	+/- 155.5	+/- 49.64e^{-6}	+/- 0.869	+/- 5.973	+/- 0.02965

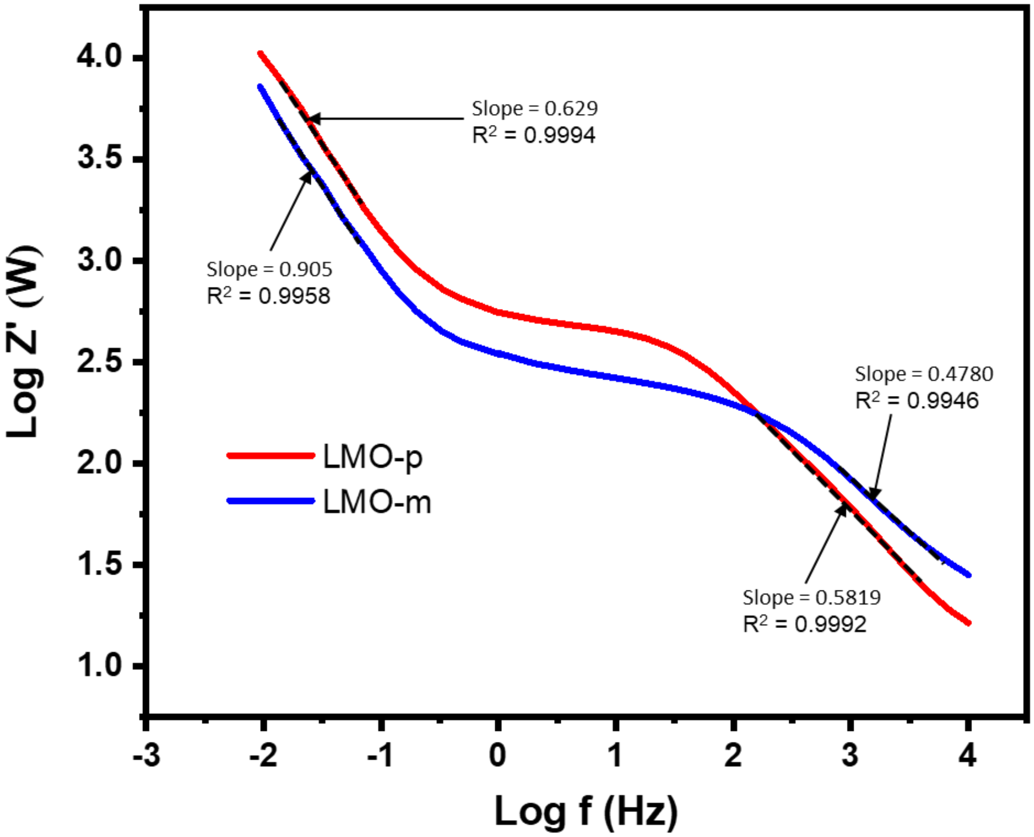

Figure 4.20: The Bode magnitude plot: magnitude

Figure 4.20 shows the Bode magnitude plots for LMO-p and LMO-m cathode materials. The Bode plots a give better understanding of the impedance than the Nyquist plots. The increasing slopes at the high frequency and low frequency represent the surface and kinetically control processes respectively. At the high-frequency range (surface process) between 10kHz and 100Hz the impedance of LMO-m electrode is higher than the LMO-p. This can result from the less conductive surface of LMO-m electrode material which was induced by its lower Mn^{3+} content. However, at the middle frequency (charge transfer process) between 100Hz and 0.1 Hz, the impedance of the LMO-m is lower than that of the LMO-p. The slopes of Bode magnitude plots for LMO-p and LMO-m are all lower than 1 with R^2 tending towards 1. This shows that the electrodes surfaces are not that of a smooth capacitance, but battery. Figure 4.21 shows the phase angle plots for the LMO-p and LMO-m. The LMO-p sample has a maximum phase angle of 11.2° at ›1 Hz while the LMO-m has its maximum phase angle of 11.3° at ~ 10 Hz. At the lower frequency of 0.01 Hz the phase angles of the two samples tend towards 90° and thus reflect a constant phase element (CPE < 90°) typical of insertion electrodes [35]. Figure 4.21 also show that the observed peak at lower frequency peak (0.01 Hz) for the LMO-p has a flat plateau (cycled) while LMO-m has a sloping profile (cycled). This suggests that LMO-p electrode has a semi-infinite type of solid phase diffusion while the LMO-m electrode has a transition frequency type behavior electrode [35]. At the middle frequency (10 – 100 kHz), the LMO-m has a phase angle shift to the higher frequencies. This shows that LMO-m has a faster kinetics of Li^+ than the LMO-p. Hence the LMO-m electrode material has a better conductivity than that of LMO-p. This result is consistent with the Bode magnitude plot, Nyquist plot G-CD and CV.

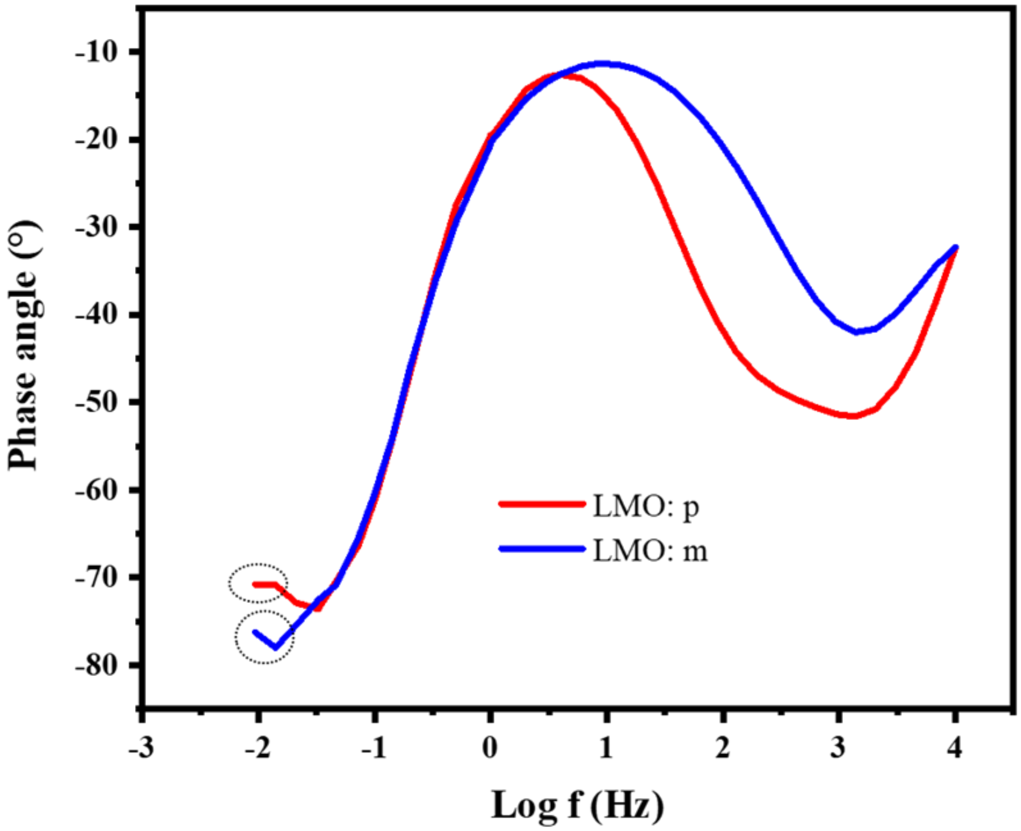

Figure 4.21: The Bode phase angle plot

4.2.10.3 Galvanostatic charge-discharge (G C-D)

Figures 4.2 (a and b) exhibits the charge-discharge curves of LMO-p and LMO-m electrodes respectively, between 3.5 and 4.38 V (0.1 C). The LMO: m electrode delivered a relatively higher discharge capacity of 96.1 mAhg^{-1} than LMO-p (77.0 mAhg^{-1}). The LMO-m has a higher specific capacity because of its larger surface area which provides a higher contact area with the electrolyte and results in high Li^{+} flux across the interface. The LMO-m larger pores of the LMO-m provide more channels for the electrolyte and increase the contact surface area between the particles and electrolyte for better lithium insertion/extraction [19]. Figures 4.23 and 4.24 show the capacity discharged and coulombic efficiency vs cycle number for LMO-p and LMO-m respectively. The LMO-m curves show that it has better coulombic efficiency than the LMO-p.

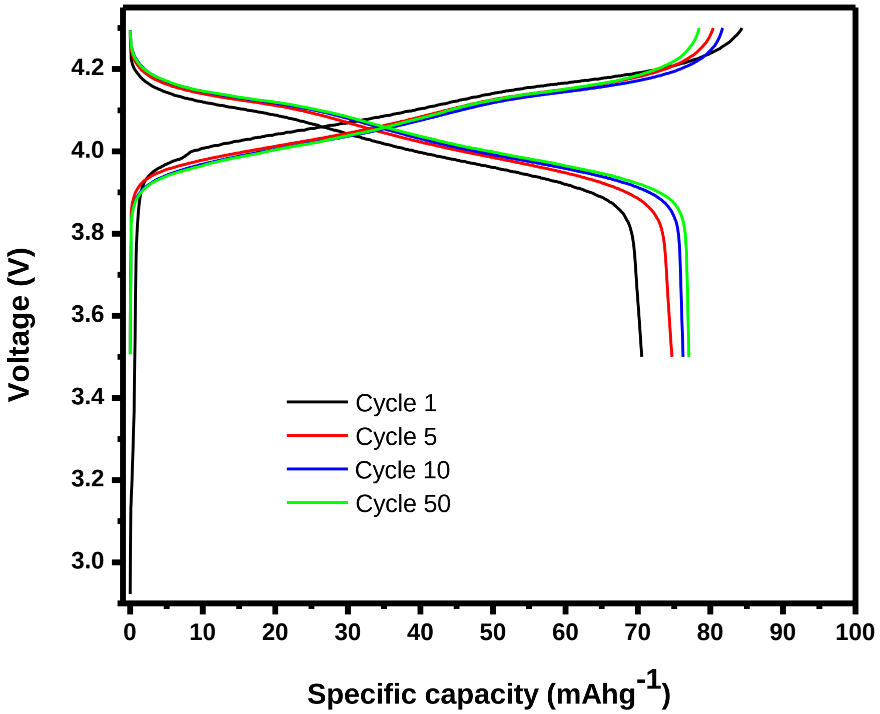

Figure 4.22 a: Charge-discharge between 3.5 - 4.3 V at 0.1 C for LMO-p

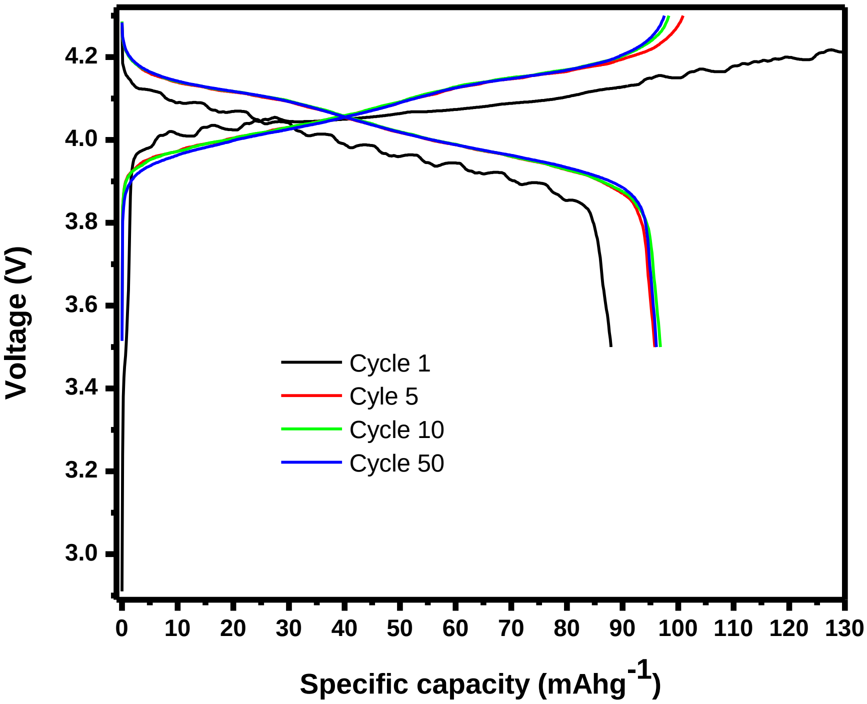

Figure 4.22 b: Charge-discharge between 3.5 - 4.3 V at 0.1 C for LMO-m

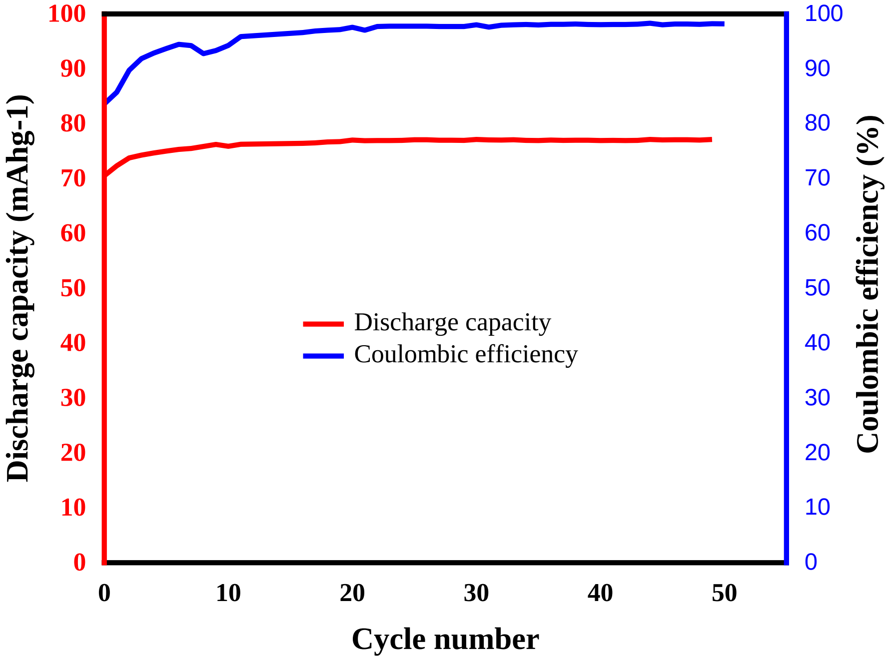

Figure 4.23: Discharge-capacity and coulombic efficiency vs cycle number for LMO-p

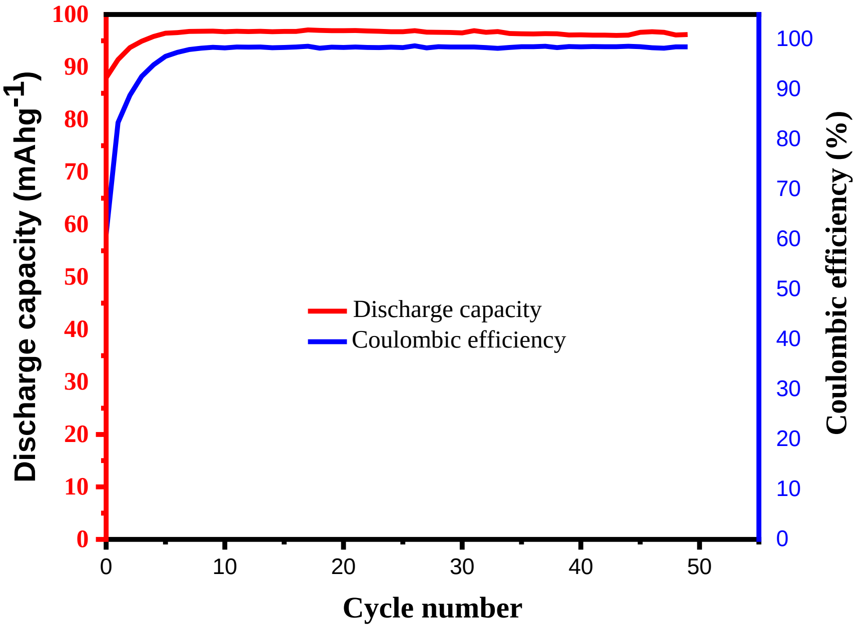

Figure 4.24: Discharge capacity / coulombic efficiency Vs cycle number for LMO-m

4.2.10.4 Rate capability

Figure 4.25 shows the rate capability of the LMO-p and LMO-m samples. The cells were charged and discharged at 0.1C, 0.5C, 1C, 2C, 5 C, 10 and again at 0.1 C. The LMO-m sample shows higher specific capacities than LMO-p at these C rates. Hence the microwave irradiation has enhanced the rate capacity due to larger surface area, pore size and pore volume of LMO-m.

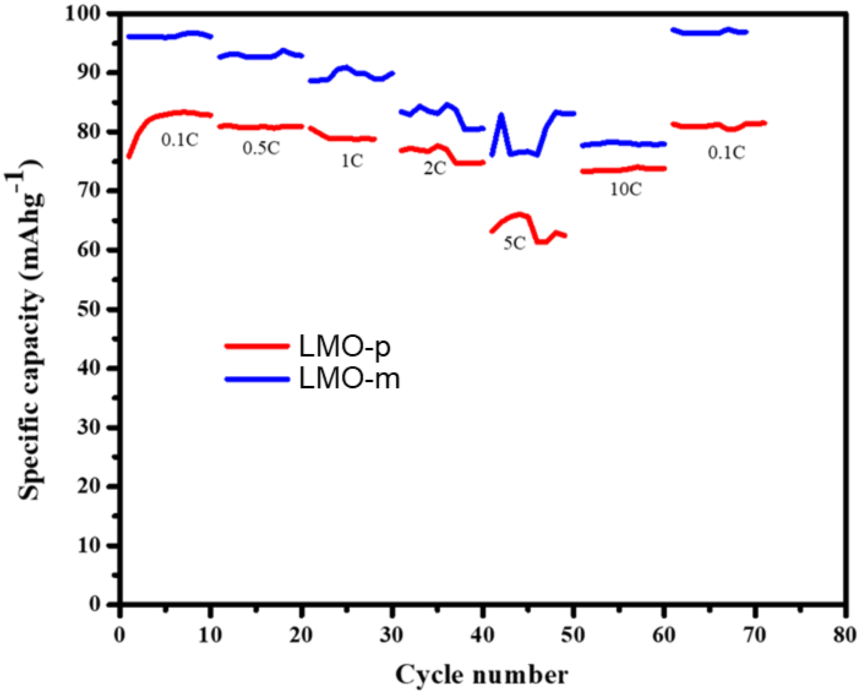

.**Figure 4.25:** Rate capability of LMO-p and LMO-m samples

4.3 Conclusions

In this study, the unique approach of microwave irradiation has been used to suppress the Jahn-Teller distortion and immensely enhanced the electrochemical properties of the LMO for L-IB. The enhancement of the electrochemical properties of the LMO was achieved by improving the intrinsic parameters: the ratio r = Mn^{4+}/Mn^{3+}, oxidation state of Mn, lattice parameter, distribution of Li and Mn cations on the tetrahedral and octahedral sites rather than extrinsic parameters such as the morphology and size of the spinel particles. For the first time microwave irradiation is used to induce lithium-ion motion in the $LiMn_2O_4$ structural systems as proven by NMR diffractions without doping or coating with foreign ions. Thus, the microwaved sample - LMO-m has reduced Jahn-Teller active Mn^{3+} content (from 58% to 43%), increase the average oxidation state of Mn (from 3.42

to 3.57) and specific capacity (from 76.6 to 96.1 $mAhg^{-1}$). Furthermore, the surface and bulk analysis by the SXPS and XANES: Mn edge: LCF fit respectively have confirmed that microwave irradiation caused the LMO-m surface to have a lower Mn^{3+} content than LMO-p while the bulk of the two samples have approximately the same Mn^{3+} content. The CV also confirms that microwave suppresses the Jahn Teller distortion. Therefore, it can be proposed that the strategic use of the microwave irradiation process can be used to improve the physical and electrochemical properties of LMO without doping and coating. This unique synthesis route can be scale-up for practical application to the synthesis of LMO for LI-Bs.

4.4 References

1. C. Masquelier, M. Tabuchi, K. Ado, R. Kanno, Y. Kobayashi, Y. Maki, O. Nakamura, and J. B. Goodenough, Journal of solid state chemistry 123, 255–266 (1996) Article No. 0176
2. H. Berg, John O. Thomas, Wen Liu, Gregory C. Farrington Solid State Ionics 112 (1998) 165–168
3. K. S. Reddy, B. Gangaja, S. V. Nair, D. Santhanagopalan, Electrochimica Acta 250 (2017) 359–367
4. D. Capsoni, M. Bini, G. Chiodelli, P. Mustarelli, V. Massarotti, C. B. Azzoni, M. C. Mozzati, Laura Linati, J. Phys. Chem. B 2002, 106, 7432-7438
5. A. Iturrondobeitia, A. Goñi, V. Palomares, I. Gil de Muro, L. Lezama, T. Rojo, Journal of Power Sources 216 (2012) 482-488
6. Y. J. Lee, F. Wang, C. P. Grey, J. Am. Chem. Soc. 1998, 120, 12601-12613
7. H. Berg, E. M. Kelder, J. O. Thomas, J. Mater. Chem., 1999, 9, 427–429
8. H. Xia, Z. Luo, J. Xie, Progress in Natural Science: Materials International 2012;22(6):572–584
9. Y. Chen, Y. Tian, Y. Qiu, Z. Liu, H He, B. Li, H. Cao, Materials Today Advances 1 (2019) 100001
10. J. Lu, C. Zhan, T. Wu, J. Wen, Y. Lei, A. J. Kropf, H. Wu, D. J. Miller, J. W. Elam, Y. Sun, X. Qiu, K. Amine, Nature Communications | 5:5693 | DOI: 10.1038/ncomms6693

11. D. Capsoni, M. Bini, G. Chiodelli, V. Massarotti, C. B. Azzoni, M. C. Mozzati, A. Comin Phys. Chem. Chem. Phys., 2001, 3, 2162-2166
12. Y. J. Lee, S. Park, C. Eng, J. B. Parise, C. P. Grey, Chem. Mater. 2002, 14, 194-205
13. R.J. Gummow, A. de Kock, M.M. Thackeray, Solid State Ionics 69 (994) 59-67
14. Y. Cai, Y. Huang, X. Wang, D. Jia, W. Pang, Z. Guo, Y. Du, X. Tang, Journal of Power Sources 278 (2015) 574-581
15. S. Martinez, I. Sobrados, D. Tonti, J. M. Amarilla and J. Sanz Phys.Chem.Chem.Phys., 2014, 16, 3282
16. H. Ming, Y. Yan, J. Ming, J. Adkins, X. Li, Q. Zhou, J. Zheng, Electrochimica Acta 120 (2014) 390–397
17. M. Molenda, M. Bakierska, D. Majda, M. Świętosławski, R. Dziembaj, Solid State Ionics 272 (2015) 127–132],
18. Y,Yu, J. Guo, M. Xiang, C. Su, X. Liu, H. Bai, W. Bai, K Duan, Scientific Reports | (2019) 9:16864 |
19. S. Li, K. Zhu, J. Liu, D. Zhao, X. Cui, Journal of Electrochemical Energy Conversion and Storage, February 2019, Vol. 16 / 011006-1
20. P. R. Ilango, K. Prasanna, S. J. Do, Y. N. Jo, C. W. Lee, Scientific Reports | 6:29826 | DOI: 10.1038/srep29826]
21. R. S. Liu, L. Y. Jang, J. M. Chen, Y. C. Tsai, Y. D. Hwang, R. G. Liu, Journal of Solid State Chemistry 128, 326*Đ*329 (1997)
22. C. P. Grey, Y. J. Lee, Solid State Sciences 5 (2003) 883–894
23. C. P. Grey, S. G. Greenbaum, MRS BULLETIN/AUGUST 2002

24. Y. J. Lee, F. Wang, C. P. Grey J. Am. Chem. Soc. 1998, 120, 12601-12613
25. M. C. Tucker, J. A. Reimer, E. J. Cairns Journal of The Electrochemical Society, 148 (8) A951-A959 (2001)
26. K. R. Morgan, S Collier, G. Burns K. Ooi. J. CHEM. SOC., CHEM. COMMUN., 1994
27. J. Lee, C. Eng, C. P. Grey. Journal of The Electrochemical Society, **148 (**3) A249-A257 (2001)
28. C. P. Grey and N. Dupre, Chem. Rev. 2004, 104, 4493-45129.
29. M. C. Tucker, J. A. Reimer, E. J. Cairns, Electrochemical and Solid-State Letters, 3 (10) 463-466 (2000)
30. B. Gee, C. R. Horne, E J. Cairns, J. A. Reimer, J. Phys. Chem. B 1998**,** 102, 10142-10149
31. K. Raju, F. P. Nkosi, E. Viswanathan, M. K. Mathe, K. Damodaran, K.I. Ozoemena Phys.Chem. Chem. Phys., 2016, 18, 13074—13083
32. C. V. Ramana, M. Massot and C. M. Julien Surf. Interface Anal. 2005; 37: 412–416
33. J. Proell, R. Kohler, A. Mangang, S. Ulrich, C. Ziebert, W. Pfleging Journal of Laser Micro/Nanoengineering Vol. 7, No. 1, 2012
34. F. Lai, X. Zhang, Q. Wu, J. Zhang, Q. Li, Y. Huang, Z. Liao, H. Wang ACS Sustainable Chem. Eng. 2018, 6, 570−578.
35. G. Sikha, R. E. White, Journal of The Electrochemical Society, 155 (12) (2008) A893-A902

36. J. Proell, R. Kohler, A. MANGANG, S. Ulrich, C. Zielbert, W. Pfleging, Journal of Laser Micro/Nanoengineering Vol. 7, No. 1, 2012

CHAPTER 5

Defect-engineering of β-$MnO_{2-\delta}$ precursor controls structure-property relationships in high-voltage spinel $LiMn_{1.5}Ni_{0.5}O_4$ cathode materials for lithium-ion battery

---

5.1 Introduction

The need to meet the high- energy density Li-ion batteries (L-IBs) for electric vehicle (EV) and stationary storage applications has advanced the spinel $LiMn_{1.5}Ni_{0.5}O_4$ (LMNO) cathode materials as an attractive potential candidate for next-generation L-IBs [1]. The LMNO cathode materials have a relatively higher working voltage and energy density than several commercialized materials (Table 5.1). The spinel LMNO cathode material's higher voltage (~ 4.7 V) originated from the increase in the required energy to remove the Ni 3d e_g electrons which have binding energy (~ 2.1 eV) relative to that of Mn 3d e_g (1.6 eV) [2, 3] . In some applications such as the EV where high voltage is required for state of start-up, accelerate and climb up, the spinel LMNO cathode materials have advantage over other cathode materials. This is because the spinel LMNO has a distinguishing high operational voltage which will require relatively less numbers of batteries in series connection. Fewer numbers of batteries have the ease of control [2] and occupies less space, thus more compact and safer.

Table 5.1: LMNO Vs commercialized cathode materials [2]

Cathode material	Average voltage (V)	Gravimetric capacity (mAhg^{-1})	Gravimetric energy (Whkg^{-1})
$LiCoO_2$	3.7	140	518
$LiFePO_4$	3.3	150	495
$LiNi_{1/3}Mn_{1/3}Co_{1/3}O_2$	3.6	160	576
$LiMn_2O_4$	4.0	110	440
$LiMn_{1.5}Ni_{0.5}O_4$	**4.7**	**146**	**686**

Previous studies have reported that spinel LMNO has two probable crystal structures in Fd3m and $P4_323$ symmetries [4, 5] . The Fd3m symmetry has a Face Centered Cubic (FCC) structure with the Li positioned in the 8a Wyckoff site, while the Mn and Ni are randomly arranged in the 16d Wyckoff sites. Thus, the Fd3m symmetry is termed disordered structure. The $P4_323$ symmetry has a primitive simple cubic structure with the Li in the *8c* Wyckoff position while the Mn and Ni are regularly arranged in the *12d* sites and *4a* Wyckoff position respectively. Hence, $P4_323$ symmetry is known as an ordered structure. The disordered structure is reported to be synthesized at temperatures above 700 °C while the ordered structure is synthesized at ~ 700 °C [6]. A lot of research works have been carried out on the spinel LMNO [7], but its structural relationship with the electrochemical properties is still a challenge [8, 9]. The properties (electrochemical) of LMNO are related to the degree of disorder, doping, impurities, morphology, oxygen vacancy, Mn^{3+} content among others.

Oxygen vacancy is identified as a key structural factor because it correlation with the degree of disorder and Mn^{3+} content. An oxygen vacancy is formed when an oxygen atom on its typical site is transformed to the gaseous state. An oxygen vacancy occurs in spinel LMNO when the synthesis temperature rises above 700 ºC [8] as shown in the equation 5.1 below [10]:

$$LiMn_{1.5}Ni_{0.5}O_4 \longleftrightarrow Li_zNi_{1-z}O + rLiMn_{1.5+w}Ni_{0.5-w}O_{4-\delta} + sO_2 \qquad (5.1)$$

The equation 5.1 shows that $LiMn_{1.5}Ni_{0.5}O_4$ released some oxygen at temperature above 700ºC and the rock salt ($Li_xNi_{1-x}O$) impurity and oxygen vacant spinel LMNO ($LiMn_{1.5+w}Ni_{0.5-w}O_{4-\delta}$) are formed. To maintain charge balance in the spinel $LiMn_{1.5-y}Ni_{0.5-y}O_{4-\delta}$, the Mn oxidation state is reduced to +3 [11]. Furthermore, in the course of the reaction, the ordered Mn/Ni phase in $LiMn_{1.5}Ni_{0.5}O_4$ changes to a disordered Mn/Ni phase [7]. Thus, it can be concluded that the high temperature creates the oxygen vacancy which in turn caused the presence of Mn^{3+}, disordered phase and impurity in the spinel LMNO. The presence of Mn^{3+} in $LiMn_{1.5-y}Ni_{0.5-y}O_{4-\delta}$ has been reported to improve the conductivity and increases the lattice constant for enhanced Li^+ transport than the Mn^{4+} in $LiMn_{1.5}Ni_{0.5}O_4$ [7, 12]. The disordered phase has been known to enhance the phase transformation behavior by extending the solid-solution reaction for Li extraction [13], 14]. However, the presence of the $Mn3^+$ has the drawback of the disproportionation reaction, which causes the dissolution of the Mn^{2+} into the electrolyte. The dissolved Mn^{2+} obstructs the diffusion of Li^+ during cycling and subsequently leads to the capacity fading of the cell

[15]. Also, during cycling the impurity phase in the disordered LMNO blocks the Li^+ mobility and thus lower the cell capacity [5].

Huang's group [16] carried out a research work on the relationship between the oxygen vacancy and Mn/Ni arrangements in spinel LMNO using the density- functional theory (D-FT) based first-principle calculation. The group's computational and experimental studies showed that the Mn/Ni arrangements are closely related to oxygen vacancies. Also, Whitt ingham et al. [9] DFT calculations and experimental works to establish that the oxygen vacancy in spinel LMNO changes directly with the degree of disordered phase and Mn^{3+} content. It is commonly reported that at temperature above 700ºC, oxygen vacancies, Mn^{3+} and impurity are introduced into the spinel LMNO lattice [5]. In addition, oxygen vacancies and Mn^{3+} have effects on the Mn / Ni ordering in the LMNO. Li et al. [5] stated that since the oxygen vacancies that brought about the generation of Mn^{3+} and impurity phase also induced Mn/Ni disordering, therefore these parameters are closely related. Li et al. [5] cited the argument on the formation of oxygen vacancy in the spinel LMNO not having direct relationship based on previous report that the doping of some transition metals into the spinel LMNO lattice can generate Mn^{3+} without the formation of oxygen vacancies. However, Whittingham et al. [9] emphasized that even though the presence of Mn^{3+} in the Cr-doped LMNO ($LiMn_{1.5}Ni_{0.45}Cr_{0.05}O_{4-\delta}$) is caused by the doped Cr, the oxygen vacancy also has its contributing effect to the Mn^{3+} content. Consequently, it is expedient to study the relationship between these parameters and their effects on the electrochemical performance on the LIBs.

In this research, the relationship among the structural parameters: oxygen vacancy, disordered phase, Mn^{3+} and impurity contents is studied using the as prepared spinel $LiMn_{1.5}Ni_{0.5}O_{4-\delta}$ having different degrees of oxygen vacancies (δ). For the first time the precursors: β-$MnO_{2-\delta}$ nanorods ($MnO_{2-\delta}$-Ar and $MnO_{2-\delta}$-H_2) were produced by the simple molten-salt process under different levels of reducing atmospheres. Also for the first-time the precursors: $MnO_{2-\delta}$-Ar and $MnO_{2-\delta}$-H_2 nanorods are used to synthesize oxygen vacant spinel LMNO-Ar and LMNO-H_2 cathode materials at 700 °C without doping, higher temperatures (above 700 °C), use of organic compound and post-annealing or modification of the cooling profile. The effects of oxygen vacancies on the electrochemical performance of the oxygen vacant electrodes were examined. The results of the studies showed that the oxygen vacancies change concurrently with the degree of disorder and Mn^{3+}, but not with the impurities as commonly reported [5, 10]. Therefore, the strategic control of the oxygen vacancy in spinel LMNO by MnO_2 with different oxygen vacancies using this synthetic route is thus proposed.

5.2 Results and Discussions

5.2.1 The precursor: MnO_2 (Physical Characterization)

5.2.1.1 Powder *X*-ray Diffraction (PXRD)

The experimental PXRD spectrum in Figure 5.1 to examine the structure of the synthesized precursor: MnO_2. Figure 5.1 shows that the PXRD pattern has strong peaks (110), (101) and (211) positioned at 2θ = 28.7°, 37.4°, and 56.8° respectively with weak peaks (impurities: MnOOH and Mn_3O_4 peaks). Dahn et al [17] reported strong peak positions at 2 θ = 28°, 37° and 57°for β-MnO_2. Previous report by Chen et al [18] stated that the impurities peaks can be found in the diffraction pattern of oxides heated in the reduced atmosphere of Ar/H_2 and not only can oxygen vacancy can be introduced into manganese oxides by simple heat treatment, but can be used to tune the concentration of the oxygen defects.

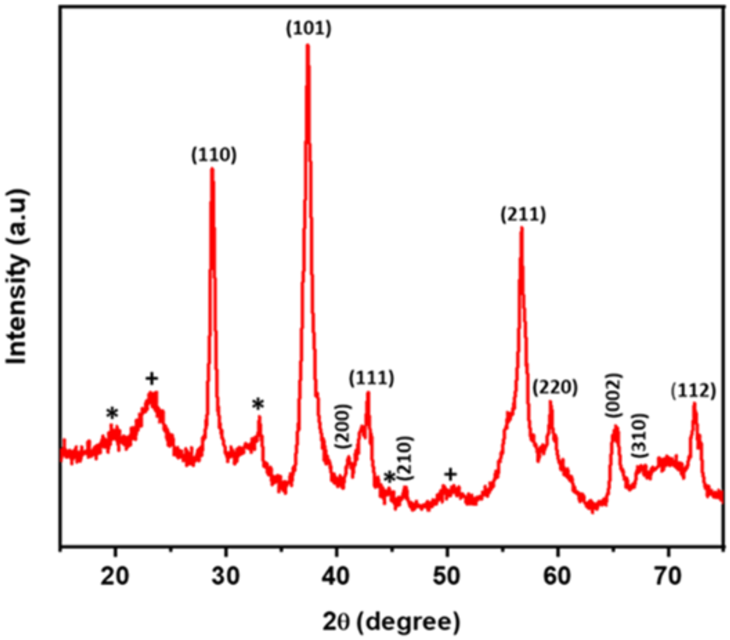

Figure 5.1: PXRD patterns of β-$MnO_{2-\delta}$

5.2.1.2 Raman Spectrum (RS)

Figure 5.2 shows the Raman spectrum (RS) of the β-MnO_2. The β-$MnO_{2-\delta}$ has strong diffraction peak (637 cm^{-1}) which can be allotted to the stretching Mn-O bond vibrations in MnO_6 octahedra for β-MnO_2 [19]. Sodo et al [19] cited a previous study that reported positions of strong bands between 630 and 655 cm^{-1} as a function of the concentration of oxygen vacancy defects. Therefore, we proposed that we have successfully synthesized β-$MnO_{2-\delta}$ by the simple molten salt synthetic method.

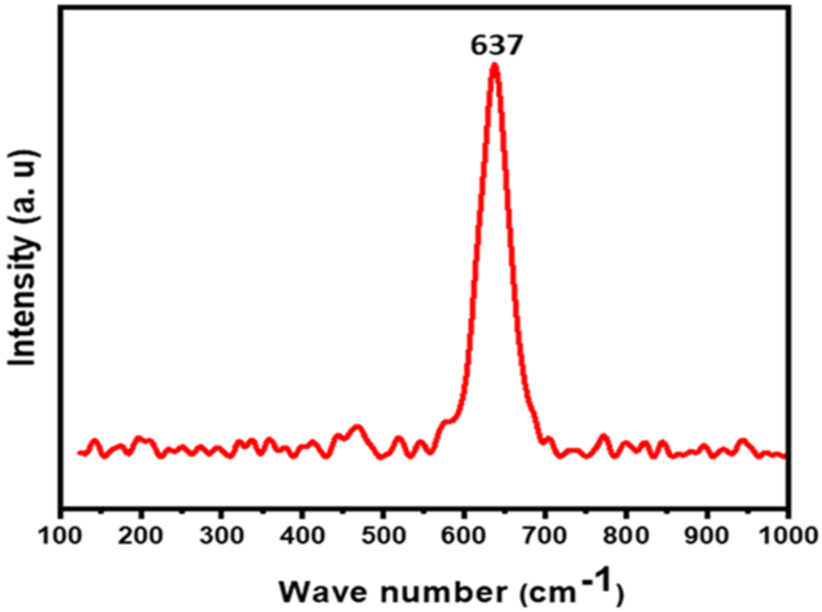

Figure 5.2 Raman spectra of β-$MnO_{2-\delta}$

5.2.1.3 Transmission Electron Microscopy (TEM)

Figures *5.3* (*a* and *b*) show the TEM images for β-$MnO_{2-\delta}$-Ar and (b) β-$MnO_{2-\delta}$-H_2 at 200nm respectively. The two samples have similar rod-like shape.

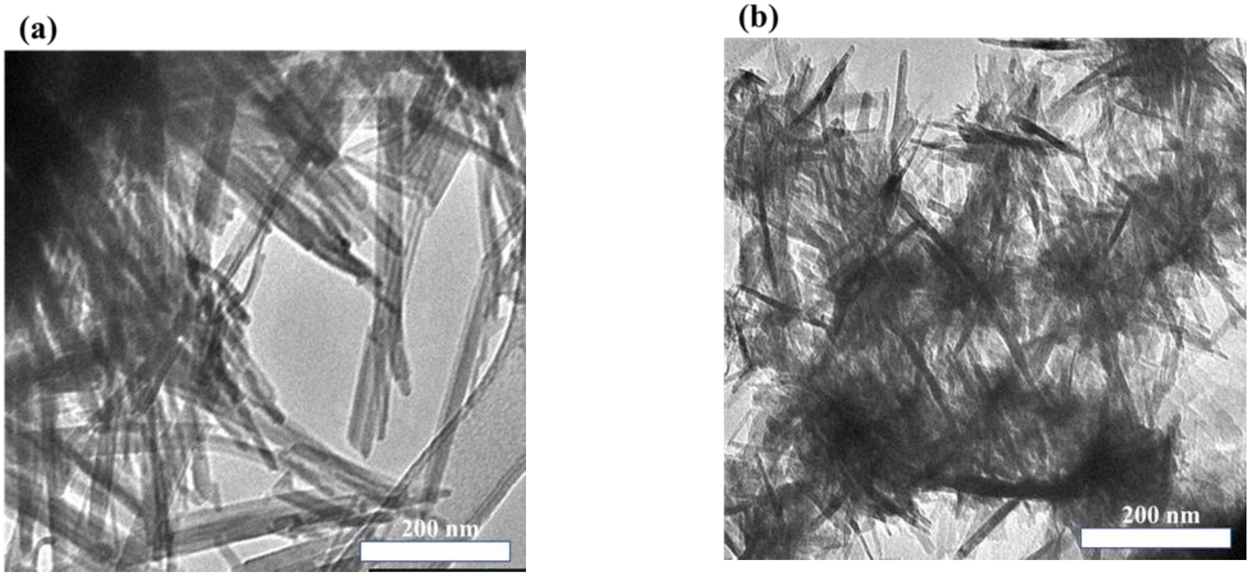

Figure 5.3: TEM-image - (a) β-$MnO_{2-\delta}$-Ar and (b) β-$MnO_{2-\delta}$-H_2

5.2.2 The product: LMNO

5.2.2.1 The Density-Functional Theory (D-FT) calculations

The D-FT calculations are used for the investigation of the effects of oxygen vacancy on LMNO cathode material's conductivity. Figures 5.4 (a to c) and Table 5.1 show the D-FT calculations results for the perfect LMNO ($LiMn_{1.5}Ni_{0.5}O_4$), LMNO with only one oxygen vacancy ($LiMn_{1.5}Ni_{0.5}O_{4-\delta}$) and LMNO with two oxygen vacancy LMNO ($LiMn_{1.5}Ni_{0.5}O_{4-2\delta}$). The D-FT results reveal that the D-FT energy gap reduces as the oxygen vacancy increases. It is common knowledge that conductivity increases with decrease in energy band gap. Hence, the conductivity of LMNO increases with increase oxygen vacancy. It is thus expected that the LMNO-H_2 will be more conductive than LMNO-Ar as will be observed in the galvanostatic charge-discharge measurements.

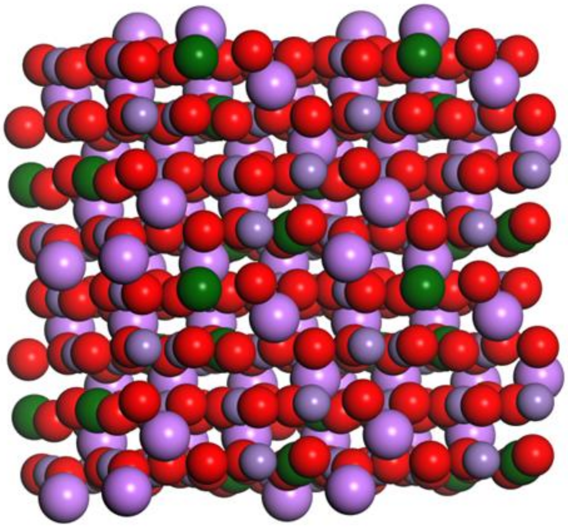

Figure 5.4 (a): Perfect LMNO without oxygen vacancy ($LiMn_{1.5}Ni_{0.5}O_{4-\delta}$) (448 atom Supercell)

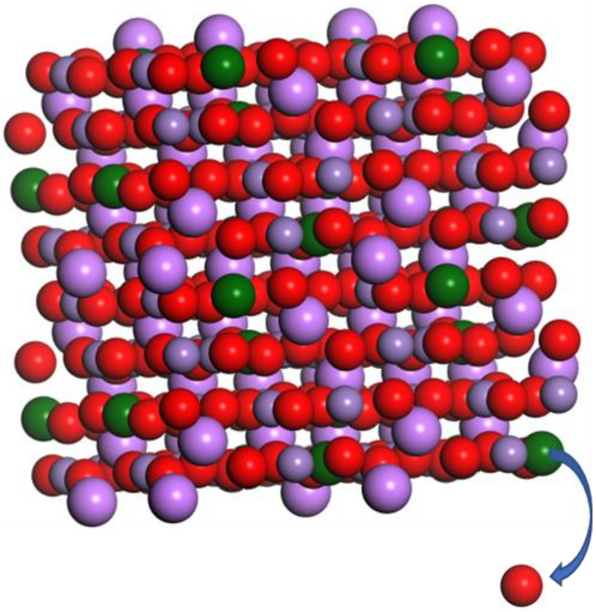

Figure 5.4 (b): LMNO with only one oxygen vacancy ($LiMn_{1.5}Ni_{0.5}O_{4-\delta}$) (447 atom Supercell)

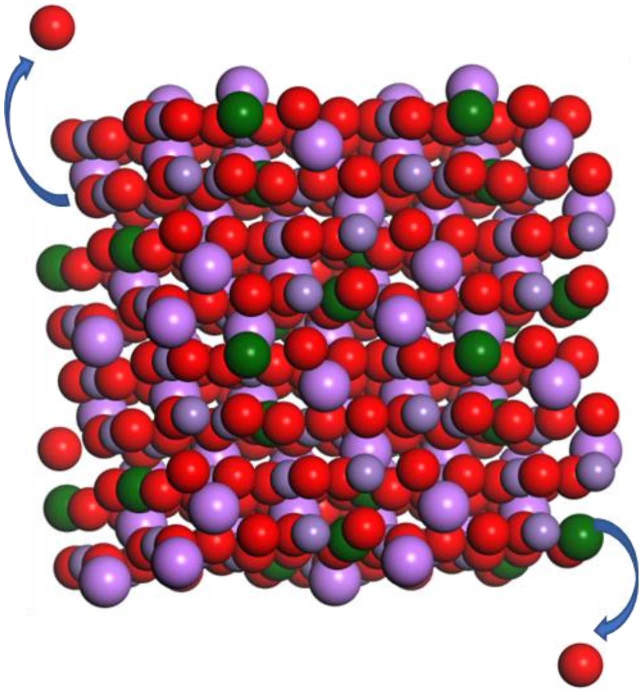

Figure 5.4 (c): LMNO with two oxygen vacancy ($LiMn_{1.5}Ni_{0.5}O_{4-2\delta}$) (446 atom Supercell)

Table 5.2: Summary of DFT calculations

	$LMNO_4$	$LMNO_{4-\delta}$	$LMNO_{4-2\delta}$
DFT energy gap (eV)	4.604 eV	4.597 eV	4.547 eV
Valence band edge (eV)	-15.841 eV	-15.852 eV	-15.821 eV
Conduction band edge (eV)	-11.237 eV	-11.255 eV	-11.274 eV
Fermi Energy (eV)	12.782 eV	-12.804 eV	-12.826 eV

5.2.2.2 Thermogravimetric Analysis (TGA)

Figure 5.5 shows TGA profiles for the LMNO-Ar and LMNO-H_2 samples. The LMNO-H_2 samples lost about 1.5% of its weight before 300 ^oC, while LMNO-Ar lost about 0.4%. The loss in weight may be caused by the evaporation of absorbed H_2O [20]. The inserted

F-TIR spectra show vibrational band 1100 cm^{-1} (approx..) which can be allotted to the (O-H) vibration in crystal lattice [21]. This (O-H) vibration may suggest the cause of the weight loss in LMNO-H_2. The absorption peak of the LMNO-H_2 sample is sharper (stronger) than that of LMNO-Ar which might have resulted from the higher concentration of hydrogen in the synthesis atmosphere of LMNO H_2 precursor [21. Xiao et al cited Kunduraci's study that revealed the weight loss by LMNO after 700 °C, is mainly due to oxygen loss [22].

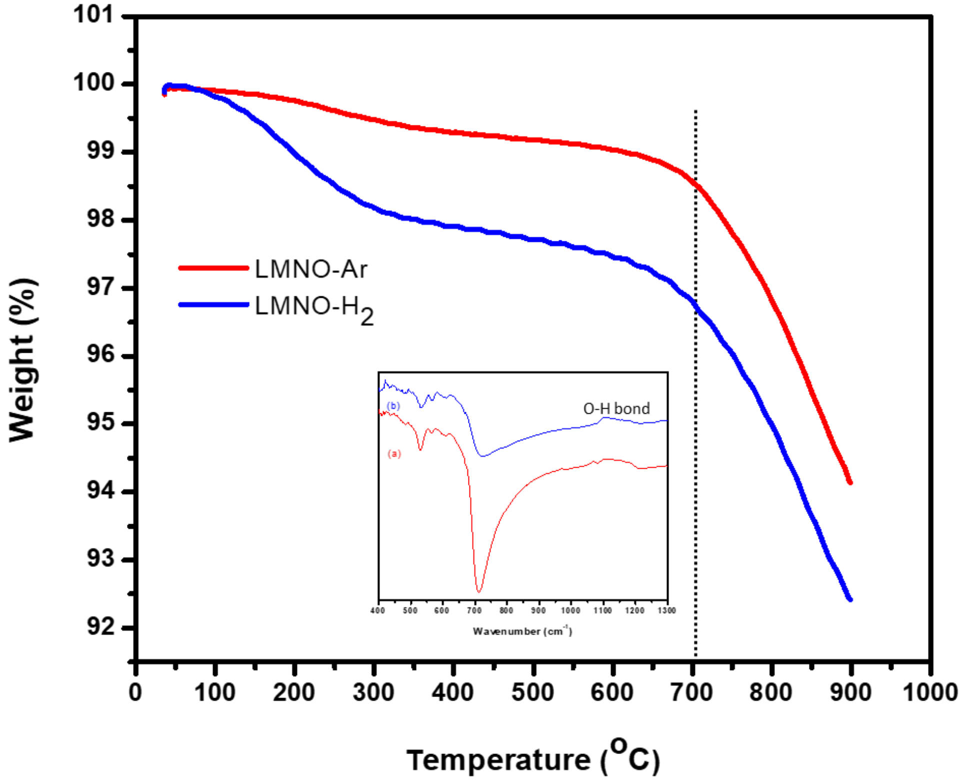

Figure 5.5. Thermogravimetric (TG) curves. The FTIR spectra inserted show

The percentage of oxygen loss by LMNO-Ar sample is higher by ~ 0.1 % than the LMNO-H_2 samples. The amount of oxygen lost depend on the initial oxygen contents of the two samples. Consequently, we can conclude that LMNO-Ar sample has higher oxygen content (lower oxygen vacancy) than LMNO-H_2 sample which has lower oxygen content (higher oxygen vacancy). In other words, LMNO-H_2 sample has higher oxygen vacancy than LMNO-Ar sample. The TGA profiles also shows that LMNO-H_2 has better thermal stability than LMNO-Ar.

5.2.2.3 Synchrotron Powder X-ray Diffraction (SPXRD)

Synchrotron Powder X-ray Diffraction (SPXRD) characterization was carried out at the XPD beamline of LNLS synchrotron facility in Brazil. Measurements were carried out using a custom-built furnace operating in reflection mode geometry and beam energy of 7.5 keV and Mythen strip detector. The PXRD has the advantage of modern beamlines which allow ultrafast measurements at high sensitivity or variable wavelength for depth profile over the conventional PXRD in the laboratory that allow extraction of information on the phase composition of near surface regions [23]. The SPXRD patterns of LMNO-Ar and LMNO-H_2 samples are presented in Figures 5.6 (a and b). The two samples show strong and sharp peaks, thus depict high crystallinity. The PXRD pattern of LMNO-Ar shows higher peak intensities than that of LMNO:H_2. Figures 5.6 (a and b) shows that the two samples have peak (111) positioned at about 18.8^o and other peaks at their respective position identical to the model spinel LMNO structure [24]. Furthermore, the PXRD patterns of the two samples do not have the *super-lattice* peaks (2θ = 15.4°, 39.8°, 45.8° and 57.6°), hence the LMNO-Ar and LMNO-H_2 samples can be indexed to Fd3m symmetry [25]. The magnification of the diffraction patterns between $2\theta = 30^o$ to 70^o (Figure 5.7) shows the presence of secondary (rock salt) phase: weak peaks at 2θ = 37.5^o, 43.6^o and 63.5^o in the diffraction pattern of LMNO-Ar which are not obvious in the diffraction pattern of LMNO:H_2. Thus, it implies that the amount of impurity (rock salt) in the LMNO:H_2 is negligible. This observation is of great interest because we can propose for the first time that the experimental atmospheres used in this research work can be used to control the impurity phase in spinel LMNO. Similar results have been previously reported [24, 26]. Ke et al. [15] reported that the impurity phase in spinel LMNO hinders the mobility of Li^+ in the cathode material, thus lowers the cell capacity. Consequently, the LMNO-Ar sample with higher amount of impurity is expected to have a lower capacity than LMNO-H_2 sample.

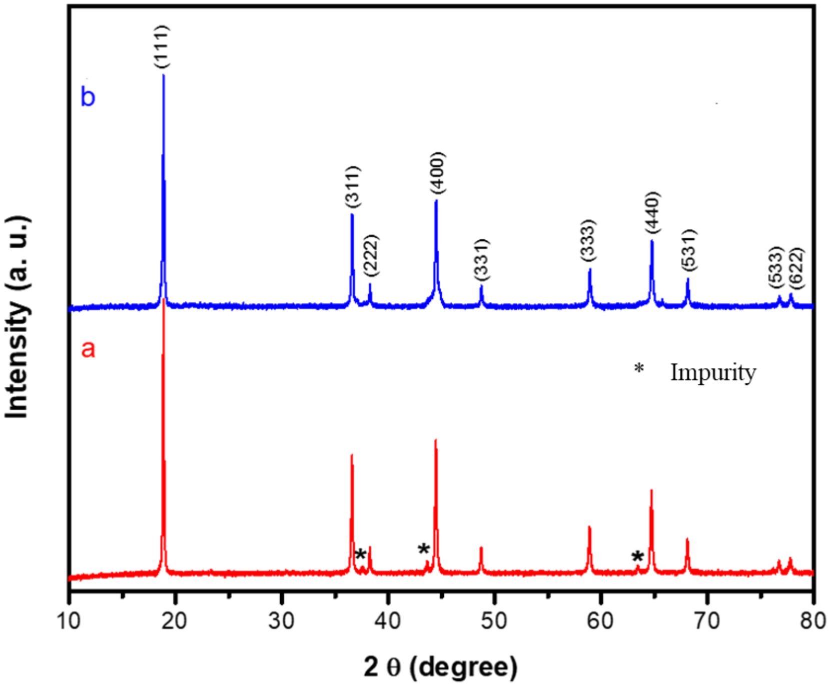

Figure 5.6: SPXRD pattern of (a) LMNO-Ar and (b) LMNO-H_2 samples

In the model spinel LMNO structure, the miller indices (111) has the highest intensity while the miller indices (311) has the highest in the antispinel structure [26, 27]. The miller indices (311) reflect the switching of atoms A/B in AB_2O_4 structure [26] and shows the proneness to form the disordered phase [28]. The peak intensity ratio: I_{111}/I_{311} is a suitable indicator to differentiate between the disordered and ordered phases [28]. Table 5.3

shows that the peak intensity ratio I_{111}/I_{311} for LMNO-Ar and LMNO-H_2 are 2.00 and 2.07 respectively. The model the peak intensity ratio: I_{111}/I_{311} of disordered phase (JCPDS: 32-0581) and ordered phase (JCPDS: 80-2184) are 1.67 and 2.61 respectively as shown in Table 5.3 [28]. Thus, we can infer that the two samples (LMNO-Ar and LMNO-H_2) have disordered and ordered phases because their intensity ratio: I_{111}/I_{311} values are in between that of the JCPDS values [28].

Table 5.3: Comparison of peak intensity ratio

	I_{111}/I_{311}	I_{311}/I_{400}
LMNO-Ar	2.00	0.9117
LMNO-H_2	2.07	0.8999
JCPDS: 32-0581	1.67	
JCPDS: 80-2184	2.61	

The peak intensity ratio I_{111}/I_{311} has been reported to relates to the degree of confusion among the Li^+ and transition metal ions in LMNO. Furthermore, peak intensity ratio I_{111}/I_{311} is inversely proportional to the degree of confusion and the degree of confusion relates inversely to Li transport (conductivity) [26].

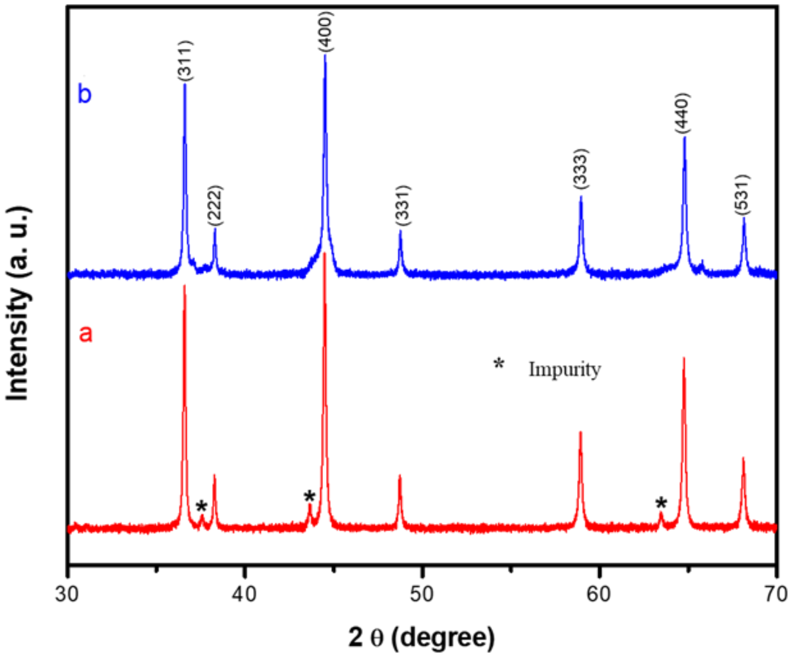

Figure 5.7: The magnification of SPXRD patterns (2θ = 30° to 70°) of the (a) LMNO-Ar and LMNO-H_2

Table 5.3 shows that LMNO-H_2 sample has higher intensity ratio I_{111}/I_{311} (2.07) than the LMNO-Ar sample (2.00). Therefore LMNO-H_2 sample has lower degree of confusion relative to the LMNO-Ar sample. Consequently, LMNO-H_2 sample has smoother path for Li^+ transport and thus better conductivity. Table 5.3 also shows that the ratio I_{311}/I_{400} of LMNO-Ar and LMNO-H_2 are 0.9117 and 0.8999 respectively. The structural stability of spinel LMNO increases with increase in the ratio I_{311}/I_{400} [29]. Therefore, LMNO-Ar has higher structural stability than LMNO-H_2, thus the cycle-performance of LMNO-Ar is expected to be better than LMNO-H_2.

Table 5.4 shows the phase-identification and phase-quantification obtained from the synchrotron XRD measurements of LMNO-Ar and LMNO-H_2 samples carried out by DIFFRAC.EVA (Version 2. 2014) and the ICDD PDF2 database (2016); and Rietveld-method as applied in Bruker AXS TOPAS software (Version 5, 2014) respectively. Table 5.4 shows that LMNO-H_2 cathode material has higher disorder phase Fd3m and order phase P4332.

Table 5.4: Rietveld refinement data for LMNO-Ar and LMNO-H_2 samples

LMNO	Ar (%)	H_2 (%)
Phase 3: Rhombohedral_ $Li_{0.8}Mn_{0.81}O_2$	13.7	
Phase 2: Li(Mn1.5Ni0.5)O4 - FD3M	0.1	5.9
Phase 1: Li(Mn1.5Ni0.5)O4 - P4332	86.2	94.1

5.2.2.4 Fourier-Transform Infrared Spectroscopy (F-TIR)

The Fourier-Transform Infrared Spectroscopy (F-TIR) spectroscopy is a valued analytical method to distinguish between the disordered and ordered structures of spinel LMNO [30]. In the FT-IR spectroscopy, the model ordered spinel LMNO structure shows 8 absorption bands, while that of the disordered spinel LMNO structure shows widen 5 absorption bands [31]. Relative to previous report [32], the spectra of the LMNO-Ar and LMNO:H_2 samples (Figure 5.8) show that the two samples have 8 absorption bands but they are not well defined as the model ordered phase, hence shows that the two samples have some degree of ordered phase. The two samples also have widened peaks at the

Mn-O and Ni-O bands (619/624 and 578/584) cm^{-1} respectively for LMNO-Ar and LMNO:H_2 samples; thus, shows that the two samples have some degree of disordered phase [33]. The two samples' peak intensities at 577 cm^{-1} / 584 cm^{-1} (Ni-O bands) are higher than that of 619 cm^{-1} / 624 cm^{-1} Mn-O and thus signifies that the two samples have some degree of ordered phase [34]. Furthermore, the wave bands at 555 cm^{-1} and 669 cm^{-1} (approx.) in the spectra of the two samples correspond to the ordered phase [35]. Thus, also confirms that the two samples have some degree of ordered phase. The seeming shoulders (429 and 669) cm^{-1} bands depicts that LMNO-Ar sample has a higher degree of cation order that of LMNO-H_2 sample [26]. Therefore, we can conclude that the two samples have partial disordered and ordered structures. The band shift from 584 cm^{-1} to 578 cm^{-1} also confirm that LMNO-Ar sample has a higher degree of cation order [26]. The intensity increase of Ni-O band (584 cm^{-1}) and intensity decrease of Mn-O band (619 cm^{-1}) of LMNO Ar sample relative to intensity decrease of Ni-O band (584 cm^{-1}) and intensity increase of Mn-O band (624 cm^{-1}) of LMNO H_2 sample as shown by represented by x and y in Figure 8 shows that LMNO Ar sample has higher degree of ordered phase than LMNO H_2 sample [6]. The LMNO-H_2 spectrum shows a sharper OH shoulder at ~ 1100 cm^{-1} [21] than that of LMNO-Ar spectrum. This is due to higher oxygen vacancy in LMNO-H_2 which reflects higher defects content in the sample.

Consequently, we can propose that the LMNO-Ar sample has a lower oxygen vacancy content than the LMNO-H_2 sample.

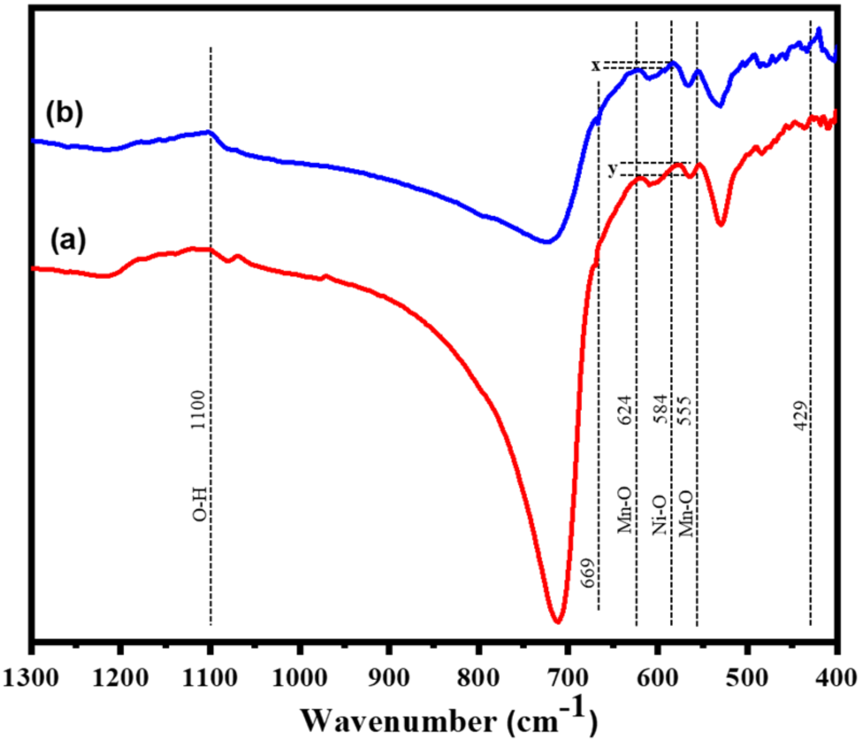

Figure 5.8: FT-IR spectra of (a) LMNO-Ar and (b) LMNO-H_2

5.2.2.5 Raman Spectroscopy (R S)

Raman spectroscopy is a sensitive technique to probe the local environments of spinel LMNO. Thus, the degree of disorder/order of the structure of the LMNO-Ar and LMNO:H_2 samples is examined by Raman spectroscopy. The RS of LMNO-Ar and LMNO:H_2 are shown in Figure 5.9. The active bands are 623, 589, 487, 382 and 157 cm^{-1}. Relative to previous literature [36, 37], the peaks at 623 relates to the A_{1g} mode: (Mn-O) symmetry vibration stretching of MnO_6. The bands at 601 and 589 cm^{-1} signify Mn/Ni ordering phase [37], however, these peaks are neither resolved as the perfect disordered phase nor ordered phase [32].

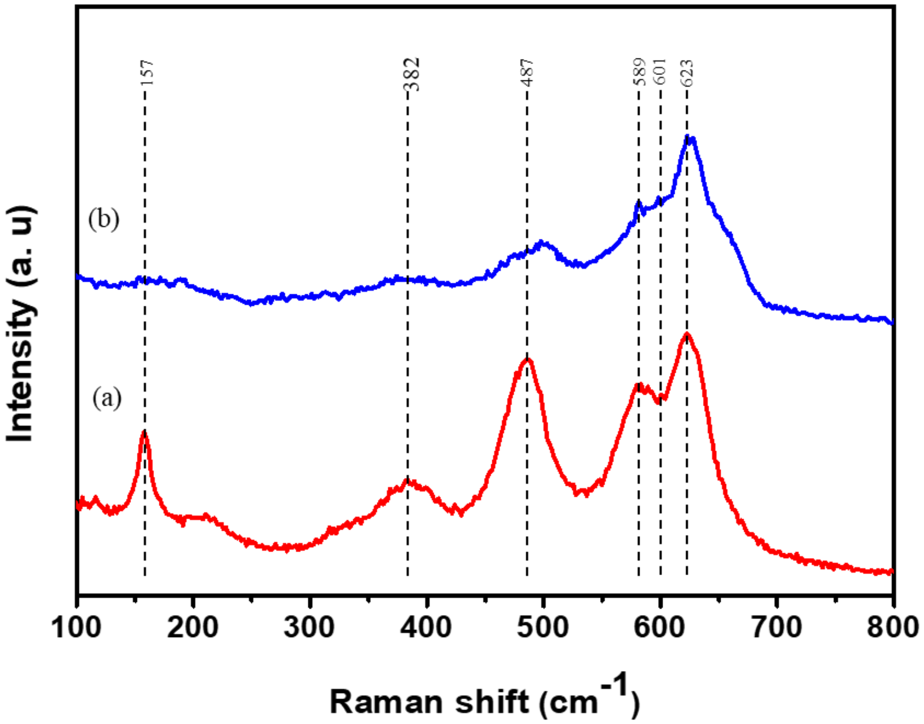

Figure 5.9: Raman spectra of (a) LMNO-Ar and (b) LMNO-H_2

But the two samples show resolution within the perfect disordered and ordered phases with the LMNO-Ar sample showing better distinction. Therefore, we can deduce that the two samples have the coexistence of the two phase (disordered and ordered) and LMNO-Ar has a higher degree of ordered phase. The wave bands at 487, 382 and 157 cm^{-1} relate to the Ni-O band [37, 38]. The spectrum of LMNO-H_2 sample has only active bands at 625 and 498 cm^{-1}, therefore the structure has more disorder phase than LMNO-Ar [36]. Similar to the Lethien et al. [38] report, the Ni-O band increased intensity at 157 cm^{-1} in LMNO-Ar relative to LMNO-H_2 correlates to higher degree of ordered phase in LMNO-Ar sample than that of LMNO-H_2. Furthermore, Amatucci et al. [34] stated that ordered phase peaks are well resolved and sharper than disordered phase, which confirms that LMNO-Ar sample has higher degree of ordered phase than LMNO-H_2 sample. Zhang et al [37] has reported similar observation from their research work on tri-doping (Cu^{2+}, Al^{3+} and Ti^{4+}) of LMNO. Consequently, Raman spectroscopy has shown that LMNO-H_2 sample has higher degree of disordered phase than LMNO-Ar. The RAMAN spectroscopy results are consistent with that of the FT-IR spectroscopy.

5.2.2.6 Nitrogen Gas Adsorption analysis

The LMNO-Ar and LMNO-H_2 samples surface areas were examined by the Nitrogen Gas Adsorption analytical technique. The LMNO-H_2 sample has higher values for surface area, pore size and volume than the LMNO-Ar sample as shown in Table 5.5. The higher surface area of the LMNO-H_2 sample offers larger area for Li^+ extraction and insertion [39] which enhance the conductivity (capacity) of the electrode in the charge-discharge processes. The LMNO-H_2 sample higher surface area correspondingly offers larger electrode-electrolyte surface contacts which increase the side reactions at the interface and thus causes the LMNO-H_2 cathode material to degrade faster during cycling. These observations are expected to reflect in the charge-discharge performances of the LMNO-Ar and LMNO-H_2 electrodes during cycling.

Table 5.5: Nitrogen Gas Adsorption analysis of LMNO-Ar and LMNO-H_2 samples

	LMNO-Ar	LMNO:H_2	% Increase
Surface area (m^2g^{-1})	6.96	7.90	14
Pore-volume (cm^3g^{-1})	0.108	0.132	22
Pore-size (nm)	60.05	67.04	12

5.2.2.7 X-ray-absorption near-edge spectroscopy (XANES)

The oxidation states of Mn and Ni in the LMNO-Ar and LMNO:H_2 samples were examined by XANES. Figure 5.10 shows that the Mn K-edge spectra of the two samples are similar.

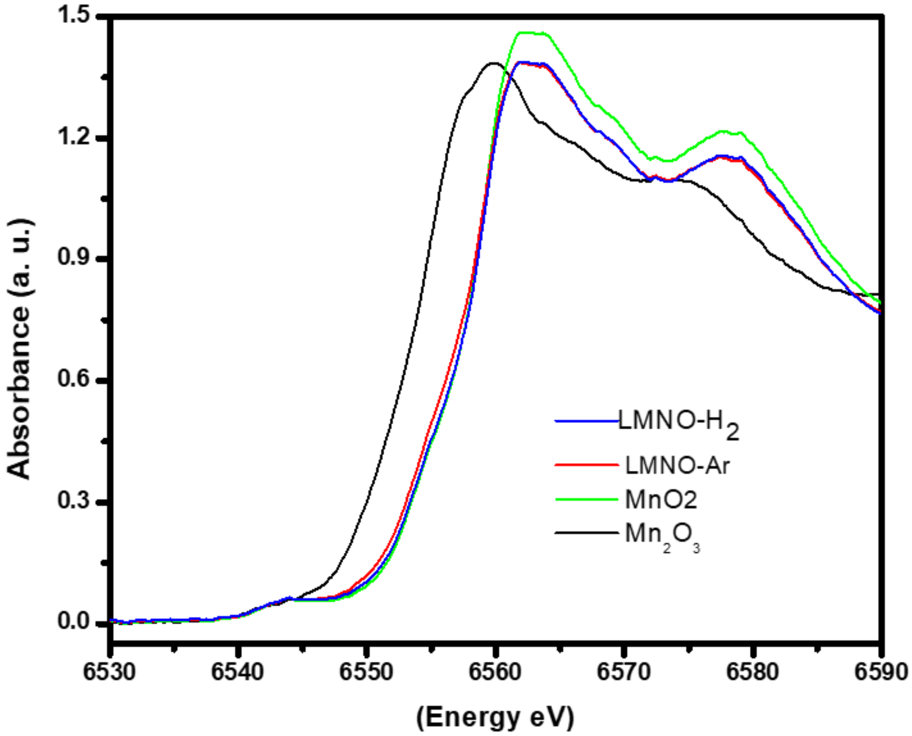

Figure 5.10: Mn K-edge XANES (LMNO-Ar and LMNO-H_2 samples with Mn_2O_3 and MnO_2 standards)

Figure 5.11 also shows that the two samples have similar spectra for Ni K-edge. The Mn and Ni K edge of the samples' spectra have weak pre-edge regions. The Mn K-edge of LMNO-Ar and LMNO:H_2 samples are positioned within that of the Mn^{3+} and Mn^{4+}standards (Figure 5.10). This shows the co-existence of the two phases: Mn^{3+} (disordered) and Mn^{4+} (ordered) in the LMNO-Ar and LMNO-H_2 samples [40] and the Mn oxidation state is between +3 and +4 [4]. Figure 5.11 shows the *Ni K*-edge spectra of the two samples and the Ni standards [NiO (Ni^{2+}) and Ni_2O_3 (Ni^{3+})]. Figure 5.11 reveals that the spectra of the two samples are very close to that of the Ni^{2+} and no significant change in the spectra of the LMNO-Ar and LMNO:H_2 samples. Thus, confirms that the Ni in the two samples exist as Ni^{2+} [5]

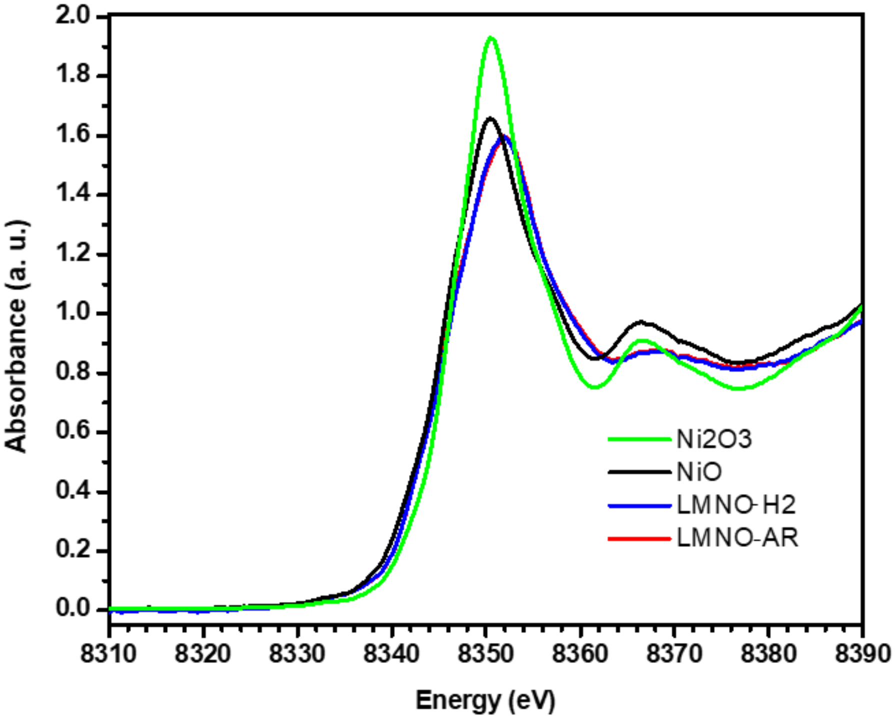

Figure 5.11: Ni K-edge XANES (LMNO-Ar and LMNO:H_2 samples with NiO and Ni_2O_3 standards)

5.2.2.8 Powder Neutron Diffraction (PND)

Figure 5.12 show the power neutron diffraction patterns (PND) of the LMNO-Ar and LMNO-H_2. The diffraction pattern of the LMNO-H_2 sample shows peaks shift to towards the lower angles. The shift of the lower angles in the main reflections of the LMNO-H_2 is consistent with the unit cell expansion [41] The PND Rietveld refinement showed that LMNO-H_2 has higher value for lattice parameter (8.27246 Å) than LMNO-Ar (8.18073 Å). The increased lattice parameter of LMNO-H_2 can be related to the increase in its Mn^{3+} content. This is because the Mn^{3+} ionic radius (0.65 Å) is higher than that of Mn^{4+} (0.54 Å) [42, 43]. Thus, the increased Mn^{3+} ionic radius in LMNO-H_2 led to its bigger cell volume of 566.11 Å^3 than that of LMNO-Ar (547.49 Å^3). Consequently, LMNO-H_2 has larger cell volume which offered better Li^+ path for higher electronic and ionic conductivity than the lower cell volume of LMNO-Ar [44, 45].

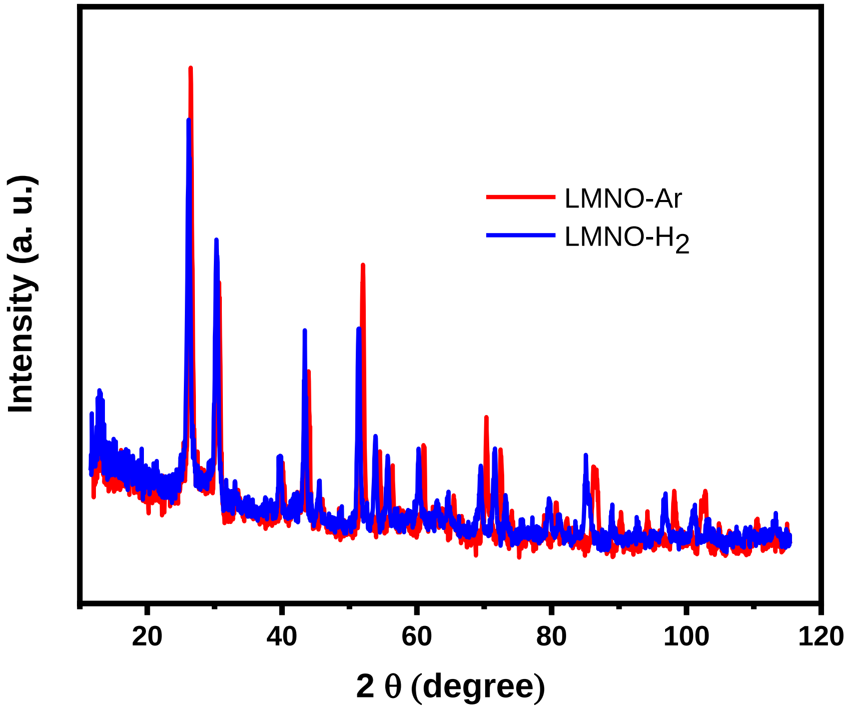

Figure 5.12: PND of LMNO-Ar and H_2

5.2.2.9 Synchrotron X-ray Photoelectron Spectroscopy (SXPS)

Figure 5.13 and Figure 5.14 show the deconvoluted spectra (Mn $2p_{3/2}$ SXPS) of LMNO-Ar and LMNO-H_2 cathode materials. Table 5.6 displays values obtained from the fitted peaks. The Mn $2p_{3/2}$ SXPS binding energy of Mn^{3+} on the surface of LMNO-Ar and LMNO-H_2 samples are positioned at 642.1 eV and 643.5 eV respectively.

While the Mn $2p_{3/2}$ SXPS binding energy of Mn^{4+} on the surface of LMNO-Ar and LMNO-H_2 cathode are positioned at 643.8 eV and 645.9 eV respectively. Similar binding energies has been reported by Banerjee et al [46].

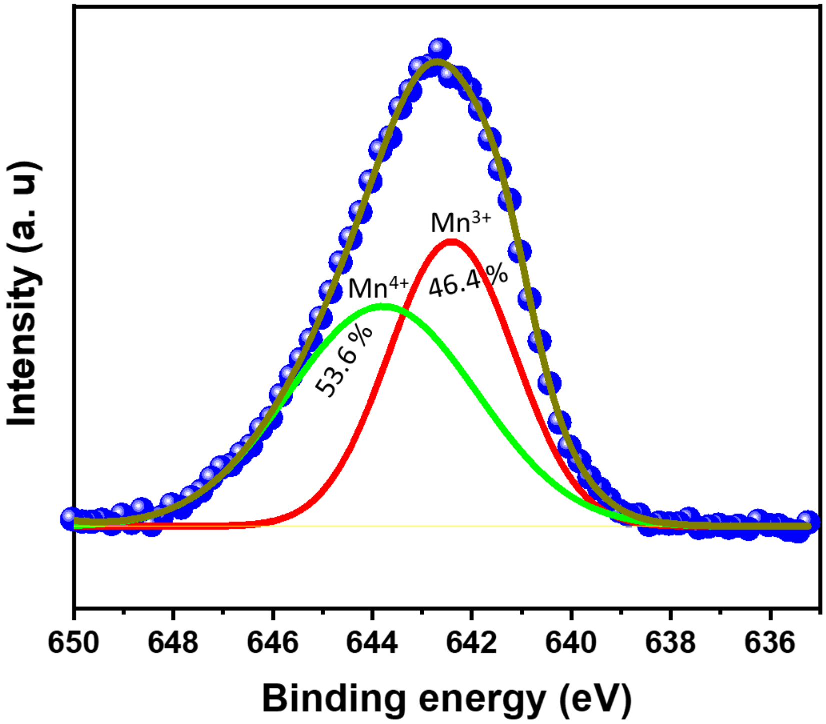

Figure 5.13: Mn $2p_{3/2}$ SXPS spectra of LMNO-Ar cathode material

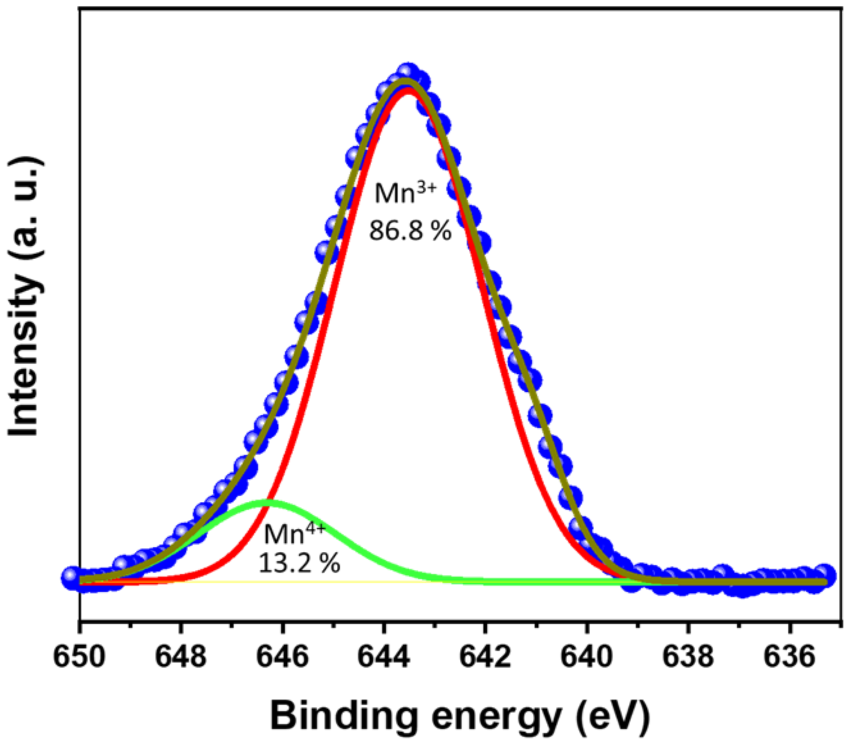

Figure 5.14. Mn $2p_{3/2}$ SXPS spectra of LMNO-H_2 cathode material

The LMNO-H_2 cathode material's Mn^{3+} content (81.4%) is greater than that of the LMNO-Ar (45.7%). The results further confirmed the presence of Mn^{3+} (disordered phase) and Mn^{4+} (ordered phase) on the surface of the two samples. And the Mn^{3+} content on the surface of LMNO-H_2 is more than that on the surface of LMNO-Ar. The presence of Mn^{3+} in the SXPS spectra of LMNO-Ar and LMNO-H_2 can be attributed to oxygen vacancy's occurrence [47] and higher percentage of Mn^{3+} in LMNO-H_2 can be ascribed to higher

oxygen content [48, 49]. This result agrees with the results of the SXRD, FTIR, Raman, XANES and GCV. Figure 5.15 shows the SXPS spectra (Ni $2p_{3/2}$) of LMNO-Ar and LMNO-H_2. The LMNO-Ar has a Ni $2p_{3/2}$ SXPS binding energy is positioned at 854.7 eV while

LMNO-H_2 sample has its binding energy is positioned at 8555.5. Wen et al [50] reported identical results. LMNO-H_2 sample has a bigger peak area (4036.7 CPSeV) than LMNO-Ar sample (2826.4 CPSeV). This result shows that LMNO-H_2 cathode material's surface has more Ni content than on the LMNO-Ar surface [51]. This is because more of the Ni content in LMNO-Ar surface has been used up in the impurity formation [52].

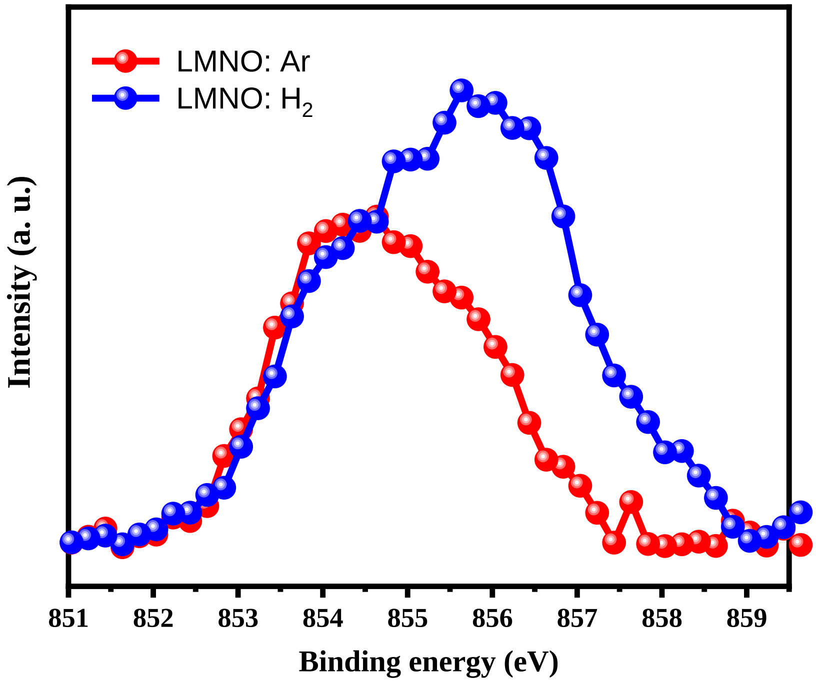

Figure 5.15. Ni $2p_{3/2}$ SXPS spectra of LMNO-Ar and LMNO-H_2 cathode material

Figures 5.16 and 5.17 and Table 5.6 show the fitted Ni $2p_{3/2}$ XPS spectra and data analysis of LMNO-Ar and LMNO-H_2 cathode materials. The fitted spectrum of LMNO-Ar has only one peak sited at binding energy of 854.7 eV. This peak can be allotted to Ni^{2+} as the value is similar to 854.8 eV cited by Wen et al. [50]. The LMNO-H_2 fitted spectrum showed two peaks and their binding energies are positioned at 853.1 eV and 855.5 eV respectively. The binding energy at 853.1 eV can be assigned to Ni^0 [53]. The high oxygen vacancy environment in the LMNO-H_2 sample may have caused the reduction of the Ni^{2+} to Ni^0.

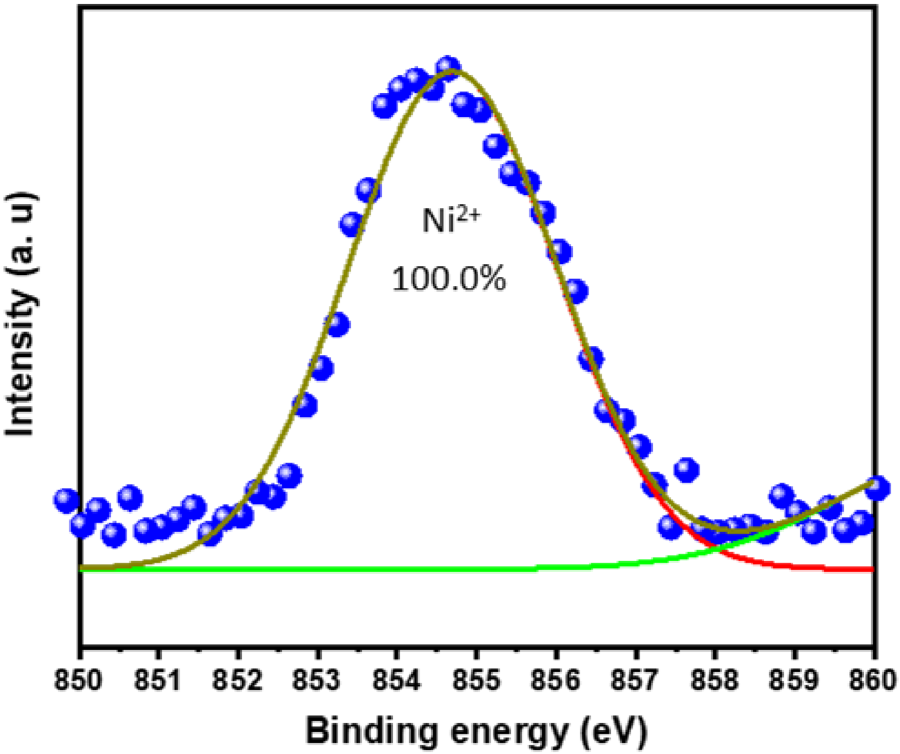

Figure 5.16. Ni $2p_{3/2}$ SXPS spectra of LMNO-Ar cathode material

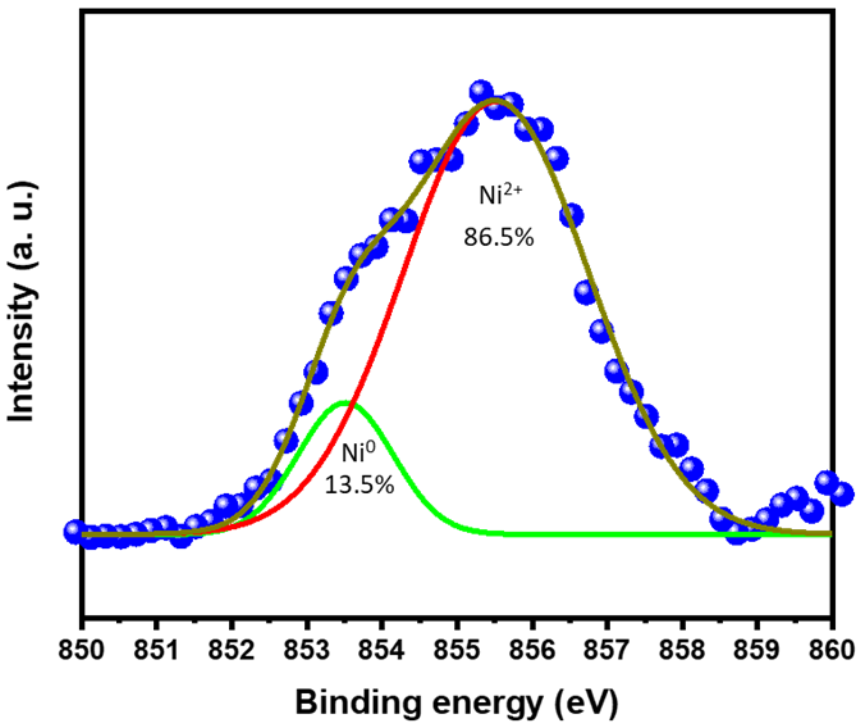

Figure 5.17. Ni 2p$_{3/2}$ SXPS spectra of LMNO-H$_2$ cathode material

Table 5.6. SXPS analysis results: LMNO-Ar and LMNO-H$_2$ cathode materials.

	Binding energy (eV)		**%**		**Binding energy (eV)**			**%**		
Sample	Mn^{3+}	Mn^{4+}	Mn^{3+}	Mn^{4+}	Ni^0	Ni^{2+} (NiO)	Ni^{2+} (Ni(OH)$_2$)	Ni^0	Ni^{2+} (NiO)	Ni^{2+} (Ni(OH)$_2$)
LMNO-Ar	642.1	643.8	45.7	54.3		854.7			100	
LMNO-H$_2$	643.5	645.9	81.4	18.6	853.1		855.5	13.5		86.5

McWinnie et al. [54] reported the binding energy of 853 eV for Ni^0 which they stated probably resulted from the reduction of Ni^{2+} in the aggressive chemical environment created by the etching experiment. The binding energy at 855.5 can be assigned to Ni^{3+}

(855.6 eV [45]) or Ni^{2+} ($Ni(OH)_2$) (855.5 eV [49]). Wen et al. [50] assigned the binding energy at 855.5 eV to $Ni^{3+}$and cited previous reports that suggested the increased binding energy (855.5 eV) resulted from the partial oxidation of Ni^{2+} to Ni^{3+}. Ikeda's et al. [57] reported that the peak at 855.5 can be assigned to Ni^{2+} ($Ni(OH)_2$). The hydrogen bonding occurred due to the transfer electron from the proton-accepting-species to the antibonding orbital of O-H bond of the proton-donating-species. The results showed that there was a reaction between oxygen and a higher oxygen vacant oxide of Ni^{2+} [58]. The CV of LMNO-H_2 has only one peak at 4.7V, hence it showed the presence of only Ni^{2+} [52]. The XANES result also showed that in LMNO-H_2 the Ni exists as Ni^{2+}. The FT-IR further confirmed the presence of OH bond in the LMNO-H_2 sample. Consequently, we can evidently assign the binding energy 855.5 eV to Ni^{2+} and not Ni^{3+}. This finding also proved that LMNO-H_2 is of higher oxygen vacancy.

5.2.2.10 Transmission *E*lectron *M*icroscopy (TEM)

Figure 5.18 shows the TEM images of LMNO-Ar cathode material at high and low magnifications, while Figure 5.19 shows the same for LMNO-H_2 cathode. The two cathode materials have similar rod-like shape. Hence the morphology has insignificant impact on the electrodes' electrochemistry.

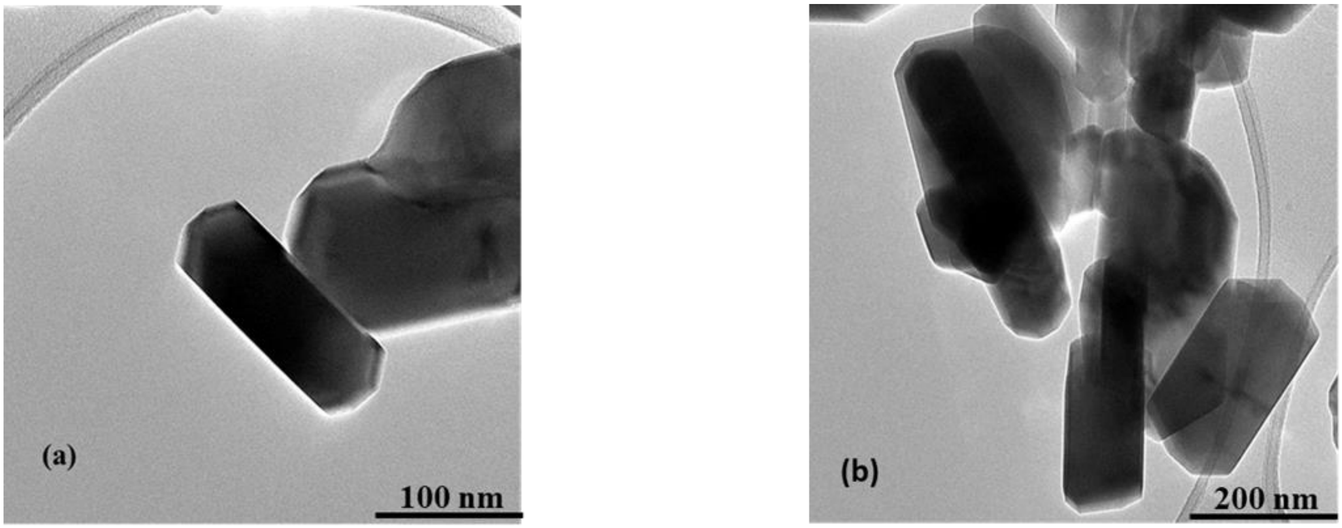

Figure 5.18: TEM images (LMNO-Ar)

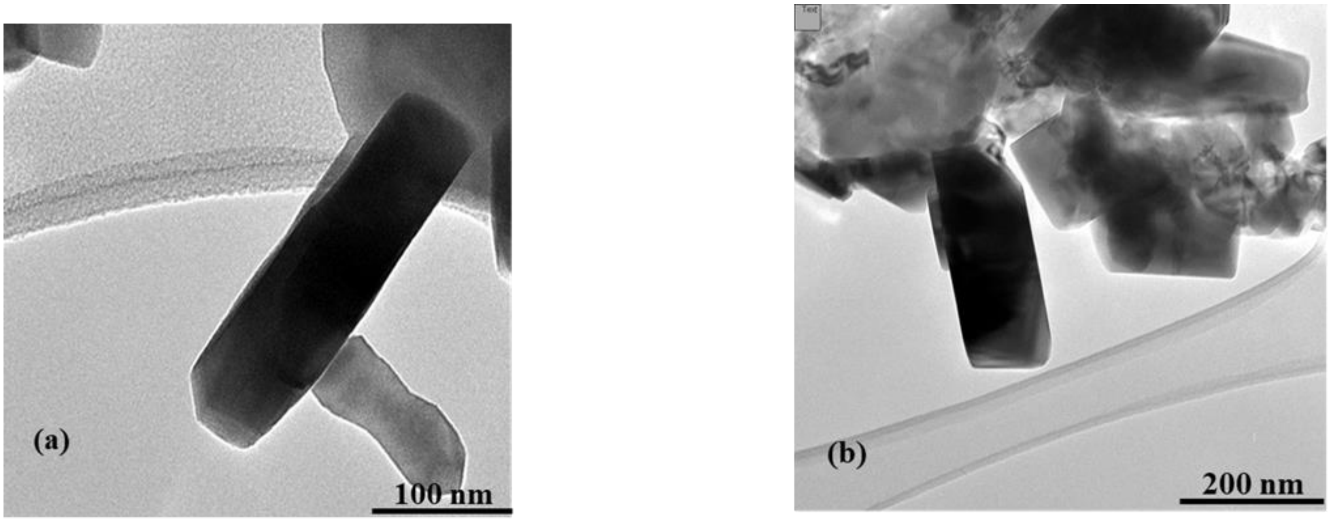

Figure 5.19: TEM images (LMNO-H_2)

5.2.3 Electrochemical Measurements

5.2.3.1 Cyclic voltammetry (C V)

The cyclic voltammetry (C V) of the LMNO-Ar and LMNO-H_2 electrodes at 0.1 mVs^{-1} were examined to reveal the redox reactions during cycling. Figure 5.20: shows the C V of the two samples between 2.0 to 4.9 V. The C V curves of the two samples are very similar and consists of three redox peaks in the regions 2.5 – 3.0 V, around 4 V and 4.5 – 4.9 V. The strong peaks at the lower voltages: anodic peak ~ 3.1 V and cathodic peak ~ 2.6 V reflect the electrochemical activity of the Mn^{3+}/Mn^{4+} redox reactions [59, 60]. The small peak about 4.0 V signifies the signature of Mn^{3+} / Mn^{4+} redox reactions [58, 61] thus the two samples have some contents of Mn^{3+}. Consequently, we can conclude that the two samples have

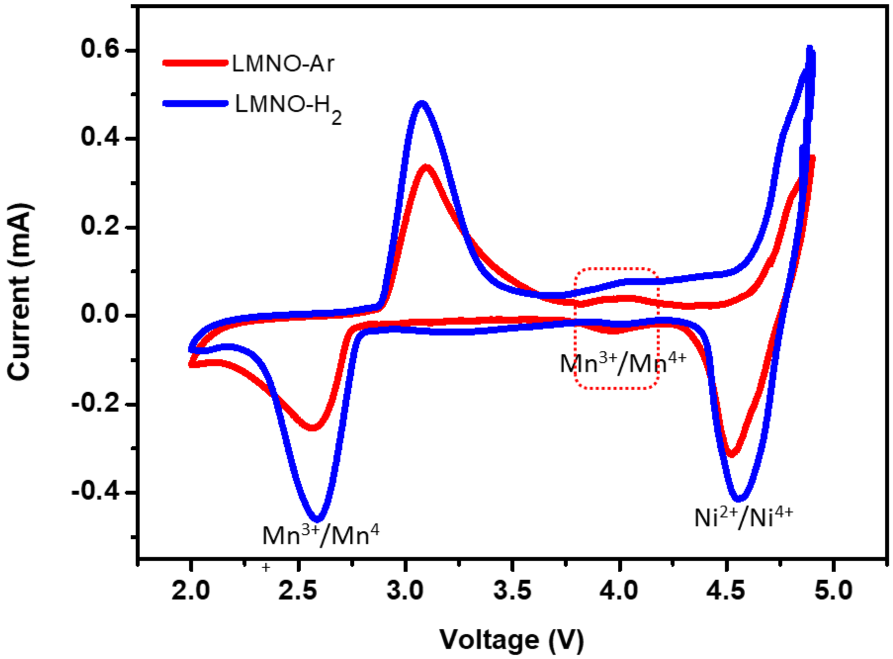

Figure 5.20: C V: LMNO-Ar and LMNO:H_2 samples

some degree of disordered phase which is consistent which the results of the analytical techniques described in the sessions above. The peak area around 4.0 V reflects the Mn^{3+} content in the LMNO-Ar and LMNO-H_2 cathode materials [51]. The area of peak in 4.0 V region of LMNO-H_2 electrode is greater than that of LMNO-Ar, therefore the Mn^{3+} content in LMNO-H_2 cathode is more than that of the LMNO-Ar. Whittingham et al. [63] atomistic simulation and experimental results shows that Mn^{3+} content changes directly with degree of disorder. Hence, LMNO-H_2 cathode material has a higher degree of disorder than LMNO-Ar. The LMNO-H_2 cathode material having higher degree of disorder phase is expected to have better electronic and Li^+ conductivity than LMNO-Ar because of its higher Mn^{3+} content and thus higher specific capacity. Furthermore, the LMNO-H_2 cathode material will have higher capacity fading during cycling than the LMNO-Ar, because of the disproportionation reaction of the Mn^{3+} [62]. In addition, Whittingham [63] and Zhou's [61] groups reported that the Mn^{3+} content in spinel LMNO reflects the oxygen vacancy. Therefore, we can propose that LMNO-H_2 cathode material has higher oxygen vacancy than LMNO-Ar. Liang et al. [58] reported that disordered phase spinel LMNO has two separate peaks at high voltage Ni redox reactions (Ni^{2+}/Ni^{3+} and Ni^{3+}/Ni^{4+}) while the ordered phase spinel LMNO has only one corresponding peak (Ni^{2+}/Ni^{4+}). Consequently, we can reiterate that LMNO-Ar and LMNO-H_2 cathode materials have the co-existence of both disordered and ordered phases structures. Which is consistent with the revelations by PXRD, FTIR, RAMAN, and XANES analytical results. The LMNO-Ar and LMNO-H_2 electrodes' anodic and cathodic peaks ~ 4.9 and ~ 4.5V respectively corresponds to the Ni^{2+}/Ni^{4+} redox. The two samples have only one strong peak at these voltage regions. Hence, the LMNO-Ar and LMNO-H_2 electrodes' have some degree of ordered phase symmetries in their crystal structure.

5.2.3.2 Electrochemical Impedance Spectroscopy (EIS)

The electrochemical performances of LMNO-Ar and LMNO-H_2 cathode materials were examine by EIS measurements. The Nyquist plots at OCV Vs Li/Li^+ and room temperature of the two electrodes (Figure 5.21) show intercept in the high-frequency area of the real impedance (Z') axis, a semicircle in the middle-frequency area, and a sloping line in lower-frequency area.

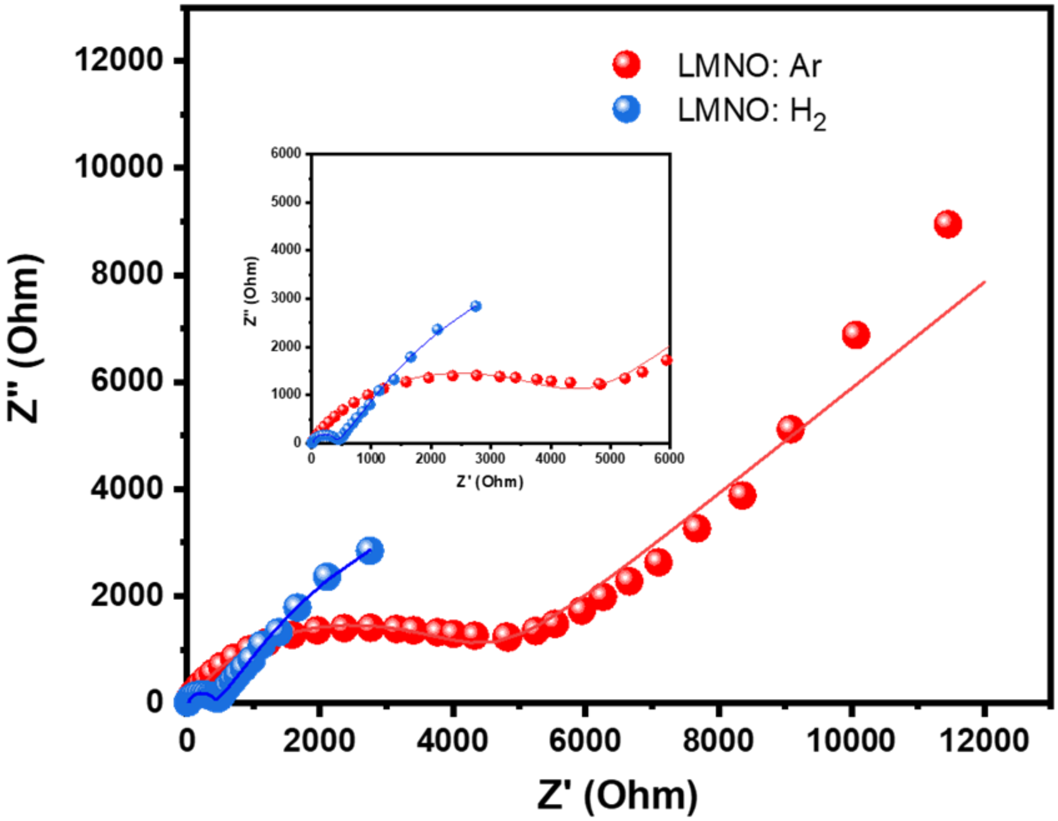

Figure 5.21: Nyquist plots LMNO-Ar and LMNO-H_2. Insert is the magnification of the Z" and Z' from 0 to 6000 Ω

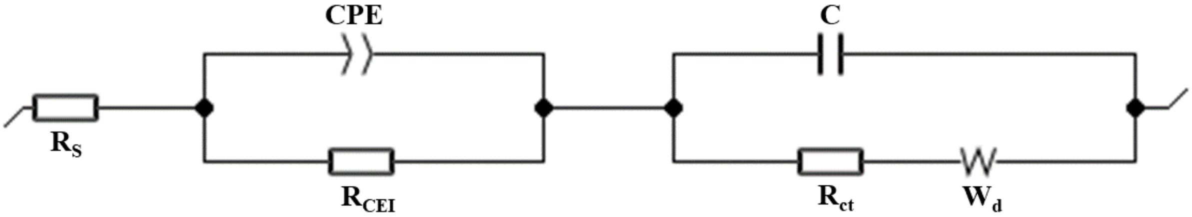

Figure 5.22: The Equivalent-circuit for LMNO-Ar and LMNO-H_2

The spectral of the samples were fitted with parameters in Table 5.7 described by the equivalent circuit shown in Figure 5.22: the electrolyte resistance (Rs), constant phase element (CPE), cathode electrolyte interface resistance (R_{CEI}), capacitance (C), charge transfer resistance (Rct) and Warburg impedance (W_d). The Rs for LMNO-Ar and LMNO-H_2 are 22.1 Ω and 23.1 Ω respectively. This is because the same electrolyte is used for the two samples, hence they have almost the same value for Rs. The LMNO-H_2 electrode has a higher R_{CEI} (2825 Ω than that of LMNO-Ar (34.1 Ω). Edstrom et al. [64] termed the occurrence of the R_{CEI} as interface phenomena which occur when two different phases come in contact (e.g. electrode and electrolyte). The R_{CEI} is based on the surface reaction of electrode–electrolyte interface. The CEI reactions and inorganic species formed are functions of the electrode material. Therefore, LMNO-H_2 electrode having more reactive oxidized surface Ni as a result of higher oxygen vacancy caused more oxidation of the electrolyte at the interface to produce more inorganic species on surfaces. Also, the LMNO-H_2 electrode has more surface Mn^{3+} which dissolves from the spinel into the electrolyte by the disproportionation reaction [15]. Consequently, LMNO-H_2 cathode has higher value for R_{CEI} than LMNO-Ar electrode. All these occurrences are cumulative effects of difference in oxygen vacancy contents in the two electrodes.

Figure 5.7. EIS fitted parameters.

Electrode	R_s (Ω)	CPE (μF.s$^{(a-1)}$)	a	R_{CEI} (Ω)	C (μF)	R_{CT} (Ω)	W_d (Ωs$^{-0.5}$)
LMNO-Ar	22.1	$7.9e^{-3}$	0.71	34.1	$7.9e^{-3}$	4153	1900.0
	+/- 0.2862	+/- $37.9e^{-6}$	+/- 0.5022	+/- 11.15	+/- $2.406e^{-3}$	+/- 29.11	+/- 0.2229
LMNO-H_2	23.1	9.5	1.00	2825.0 +/-	$3.4e^{-3}$	353.9	383.7
	+/- 0.3643	+/- 0.3579	+/- 1.00	33.27	+/- $24.23e^{-6}$	+/- 0.7725	+/- 2.015

The Rct and W_d of the LMNO-H_2 cathode are smaller than that of LMNO-Ar. The LMNO-H_2 has a Rct value of 353.9 Ω which is significantly lower than the LMNO-Ar (4153.0 Ω) . Consequently, the kinetics of Li^+ transport in LMNO-H_2 is enhanced relative to the LMNO-Ar. Similarly, the LMNO-H_2 has lower W_d (383.7 Ω) than LMNO-Ar (1900.0 Ω), which illustrated the faster kinetics of Li^+ diffusion in LMNO-H_2. These higher impedance values for LMNO-Ar can be attributed to its higher impurity phase that impeded the Li^+ mobility in the electrode material [15]. Thus, it can be inferred that LMNO-H_2 cathode materials a higher conductivity than LMNO-Ar. This effect can be attributed to the higher oxygen vacancy content in the LMNO-H_2 cathode material which induced higher amount of Mn^{3+} that enhanced higher electronic and Li^+ conductivity. Therefore, we can propose that the higher oxygen vacancy in LMNO-H_2 cathode material caused the higher conductivity and thus the lower the overall impedance (LMNO-Ar and LMNO-H_2 has total impedance of 6109.3 Ω and 3585.7 Ω respectively).

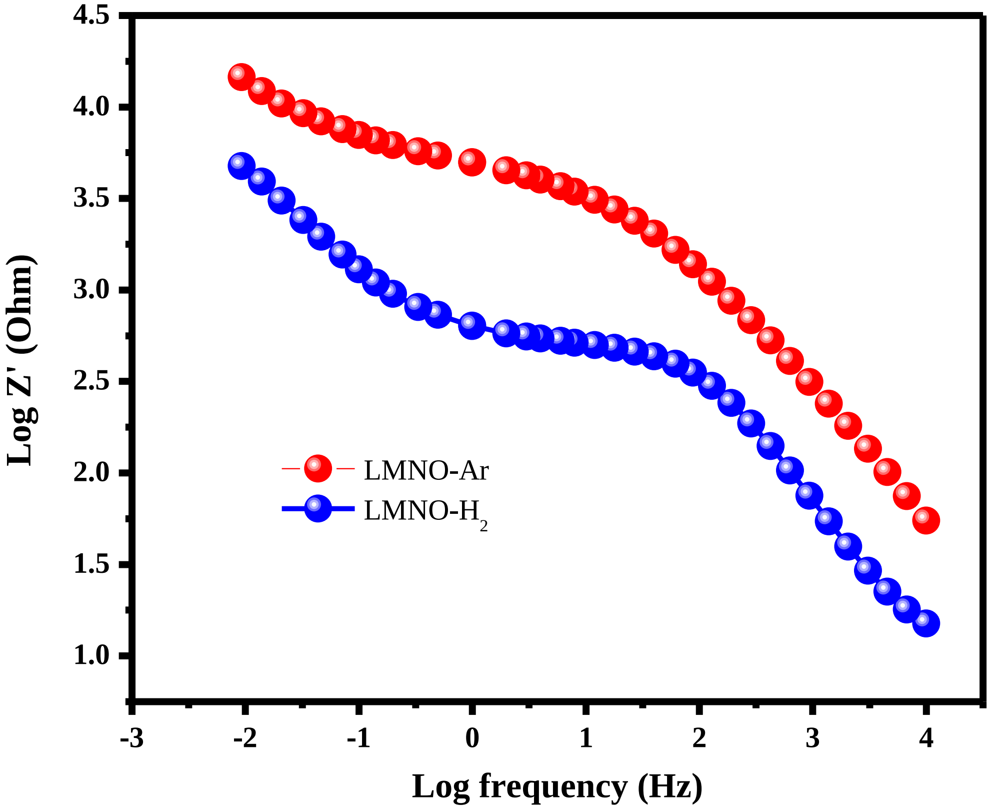

Figure 5.23: Bode magnitude plot

In addition, the Bode plot of the real impedance (Z') against the frequency (Figure 5.23) is used to reveal the clear difference between the conductivities of the two materials. The Figure 5.23 revealed that the LMNO-Ar cathode material has a significant increase in the *charge-transfer* resistance and solid-state Li^+ diffusion into the bulk cathode respectively [65] than the LMNO-H_2 cathode material. Unlike the Nyquist plot fit data that has a higher value of R_{CEI} for LMNO-H_2 in the high frequency area than LMNO-Ar, the Bode plot showed that LMNO-H_2 has a lower impedance in the high frequency region. This is because the observed increase in R_{CEI} for LMNO-H_2 by Nyquist plot resulted from the degradation of the active materials or the inorganic species produced on surfaces of the electrode and electrolyte by the more reactive surface Ni reaction with the electrolyte. Consequently, there was increase in the Li^+ diffusion resistance through the surface layer

(CEI) which is not electron insulating layer. The EIS results confirm the GC-D measurements that showed that LMNO-H_2 cathode material has higher specific capacity as a result of higher conductivity caused by its higher Mn^{3+} content which was induced by the higher oxygen vacancy. The Bode phase angle plots of the LMNO-Ar and LMNO-H_2 are displayed in Figure 5.24 and 5.25. The slope of the Bode plots gives values less than 1 with R^2 values very close to 1. Hence the electrodes are not having capacitance surface as depicted by Nyquist fit, but have constant phase element surfaces consistent with battery materials.

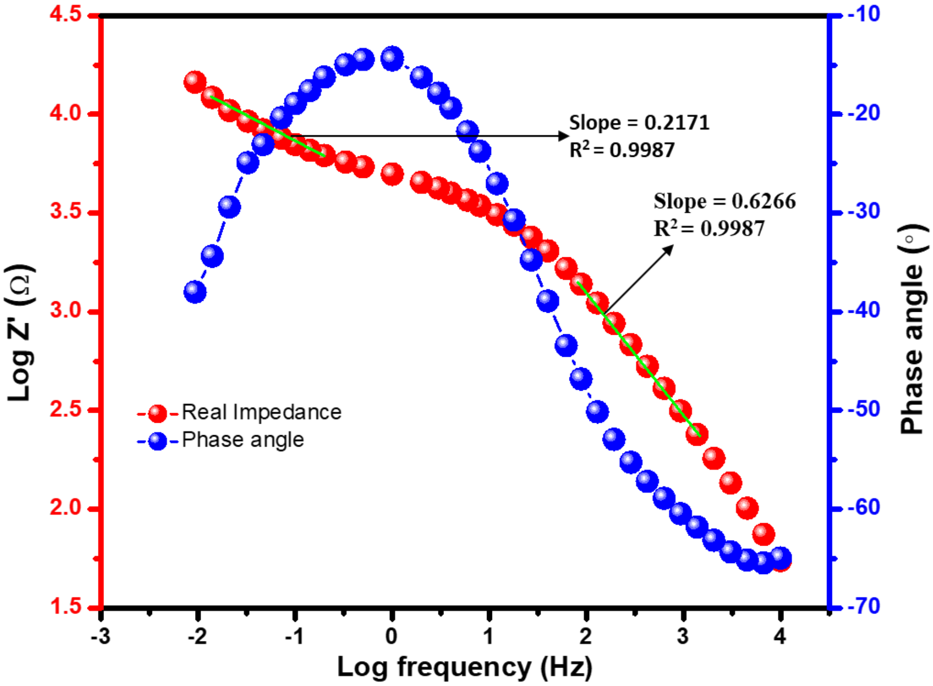

Figure 5.24: Bode plots - LMNO-Ar electrode

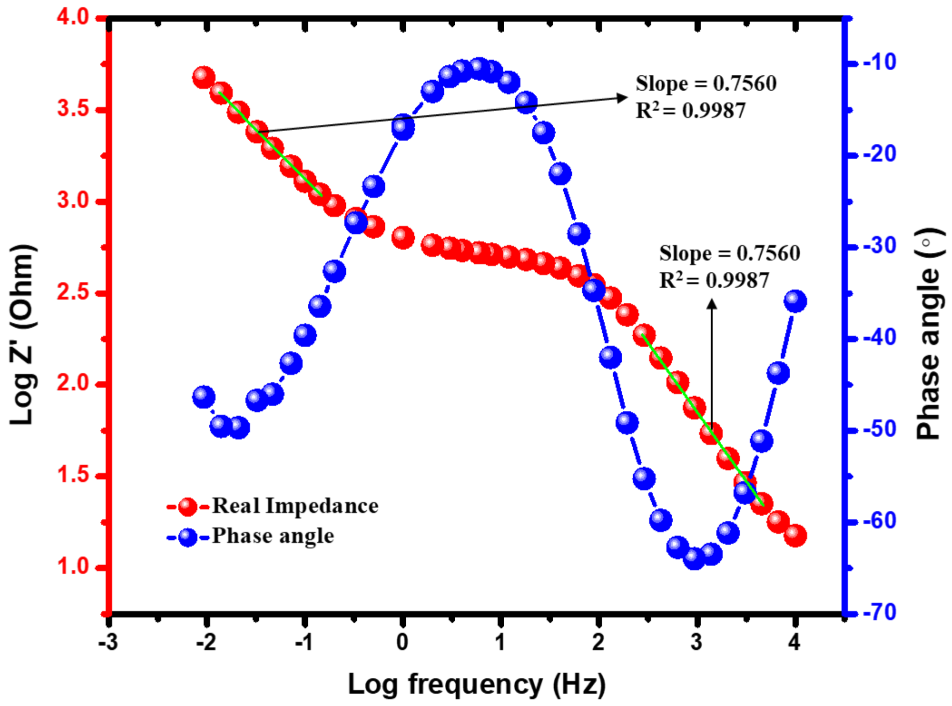

Figure 5.25. Bode plots - LMNO-H_2 electrode

5.2.3.3 Galvanostatic charge-discharge (GC-D)

Figure 5.26 shows the GC-D profiles of LMNO-Ar and LMNO-H_2 cathode materials at 0.1 C rate. The LMNO-H_2 has specific capacity of 113.6 $mAhg^{-1}$ and it decays to 54.9 $mAhg^{-1}$ at cycle number 50 (retention capacity: 48.3%). The specific capacity obtained for LMNO-Ar cathode material is 90.1 $mAhg^{-1}$ and decay to 69.9 $mAhg^{-1}$ at cycle number 50 (capacity retention: 77.6%).

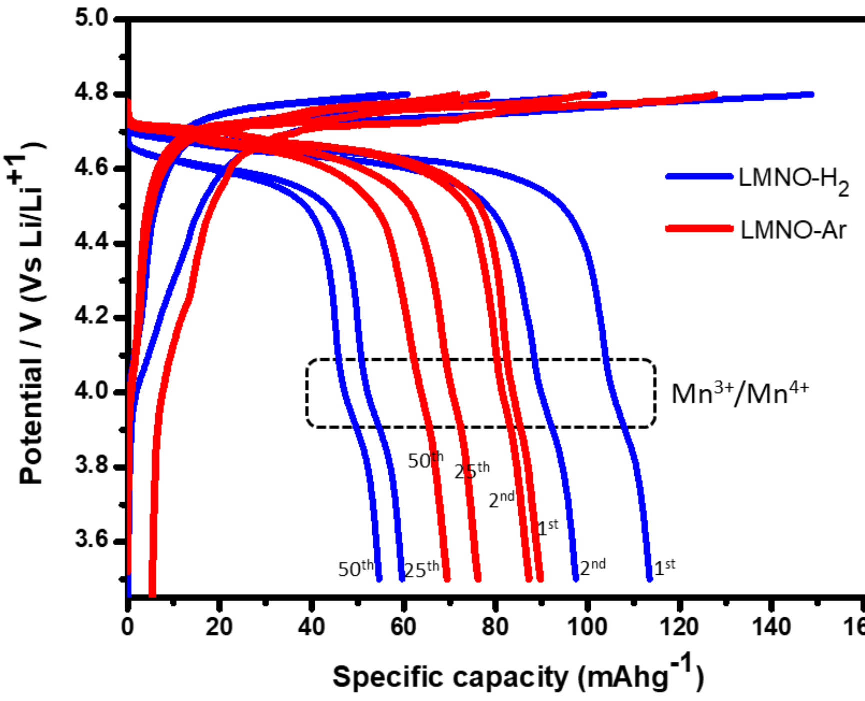

Figure 5.26: GC-D: LMNO-Ar and LMNO:H_2 samples

Thus, the LMNO-H_2 cathode material has higher specific capacity than LMNO-Ar cathode material because of:

(1) Higher degree of oxygen vacancy.

(2) Higher degree of disordered phase

(3) Higher Mn^{3+} content

(4) Lower impurity content

(5) Higher Nitrogen Gas Adsorption surface area

(6) Lower extent of confusion between Li^+ and transition cations

The higher Mn^{3+} content in LMNO-H_2 electrode caused it to have higher amount of soluble Mn^{2+} in the electrolyte by disproportionate reaction than LMNO-Ar cathode material. Hence LMNO-H_2 electrode capacity deteriorated faster than the LMNO-Ar electrode as shown in Figure 5.27. The specific capacity of LMNO-H_2 electrode faded from 113.6 $mAhg^{-1}$ to 54.9 $mAhg^{-1}$ after 50 cycles while that of LMNO-Ar electrode faded from 90.1 $mAhg^{-1}$ to 69.9 $mAhg^{-1}$. Therefore, LMNO-Ar electrode has a higher capacity retention (77.6%) than the LMNO-H_2 electrode (48.3%). Consequently, we can conclude that the LMNO-H_2 cathode material has higher specific capacity than LMNO-Ar cathode material but has worse cycling stability. The higher oxygen vacancy and Mn^{3+} contents in the LMNO-H_2 led to the low cycling stability. The LMNO-Ar cathode material has a lower specific capacity because of its lower Mn^{3+} and impurity contents. The impurities restrict the Li^+ mobility and hence lowered the capacity of the LMNO-Ar cell. The lower Nitrogen Gas Adsorption surface area of LMNO-Ar cathode material offered a reduced surface contact with the electrolyte, thus reduction in the side reactions and consequently a higher retention capacity. Going by the proposition of Ke [15] that the voltage plateau-length around 4 V is used to quantify the amount of Mn^{3+} in spinel LMNO, it may be suggested from the lengths of plateau around 4 V of LMNO-Ar and LMNO-H_2 electrodes in Figure 5.1.3 that the Mn^{3+} content of LMNO-H_2 is more than that of LMNO-Ar. This is consistent with previous sub-sections' results. Figure 5.27 also shows the coulombic efficiency of the two electrode materials. The coulombic efficiency of LMNO-Ar electrode increased steadily from cycle zero and stabilized around cycle 20 at coulombic efficiency of 97%. At the end of the 50 cycles LMNO-Ar electrode material has coulombic efficiency of 97%. While the coulombic efficiency of LMNO-H_2 electrode material increased steadily from cycle zero to cycle 2: attained coulombic efficiency of 96%, it then decreased to about 94% at cycle 6 before it started to increase again. The LMNO-H_2 electrode material stabilized around cycle 13 at coulombic efficiency of 98% and maintain the value to the end of 50 cycles. From cycle 6 to 50, the LMNO-H_2 electrode material has a better coulombic efficiency than LMNO-Ar electrode material.

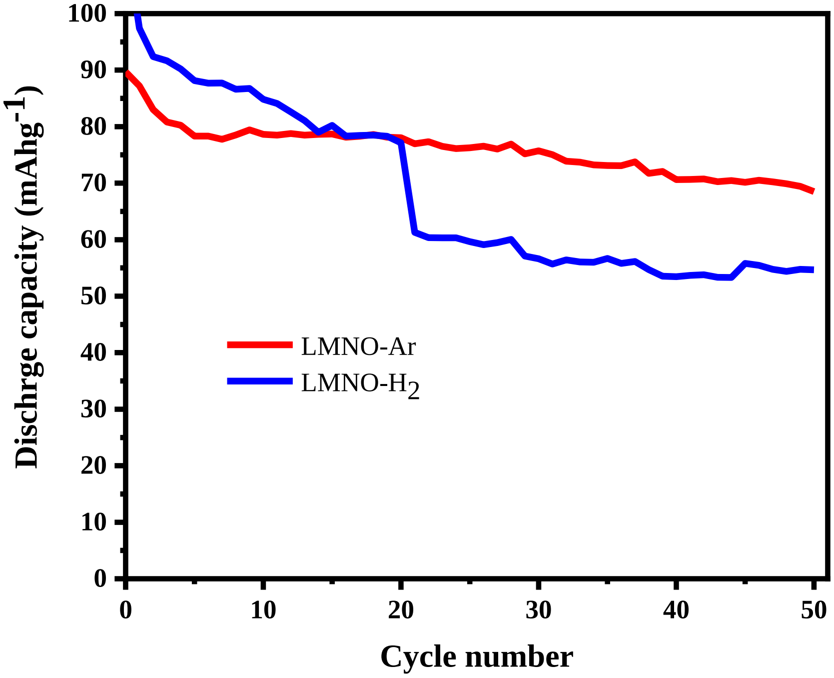

Figure 5.27: Discharge capacity Vs cycle number

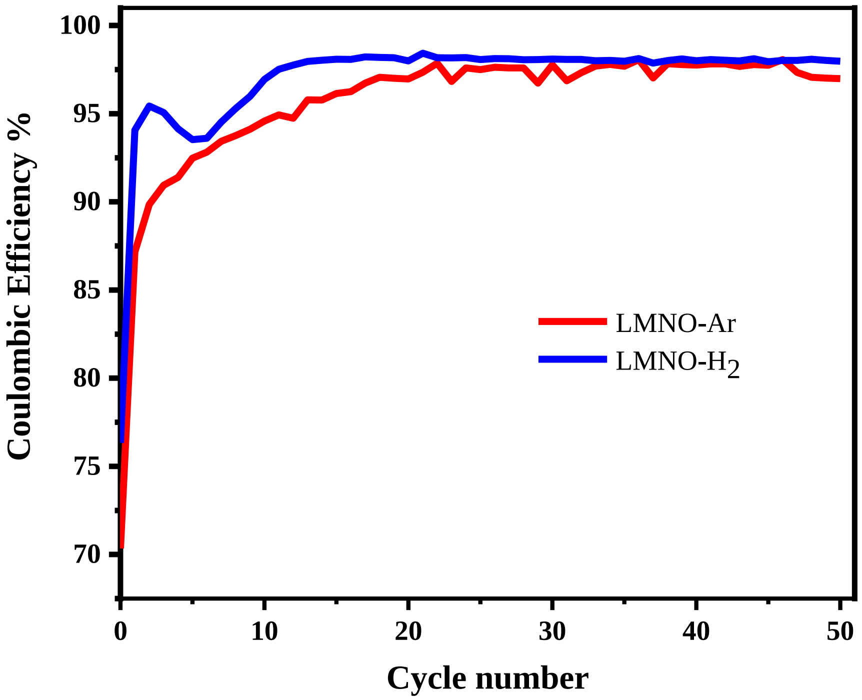

Figure 5.28: Coulombic efficiency and discharge capacity and Vs cycle number

5.3 Conclusions

The oxygen vacancies LMNO-Ar and LMNO-H_2 were successfully synthesized by controlling the precursors' (β-$MnO_{2-\delta}$) synthesis atmosphere as confirmed by TGA, FTIR, RAMAN, XPS, CV, etc. The different levels of reducing the atmosphere under which the precursors were synthesized are identified as the key factor for the introduction of the oxygen vacancies into the LMNO-Ar and LMNO-H_2 cathode materials. The CV and GCD results confirmed the co-existence of disorder and ordered phases in the LMNO-Ar and LMNO-H_2 samples with different Mn^{3+} contents. The higher discharge capacity of LMNO-H_2 sample relative to that of the LMNO-Ar is attributed to its higher degree of oxygen vacancies, disorder, Mn^{3+} content and lower impurities. While the worse capacity fading of LMNO-H_2 sample is also ascribed to the same trend of indices (oxygen vacancies, disorder, Mn^{3+} content and impurities). In addition, the high oxygen vacancy LMNO-H_2 sample cathode material has high R_{CEI} which caused significant change to the electrochemical properties of the Li-ion battery. Thus, we can infer that the careful control of the precursors' synthetic atmosphere is critical to have appropriate contents of oxygen vacancies, disorder, Mn^{3+} content, impurities and CEI for the improved electrochemical performance of spinel LMNO. The oxygen vacancy content in spinel LMNO cathode material changes concurrently with the Mn^{3+} content and degree of disorder, but not with the impurity content Therefore it can be proposed that these fundamental findings can be a valuable direction to the design, synthesis and optimization of improved spinel LMNO for lithium-ion batteries.

5.4 References

1. J. Mao, K. Dai, M. Xuan, G. Shao, R. Qiao, W. Yang, V. S. Battaglia, G. Liu, ACS Appl. Mater. Interfaces 2016, 8, 9116−9124

2. G. Q. Liu, L. Wen, Y. M. Liu, J Solid State Electrochem (2010) 14:2191–2202

3. Y. Gao, K. Myrtle, M. Zhang, J. N. Reimers, J. R. Dahn, Phys. Rev. B 54, 16670

4. P. B. Samarasingha, J. Sottmann, S. Margadonna, H. Emerich, O. Nilsen, H. Fjellvåg, Acta Materialia 116 (2016) 290-297

5. H. Liu, X. Zhang, X. He, A. Senyshyn, A. Wilken, D. Zhou, O. Fromm, P. Niehoff, B. Yan, J. Li, M. Muehlbauer, J. Wang, G. Schumacher, E. Paillard, M. Winter, J. Li, Journal of The Electrochemical Society, 165 (9) A1886-A1896 (2018)

6. K. Lee, G. J. Yang, Y. Kim, Ceramics International 43 (2017) 15510–15518

7. G. Liu, Y. Li, B. Ma, Y. Li, Electrochimica Acta 112 (2013) 557– 561

8. G. Liu, J. Zhang, X. Zhang, Y. Du, K. Zhang, G. Li, H. Yu, C. Li, Z. Li, Q. Sun, L. Wen, Journal of Alloys and Compounds 725 (2017) 580-586

9. J. Xiao, X. Chen, P. V. Sushko, M. L. Sushko, L. Kovarik, J. Feng, Z. Deng, J. Zheng, G. L. Graff, Z. Nie, D. Choi, J. Liu, J. Zhang, M. Stanley, Whittingham Adv. Mater. 2012, 24, 2109–2116

10. Q. Zhong, A. Bonakclarpour, M. Zhang, Y. Gao, J. R. Dahn, J. Electrochem. Soc., Vol. 144, No. 1, January 1997

11. A. K. Haridas, C. S. Sharma, T. N. Rao, Electrochimica Acta 212 (2016) 500–509

12. E. Zhao, L. Wei, Y. Guo, Y. Xu, W. Yan, D. Sun, Y. Jin, Journal of Alloys and Compounds 695 (2017) 3393-3401

13. J. Lee, C. Kim, B. Kang, NPG Asia Materials (2015) 7, e211

14. J. Lee, N. Dupre, M. Avdeev, B. Kang Scientific Reports volume 7, Article number: 6728 (2017)

15. Y. Xue, Z. Wang, L. Zheng, F. Yu, B. Liu, Y. Zhang, K. Ke, Scientific Reports volume 5, Article number: 13299 (2015)

16. Y. Chen, Y. Sun, X. Huang, Computational Materials Science 115 (2016) 109–116

17. Phase Diagram of Li-Mn-O Spinel in Air J. M. Paulsen and J. R. Dahn *Chem. Mater.* 1999, *11,* 3065-3079

18. F. Cheng, T. Zhang, Y. Zhang, J. Du, X. Han and J. Chen, Angew. Chem. Int. Ed. 2013, 52, 2474 – 2477

19. Raman spectra of natural manganese oxides Simone Bernardini, Fabio Bellatreccia, Annalaura Casanova Municchia, Giancarlo Della Ventura, Armida Sodo, *J Raman Spectrosc*. 2019; 1–16

20. M. Kunduraciz, G. G. Amatucci, Journal of The Electrochemical Society, 153 (7) (2006) A1345-A1352

21. T. Zhang , F. Cheng , J. Du , Y. Hu and J. Chen Adv. Energy Mater. 2015, 5, 1400654

22. H. Wang, Z. Shi, J. Li, S. Yang, R. Ren, J. Cui, J. Xiao and B. Zhang, Journal of Power Sources 288 (2015) 206-213

23. In situ XRD measurements to explore phase formation in the near surface region Darina Manovaa) and Stephan Mändl, J. Appl. Phys. 126, 200901 (2019)

24. Y. Qian, Y. Deng, L. Wan, H. Xu, X. Qin, G. Chen, J. Phys. Chem. C 2014, 118, 15581−15589

25. J. Song, D. W. Shin, Y. Lu, C. D. Amos, A. Manthiram, John B. Goodenough, Chem. Mater. 2012, 24, 3101−3109

26. J. Feng, Z. Huang, C. Guo, N. A. Chernova, S. Upreti, M. S. Whittingham, ACS Appl. Mater. Interfaces 2013, 5, 10227−10232

27. W. Wei, Q. Xing, G. Jianling, W. Jiangfeng, Y. Huiyu, W. Li Journal of Rare Earth, Vol. 35, No. 9, Sep. 2017, P. 887

28. Yi-Chun Jin and Jenq-Gong Duh **RSC Adv.**, 2015,**5**, 6919-6924

29. J. Wang, D. Chen, W. Wu, L. Wang, G. Liang, Trans. Nonferrous Met. Soc. China 27(2017) 2239−2248

30. Z. Chen, R. Zhao, A. Li, H. Hu, G. Liang, W. Lan, Z. Cao, H. Chen, Journal of Power Sources 274 (2015) 265-273

31. J. Wen, D. Zhang, Y. Zang, X. Sun, B. Cheng, C. Ding, Y. Yua, C. Chen, Electrochimica Acta 133 (2014) 515–521

32. T. Yi, J. Mei, Y. Zhu, Journal of Power Sources 316 (2016) 85-105

33. L. Wang, H. Li, X. Huang, E. Baudrin, Solid State Ionics 193 (2011) 32–38

34. M. Kunduraciz, G. G. Amatucci, Journal of The Electrochemical Society, 153 (7) (2006) A1345-A1352

35. H. Sun, X. Kong, B. Wang, T. Luo, G. Liu, Int. J. Electrochem. Sci., 12 (2017) 8609 – 8621

36. G. Liu, K. Park, J. Song, J. B. Goodenough, Journal of Power Sources 243 (2013) 260-266

37. J. Deng, Y. Xu, L. Xiong, L. Li, X. Sun, Y. Zhang, Journal of Alloys and Compounds 677 (2016) 18-26

38. M. Létiche, M. Hallot, M. Huvé, T. Brousse, P. Roussel, C. Lethien, Chem. Mater. 2017, 29, 6044−6057

39. N. M. Hagh, G. G. Amatucci, Journal of Power Sources 195 (2010) 5005–5012

40. H. Liu, J. Wang, X. Zhang, D. Zhou, X. Qi, B. Qiu, J. Fang, R. Kloepsch, G. Schumacher, Z. Liu, J. Li, ACS Appl. Mater. Interfaces 2016, 8, 4661−4675

41. J. Cabana, M. Casas-Cabanas, F. O. Omenya, N. A. Chernova, D. Zeng, M. S. Whittingham, C. P. Grey, Chem. Mater. 2012, 24, 2952−2964

42. J. Feng, Z. Huang, C. Guo, N. A. Chernova, S. Upreti, M. S. Whittingham, ACS Appl. Mater. Interfaces 2013, 5, 10227−10232

43. A. K. Haridasa, C. S. Sharma and T. N. Rao Electrochimica Acta 212 (2016) 500–509

44. G. Liu, Y. Li, B. Ma, Y. Li, Electrochimica Acta 112 (2013) 557– 561

45. E. Zhao, L. Wei, Y. Guo, Y. Xu, W. Yan, D. Sun, Y. Jin, Journal of Alloys and Compounds 695 (2017) 3393-3401

46. H.W. Nesbitt and D. Banerjee, American Mineralogist, Volume 83, pages 305–315, 1998

47. Rosedhi, N. H. Idris, M, M. Rahman, M.F. Md Din, J. Wang, Electrochimica Acta 206 (2016) 374–380

48. H. Liu, X. Zhang, X. He, A. Senyshyn, A. Wilken, D. Zhou, O. Fromm, P. Niehoff, B. Yan, J. Li, M. Muehlbauer, J. Wang, G. Schumacher, E. Paillard, M. Winter, J. Li, Journal of The Electrochemical Society, 165 (9) A1886-A1896 (2018)

49. J. Xiao, X. Chen, P. V. Sushko, M. L. Sushko, L. Kovarik, J. Feng, Z. Deng, J. Zheng, G. L. Graff, Z. Nie, D. Choi, J. Liu, J. Zhang, M. Stanley, Whittingham Adv. Mater. 2012, 24, 2109–2116

50. G. Liu, Y. Du, W. Liu, L. Wen, Electrochimica Acta 209 (2016) 308–314

51. Y. Xue, Z. Wang, L. Zheng, F. Yu, B. Liu, Y. Zhang, K. Ke, Scientific Reports volume 5, Article number: 13299 (2015)

52. L. Wang, D. Chen, J. Liu, W. Wu, G. Liang, Powder Technology 292 (2016) 203–209

53. M.W. Robert and R. Smart, Surface Science 100 (1980) 590-604

54. N. Davison and W. R, McWinnie, Clays and Clay Minerals, Vol. 39, No 1, (1991) 22-27

55. G. Liu, Y. Du, W. Liu, L. Wen, Electrochimica Acta 209 (2016) 308–314

56. J. F. Moulder W. F. Stickle, P. E.'Sobol, K. D. Bomben, Perkin-Elmer Corporation Physical Electronics Division October 1992, page 230

57. K. Kishi. S. Ikedia, Chemistry Letters, pp. 245-248, 1972

58. L. Wang, D. Chen, J. Liu, W. Wu, G. Liang, Powder Technology 292 (2016) 203–209

59. M. Mancini, G. Gabrielli, P. Axmann, and M. Wohlfahrt-Mehrens Journal of The Electrochemical Society, 164 (1) A6229-A6235 (2017)

60. S.H. Park, S.-W. Oh, S.H. Kang, I. Belharouak, K. Amine, Y.-K. Sun, Electrochimica Acta 52 (2007) 7226–7230

61. Y. Sun, Y. Yang, H. Zhan, H. Shao, Y. Zhou, Journal of Power Sources 195 (2010) 4322–4326

62. Y. Xue, Z. Wang, L. Zheng, F. Yu, B. Liu, Y. Zhang, K. Ke, Scientific Reports volume 5, Article number: 13299 (2015)

63. J. Xiao, X. Chen, P. V. Sushko, M. L. Sushko, L. Kovarik, J. Feng, Z. Deng, J. Zheng, G. L. Graff, Z. Nie, D. Choi, J. Liu, J. Zhang, M. Stanley, Whittingham Adv. Mater. 2012, 24, 2109–2116

64. K. Edstr¨om, T. Gustafsson, J.O. Thomas, Electrochimica Acta 50 (2004) 397–403

65. Y. Kim, N. J. Dudney M. Chi, S. K. Martha, J. Nanda, G. M. Veith and C. Liang *Journal of The Electrochemical Society*, 160 (5) A3113-A3125 (2013),

CHAPTER 6

General conclusions

6.1 Conclusion

6.1.1 Effects of microwave irradiation on physical and electrochemical properties of Spinel $LiMn_2O_4$ Cathode Material

- The effects of microwave irradiation on the commercial LMO were studied. The microwave irradiation produced pure and high crystalline phase LMO.
- The microwave irradiated sample LMO-m has a larger Nitrogen Gas Adsorption surface area, pore volume and size than LMO-p for an increased discharge capacity.
- The microwave irradiation increased the Mn^{4+} content in LMO-m, thus the increased average Mn valency of LMO-m than that of the pristine (LMO-p).
- This simple process (microwave irradiation) can be applied in the strategic design and synthesis of LMO for improved LIBs.

6.1.2 Defect-engineering of β-$MnO_{2-\delta}$ precursor controls structure-property relationships in high-voltage spinel $LiMn_{1.5}Ni_{0.5}O_4$ cathode materials for lithium-ion battery

- The different levels of reducing environments under which the precursors were synthesized have great effects on the structural and electrochemical properties of the as prepared LMNO-Ar and LMNO-H_2 samples.
- The different levels of reducing environments lead to different degrees of oxygen vacancies, disorder phases, Mn^{3+} contents and impurities in LMNO-Ar and LMNO-H_2 samples.
- The LMNO-H_2 sample has a higher discharge capacity (113.6 $mAhg^{-1}$) and a lower retention capacity (48.3%) after 50 cycles. While LMNO-Ar sample has a lower discharge capacity (90.1 $mAhg^{-1}$) and higher retention capacity of (77.6%) after 50 cycles.
- This simple and environmentally friendly process can be conveniently adapted for large-scale production of high energy and power lithium-ion battery

6.1.3 Future work

- The electrochemical measurements of the spinel LMO and LMNO cathode materials were carried at room temperature. Therefore, the electrochemical measurements can be carried out at high temperature (55°C) as applicable for electric vehicles and stationary storage applications.
- The C-rate measurements will be carried out for the LMNO cathode materials.

- The microwave irradiation process can be inculcated into the synthesis processes of the LMNO cathode materials.
- The studies on the electrochemical measurements of the spinel LMO and LMNO cathode materials can be carried out in full cells (coin) using hard carbon as the anode.
- The studies on the electrochemical measurements of the spinel LMO and LMNO cathode be carried out in full cells (cylindrical: 18650).